Tectonics

RESEARCH ARTICLE
10.1029/2019TC005890

Special Section:
Tethyan Dynamics: from Rifting to Collision

The Cycladic Blueschist Unit on Tinos, Greece: Cold NE Subduction and SW Directed Extrusion of the Cycladic Continental Margin Under the Tsiknias Ophiolite

Thomas N. Lamont[1,2], Michael P. Searle[1], Phillip Gopon[1], Nick M. W. Roberts[3], Jon Wade[1], Richard M. Palin[1], and David J. Waters[1]

[1]Department Earth Sciences, University of Oxford, Oxford, UK, [2]School of Earth and Environmental Sciences, University of St Andrews, St Andrews, UK, [3]Geochronology and Tracers Facility, British Geological Survey, Nottingham, UK

Abstract High pressure-low temperature (*HP-LT*) metamorphic rocks structurally beneath the Tsiknias Ophiolite make up the interior of Tinos Island, Greece, but their relationship with the overlying ophiolite is poorly understood. Here, new field observations are integrated with petrological modeling of eclogite and blueschists to provide new insight into their tectonothermal evolution. Pseudomorphed lawsonite-, garnet-, and glaucophane-bearing schists exposed at the highest structural levels of Tinos (Kionnia and Pyrgos Subunits) reached ~22–26 kbar and 490–520°C under water-saturated conditions, whereas pseudomorphed lawsonite- and aegirine-omphacite bearing eclogite reached ~20–23 kbar and 530–570°C. These rocks are separated from rocks at deeper structural levels (Sostis Subunit) by a top-to-SW thrust. The Sostis Subunit records *P-T* conditions of ~18.5 kbar and 480–510°C and is overprinted by pervasive top-to-NE shearing that developed during exhumation from (M_1) blueschist to (M_2) greenschist facies conditions of ~7.3 ± 0.7 kbar and 536 ± 16°C. These *P-T-D* relationships suggest that the Cycladic Blueschist Unit represents a discrete series of tectonometamorphic subunits that each experienced different tectonic and thermal histories. These subunits were buried to variable depths and sequentially extruded toward the SW from a NE dipping subduction zone. The difference in age and *P-T* conditions between the *HP-LT* rocks and the overlying metamorphic sole of the Tsiknias Ophiolite suggests that this NE dipping subduction zone was active between circa 74 and 46 Ma and cooled at a minimum rate of ~1.2–1.5°C/km/Myr prior to continent-continent collision between Eurasia and Adria/Cyclades.

Plain Language Summary High pressure-low temperature metamorphic rocks make up the interior of Tinos Island, Greece and underlie an ancient piece of oceanic crust and mantle (Tsiknias Ophiolite). The rocks that make up Tinos were once mudstones and limestones deposited on the NE margin of the Cycladic-Adriatic continent and were deeply buried in a subduction zone. In this work, we investigate the structures and mineralogy of the Tinos high-pressure rocks and find they were buried to variable depths (80–60 km) and reached temperatures of 500–550°C. These packages of rock were then emplaced against each other during their return journey toward the surface after subduction ended. We document evidence for circa 25 Myr (ca. 74 and 46 Ma) of subduction prior to continent-continent collision (between Eurasia and Adria/Cyclades) on Tinos and that this records the closure of an ancient ocean to the NE of the Cyclades.

Key Points:
- Blueschist and eclogite facies metamorphism on Tinos record peak *P-T* conditions of 22–26 kbar, 490–520°C and 20–23 kbar, 530–570°C respectively
- *HP-LT* rocks were sequentially underplated and extruded to the SW by a combination of top-to-SW thrusting and top-to-NE normal-sensed shear
- *HP* metamorphism was associated with NE subduction of the Cycladic continental margin ~25 Myr after obduction of the Tsiknias Ophiolite

Supporting Information:
- Supporting Information S1
- Data Set S1
- Table S1

Correspondence to:
T. N. Lamont,
tnl1@st-andrews.ac.uk

Citation:
Lamont, T. N., Searle, M. P., Gopon, P., Roberts, N. M. W., Wade, J., Palin, R. M., & Waters, D. J. (2020). The Cycladic Blueschist Unit on Tinos, Greece: Cold NE subduction and SW directed extrusion of the Cycladic continental margin under the Tsiknias Ophiolite. *Tectonics*, *39*, e2019TC005890. https://doi.org/10.1029/2019TC005890

Received 21 SEP 2019
Accepted 20 JUN 2020
Accepted article online 25 JUN 2020

1. Introduction

High pressure-low temperature (*HP-LT*) metamorphism is a diagnostic feature of mature subduction zones and is characterized by rocks that have been buried along cool geothermal gradients (<10°C/km) (e.g., Fryer et al., 1999; Goffé & Chopin, 1986; Maekawa et al., 1993; Maruyama & Liou, 1996; Miyashiro, 1961; Okay, 1989; Oxburgh & Turcotte, 1971; Palin & White, 2016; St-Onge et al., 2013). *HP-LT* metamorphism of continental crust is a transient geological process that occurs over timescales of 1–10 Myr and is commonly associated with attempted continental crust subduction preceding or during subduction-termination due to continent-continent collision (Agard et al., 2009; Searle et al., 1994, 2004). *HP-LT* continental terranes are typically exhumed from mantle depths in two stages: first, at plate tectonic rates driven by positive buoyancy with respect to the surrounding lithospheric or asthenospheric mantle (Chemenda et al., 1995; England & Holland, 1979) and then at slower rates during exhumation through

the overlying crust. This tectonothermal evolution associated with subduction termination contrasts with high geothermal gradients (>30°C/km) recorded in metamorphic sole rocks directly under ophiolites, which are interpreted to represent subduction initiation (e.g., Cowan et al., 2014; Guilmette et al., 2018; Hacker, 1990; Searle & Cox, 2002). Although continental *HP-LT* metamorphism is common in the geological record, precontinental subduction events, such as ophiolite emplacement, are rare. The best examples include Oman, the Himalaya, New Caledonia, and Western Turkey. In these locations, *HP* metamorphism postdates ophiolite obduction by circa 15, circa 25, circa 12, and circa 15 to <1 Myr, respectively (e.g., Cluzel et al., 2012; Plunder et al., 2016; Pourteau et al., 2019; Searle et al., 1994, 2004; St-Onge et al., 2013; Warren et al., 2003, 2005). This observation poses three tectonic questions: (1) Does ophiolite obduction precede continental high-pressure (*HP*) metamorphism and by how long? (2) Do *HP-LT* metamorphic rocks record the same subduction zone that suprasubduction zone (SSZ) ophiolites were formed and obducted onto earlier in the orogenic history? (3) how quickly do subduction zones cool following initiation?

The Cycladic Blueschists Unit (CBU) on the island of Tinos, Greece, provides new insights into these questions, as rocks representing the Adriatic-Cycladic continental margin were buried down a NE dipping subduction zone and exhumed beneath the overriding Tsiknias Ophiolite (Avigad & Garfunkel, 1989; Bröcker, 1990; Bröcker et al., 1993; Katzir et al., 1996; Lamont, Roberts, et al., 2020). Although studied in less detail than neighboring Syros, Tinos also preserves fresh eclogite and blueschist facies rocks (Bröcker, 1990; Bröcker & Enders, 1999; Bröcker et al., 1993, 2004) that are juxxtaposed against ophiolitic and pelagic metasedimentary rocks that did not reach *HP* (Avigad & Garfunkel, 1989; Katzir et al., 1996) and instead record a subduction initiation event/earlier stages of subduction during orogenesis (Lamont, Roberts, et al., 2020).

HP-LT metamorphic rocks on Tinos are investigated to constrain their pressure-temperature and deformation (*P-T-D*) evolution through field and microstructural observations, thermobarometry and petrological modeling. The *P-T-D* histories are integrated into a tectonothermal model that explains the structure of the CBU on Tinos and the relationship with the overlying Tsiknias Ophiolite.

2. Geology of Tinos and the Cycladic Blueschist Unit

Tinos island is a part of the Attic Cycladic Massif (ACM; Durr et al., 1978; Papanikolaou, 2013) (Figure 1), which experienced a complete orogenic cycle including ophiolite obduction, *HP* metamorphism through crustal thickening, and regional metamorphism to crustal extension (Lamont et al., 2019; Lamont, Roberts, et al., 2020; Searle & Lamont, 2019). The island represents a NW-SE trending dome (Figure 2) and comprises two distinct tectonometamorphic units (Upper Unit and Lower Unit) that are separated by a greenschist facies low-angle normal-sensed shear zone (the Tinos Shear Zone, TSZ), which displays top-to-NE kinematics (Avigad & Garfunkel, 1989; Brichau et al., 2007; Bröcker, 1990; Bröcker & Franz, 1994, 1998; Bröcker et al., 1993, 2004; Jolivet et al., 2010; Katzir et al., 1996; Melidonis, 1980; Ring & Layer, 2003). The Upper Unit, at the highest structural levels, comprises the Tsiknias Ophiolite (interpreted to represent the upper plate) and underlying metamorphic sole amphibolites, pelagic sediments, and mafic phyllites (interpreted to represent oceanic crust the subducted plate) that did not experience (M_1) *HP* conditions (Katzir et al., 1996; Lamont, Roberts, et al., 2020). The Lower Unit comprises (M_1) *HP-LT* continental margin rocks of the CBU, which are highly retrogressed to (M_2) greenschist facies assemblages (Avigad & Garfunkel, 1989; Bröcker, 1990; Bröcker et al., 2004; Parra et al., 2002; Ring et al., 2010).

2.1. Upper Unit (Tsiknias Ophiolite and Metamorphic Sole)

The Tsiknias Ophiolite (Figure 2) in the Upper Unit represents the highest thrust sheet in the ACM, comprising a fragmented piece of Jurassic oceanic crust and upper mantle dated at 161.8 ± 2.7 Ma by U-Pb zircon from a plagiogranite within the Moho Transition Zone (Lamont, Roberts, et al., 2020). The ophiolite is incomplete and tectonically dismembered, owing to intense deformation by both out-of-sequence thrusts and normal faults (Katzir et al., 1996; Lamont, Roberts, et al., 2020). A major top-to-SW thrust (The Tsiknias Thrust) crops out structurally beneath the mantle section of the Tsiknias Ophiolite. Immediately, structurally beneath this tectonic contact is a metamorphic sole (interpreted as the subducting plate) comprising anatectic amphibolites (metamorphosed basalts and gabbros) at the top of the section and pelagic metasediments, including meta-cherts and mafic phyllites at the bottom (Mirsini Unit; Lamont, Roberts, et al., 2020). The metamorphic sole displays an inverted metamorphic gradient, with *P-T* conditions of ~8.5 kbar and >800°C at the top, and ~600°C at the base (Lamont, Roberts, et al., 2020). Metamorphism

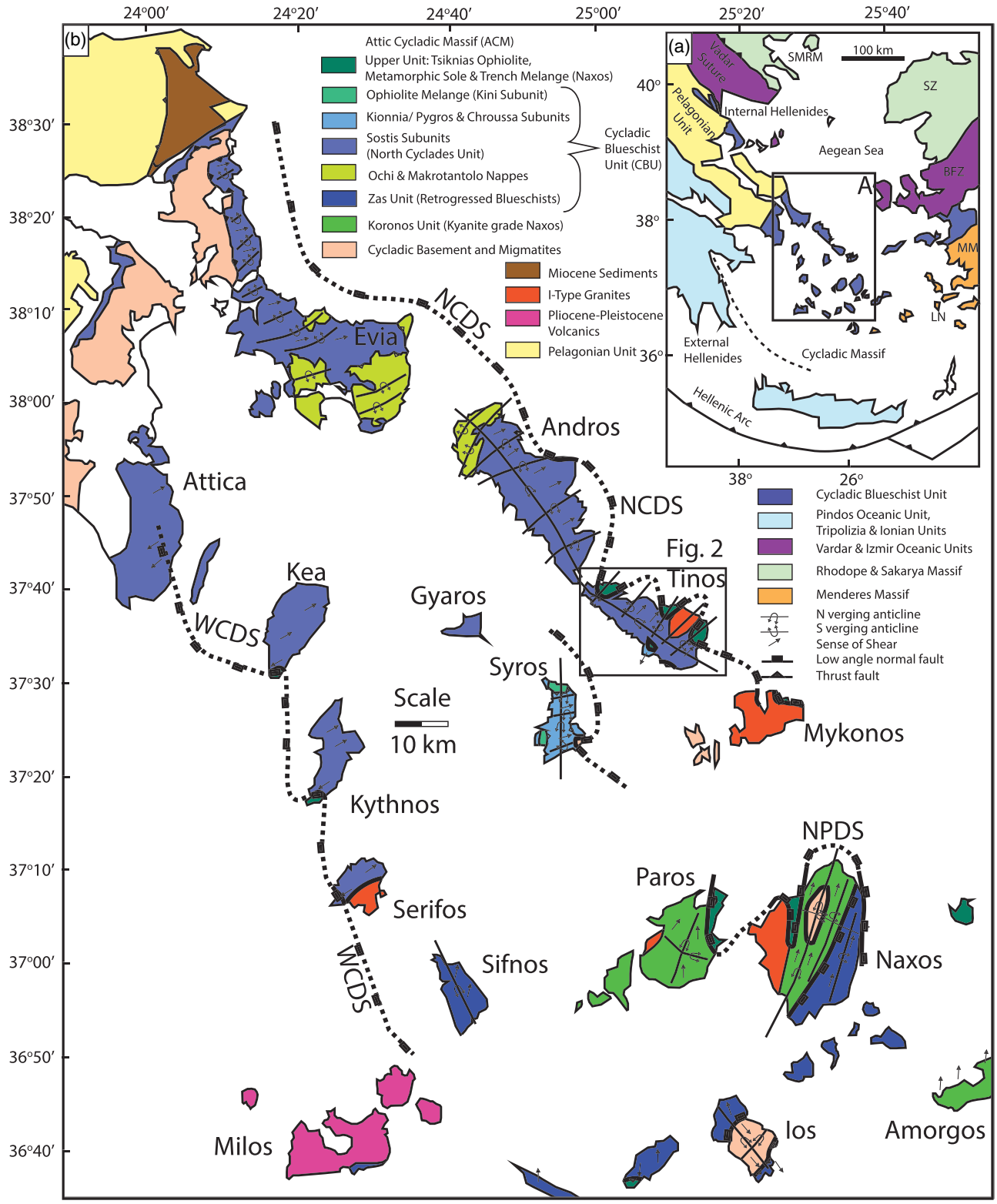

Figure 1. (a) Tectonic map of the Aegean showing the location of Tinos and the Cycladic Blueschist Unit; (b) zoomed in map of the Cycladic Blueschist Unit with age data and reported *P-T* conditions.

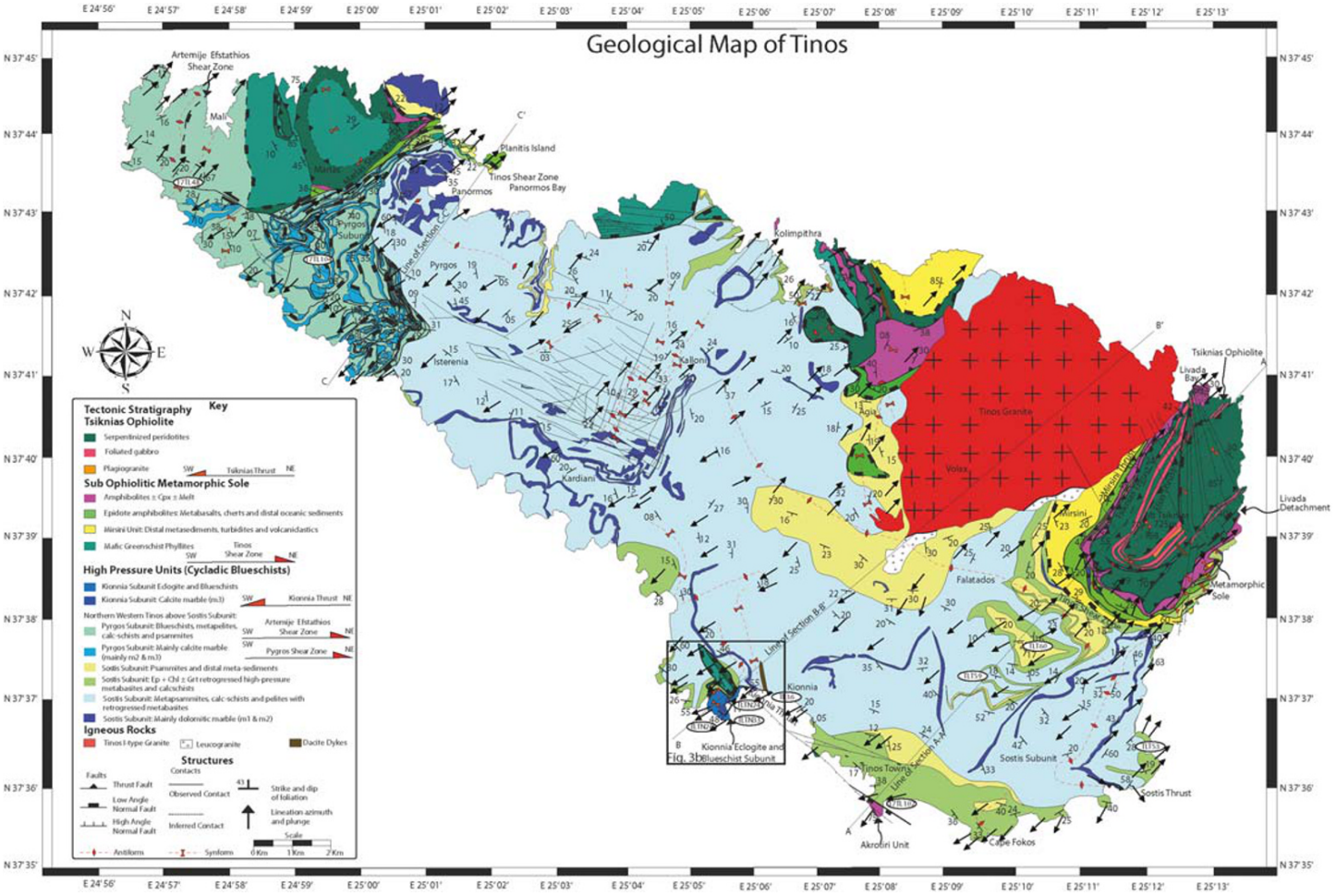

Figure 2. New geological map of Tinos showing key structural units of the Lower Unit and samples locations used in this study, with locations of cross sections A-A′, B-B′, and C-C′. For locations consult the geological map in Figure 1, note that the Kionnia Subunit is projected at the highest structural level but only crops out on the Kionnia Peninsular.

and deformation occurred during initiation of a NE dipping subduction zone preceding ophiolite emplacement at circa 74.0 ± 3.5 Ma, dated by U-Pb zircon of partial melt that emanates from amphibolites immediately beneath the Tsiknias Thrust (Lamont, Roberts, et al., 2020). The timing of sole metamorphism (interpreted to represent subduction initiation) corresponds to when Africa's plate motion was convergent (N-S) with respect to Eurasia (Vissers & Meijer, 2012). The circa 90 Myr age discrepancy between the ophiolite and the sole suggest the heat to drive metamorphism was derived from a combination of the overriding mantle wedge and shear heating on the subduction interface. Mafic phyllites within the sole yield Rb-Sr phengite-whole-rock ages of circa 92–21 Ma (Bröcker & Franz, 1998), which is probably due to open system behavior. The Akrotiri Unit is exposed on the SE coast near Tinos Town, comprising amphibolite and paragneiss with K-Ar ages of circa 76–66 Ma, similar to the age metamorphic sole (Patzak et al., 1994). The Akrotiri Unit is separated from the Lower Unit by a late top-to-SW shear zone that truncates the CBU (Lamont, Roberts, et al., 2020).

2.2. Lower Unit (Cycladic Blueschist Unit)

Petrological studies from several Cycladic islands have yielded contrasting peak M_1 *P-T-t* estimates within the CBU (Lower Unit). These range from 15–18 kbar and 500°C (Avigad & Garfunkel, 1991; Okrusch & Bröcker, 1990; Parra et al., 2002; Schliestedt et al., 1987; Schmädicke & Will, 2003; Schumacher et al., 2008) to 19–20 kbar and 525–550°C (Ashley et al., 2014; Dragovic et al., 2012; Groppo et al., 2009; Trotet et al., 2001). Recent petrological modeling by Laurent et al. (2018) suggested Syros eclogites reached peak conditions of 19–22 kbar at 550°C, followed by isothermal decompression to ~10 kbar. They suggest a synorogenic

extrusion mechanism and argue the rocks were reheated to 500–550°C in the midcrust. However, Behr et al. (2018) obtained lower pressures for eclogite facies metamorphism of 12.5–15.5 kbar at 450–550°C, based on quartz-in-garnet inclusion barometry, questioning whether the eclogites reached such *HP*. On mainland Greece, blueschist facies rocks occur in Attica and Evia but did not reach as *HP* and probably relate to an overlying thrust package (~12–13 kbar and 360–380°C; e.g., Baziotis et al., 2020).

Thermobarometry of the CBU on Tinos suggests peak M_1 conditions of ~12–20 kbar and 450–550°C (e.g., Bröcker et al., 1993; Parra et al., 2002; Trotet et al., 2001). A three-stage exhumation has been suggested: first, decompression from 18–15 kbar at 500°C to 9–5 kbar at 400°C, followed by a thermal overprint (400–550°C) and further decompression from 9 kbar at 550–570°C to 2 kbar at 420°C (Bröcker et al., 1993; Parra et al., 2002). The Basal Unit comprising a dolomite-phyllite-quartzite sequence has been suggested to crop out at Panormos Bay in NW Tinos. It is postulated that these rocks did not experience *HP* conditions due to the absence of glaucophane, distinct deformational characteristics, and preservation of undeformed fossils within the marbles (Avigad & Garfunkel, 1989); however, this interpretation is debated. Bröcker and Franz (2005), show that Rb-Sr ages and phengite compositions are indistinguishable between both units, indicating they reached *HP* conditions at the same time, and oxygen isotope data suggest both units equilibrated at similar temperatures (Bröcker & Franz, 2005; Matthews et al., 1999). If there was a contrast in metamorphic grade between these two units, then the contact would have been a thrust (Panormos Thrust), placing the CBU over the Basal Unit, which did not experience such *HP* (Avigad & Garfunkel, 1989; Bröcker & Franz, 2005). Additionally, a mélange-like outcrop pattern with blocks of eclogite and blueschist within a host metasedimentary matrix is described by Bulle et al. (2010) and Bröcker et al., 2014 for a few locations within the Lower Unit including Kionnia Peninsular and within the interior of the island. These mélange-like outcrops differ from mélanges exposed on Syros, which are bounded by a serpentine matrix, whereas on Tinos they are hosted in a more coherent metasedimentary matrix that appears to have experienced a similar deformation and metamorphic history, although we acknowledge rare, narrow and laterally discontinuous serpentinite outcrops occur particularly near Tinos Town.

It is unclear whether these semicontinuous eclogite and blueschist horizons experienced similar pressures to the rest of the Lower Unit. The classic interpretation is that entire Lower Unit (CBU) experienced the same tectonothermal history. The apparent better preservation of *HP* rocks at high structural levels and more extensive retrogression at deeper levels has been attributed to the increased availability of retrograde fluids with depth (Avigad & Garfunkel, 1989; Bröcker, 1990; Bröcker et al., 2014). An alternative hypothesis to explain this observation is that the Lower Unit represents a series of tectonically bound slices that experienced discrete metamorphic histories, with lower levels not being buried as deeply within the subduction-accretion system. This is the main questions we aim to address.

The timing and duration of (M_1) *HP* metamorphism within the CBU has been constrained by a range of isotopic dating methods. On Tinos, Hinsken et al. (2016) report sediment deposition U-Pb zircon ages of Triassic-Permian age population (200–275 Ma) that includes peaks around 230, 245, and 255 Ma, with the youngest detrital zircon ages of circa 70–80 Ma. Eocene metamorphic ages in blueschists from Kionnia Peninsular yield ages of 53.5 $\pm$ 1.6 and 56.7 $\pm$ 3.9 Ma (ca. 57–52 Ma) and a single age of circa 31 Ma (Bulle et al., 2010). In contrast, a jadeitite from Kionnia Peninsular yields a U-Pb age of circa 63–61 Ma (Bröcker & Enders, 1999). These *HP* metamorphic ages slightly predate Rb-Sr and Ar-Ar data reported for *HP-LT* and variably overprinted rocks from Tinos and other Cycladic islands spanning circa 44–40 Ma for peak to immediately post M_1 (herein referred to M_{1b}) (e.g., Bröcker & Franz, 1998; Bröcker et al., 1993; Huet et al., 2015; Peillod et al., 2017). Lu-Hf garnet geochronology yields ages of circa 52–50 Ma (Lagos et al., 2007) on Syros eclogites and circa 46 Ma (Dragovic et al., 2012, 2015) on Sifnos eclogites. U-Pb zircon geochronology from meta-plagiogranite and *HP* meta-gabbro on Syros provide an estimate of peak M_1 eclogite facies metamorphism between circa 53 and 50 Ma (Tomaschek et al., 2003), which correlates with the upper end of the 52–42 Ma age range reported from Ar-Ar dating of white mica on Syros eclogite and meta-gabbro (Putlitz et al., 2005). These ages correlate with a U-Pb allanite age of circa 52–46 Ma from Naxos blueschists (Lamont, 2018) and 64–40 Ma by U-Pb zircon rim ages from Naxos metasediments (Bolhar et al., 2017; Martin et al., 2006) and white mica on Ios (Lister & Forster, 2016). M_2 greenschist facies retrogression on Tinos has been dated between circa 36 and 21 Ma (Bröcker et al., 1993, 2004, 2014), whereas the rest of the Cyclades record M_2 ages between 36 and 13 Ma (Keay et al., 2001; Lamont, 2018; Peillod

et al., 2017). The best constraint on the timing of tectonic juxtaposition of the Upper and Lower Units on Tinos is an Rb-Sr age of circa 21 Ma from a deformed phyllite close to the TSZ (Bröcker & Franz, 1998; Zeffren et al., 2005). Final exhumation of the CBU occurred at 12–8 Ma based on fission track ages (Ring & Layer, 2003; Soukis & Stockli, 2013).

The tectonic regime of the area following subduction and accretion is debated. Slab roll-back of the Hellenic subduction zone since the Eocene to present day (Lister et al., 1984; Jolivet et al., 2013, 2015; Jolivet & Brun, 2010) is a popular model to explain extension and exhumation of the Cyclades. Many authors regard slab rollback as having caused isobaric heating and Barrovian metamorphism (M_2) of previous *HP-LT* rocks, due to increased basal heating from the upwelling asthenosphere (e.g., Jolivet et al., 2013; Jolivet & Brun, 2010). However, a crustal thickening model has been proposed by Lamont et al. (2019) and Searle and Lamont et al. (2019) who argue for compression as a result of continent-continent collision between Cyclades/Adria and Eurasia as the cause of M_2-M_3 kyanite-sillimanite grade metamorphism on Naxos, based on isoclinal upright folds within the Naxos core, a clockwise prograde *P-T-t* paths of kyanite grade gneisses and migmatites, and evidence for horizontal constriction and vertical extension within the core of Naxos migmatite dome (Lamont et al., 2019; Virgo et al., 2018; von Hagke et al., 2018). Lamont et al. (2019) suggested a switch from overall compression to extension occurred at circa 15 Ma, timing that coincides with a two-fold decrease in the Africa-Eurasia convergence rate (DeMets et al., 2015). This tectonic reversal may have occurred due to gravitational collapse of over-thickened crust, or removal of the lithospheric mantle, which may have resulted in the onset of normal faulting that caused rapid exhumation and cooling.

3. Field Relationships and Petrography of the CBU on Tinos

A new structural and metamorphic map and cross sections are presented in Figures 2, 3, and S1 in the supporting information and a smaller-scale map and cross sections of the Kionnia Subunit (see below) in southern Tinos is presented in Figure 3. The new mapping has integrated the previous detailed observations (Avigad & Garfunkel, 1989; Bröcker, 1990; Bröcker & Franz, 2005; Bröcker et al., 1993; Jolivet et al., 2010; Katzir et al., 1996; Melidonis, 1980) and included the marble bands (m1–m3), which are classically used as structural markers, into a new structural framework. For a more thorough summary of methods please refer to supporting information Text S1. The following sections and Figures 4–7 describe the key field and petrological observations from structurally high to structurally low, which have new implications for the evolution of *HP* rocks on Tinos and the Cyclades. Blueschist, eclogite, and greenschist facies samples were collected at all structural levels to investigate spatial variations in the *P-T* conditions of prograde, peak, and retrograde metamorphism. Representative photomicrographs are displayed in Figures 8 and 9 and a schematic illustration of deformation and mineral growth and microstructure is displayed in Figure 10. Garnet compositions and maps are presented in Figure 11, and other phases compositions in supporting information Text S1 and Table S1. For a full petrographic description of each sample, consult supporting information Text S1.

3.1. The Kionnia Subunit

Eclogite and blueschist facies rocks occur within an ~500 m thick intensely folded metasedimentary sequence at Kionnia Peninsular (Bröcker & Enders, 1999) (Kionnia Subunit) on the south coast of Tinos, at the highest structural levels of the Lower Unit (Figures 2 and 3; N37.548015, E25.125559). This sequence comprises calcite marbles (m3) intercalated with metasediments and meta-basalts that form granoblastic and foliated eclogite and blueschist. At least three structural fabrics are preserved within the subunit. S_1 is only preserved as inclusions within garnet cores and is a planar fabric defined by prograde-peak M_1 inclusions of glaucophane, rutile, and lawsonite pseudomorphs. The S_1 fabric is folded by the S_{2a} fabric. S_{2a} is preserved as inclusions of lozenge shaped lawsonite pseudomorphs within garnet rims that show a 90° rotation from the S_1 inclusion orientation. S_{2a} also forms matrix crenulations (Figure 6a) with millimeter-centimeter-sized microlithons affecting peak M_1 matrix phases including glaucophane, omphacite, phengite and rutile (Figures 8g, 8k, and 8n). In the lower half of the subunit, a top-to-SW shear fabric (S_{2b}) overprints the S_{2a} fabrics (best seen at Kionnia Beach at the base of the subunit) and affects cleavage domains. S_{2b} is associated with S-C′ that deforms the peak M_1 and retrograde M_{1b} phases (including clinozoisite and titanite), indicating top-to-SW shearing developed at peak to immediately post M_1 and continued during earliest stages of exhumation (M_{1b}) (Figure 8d). In the upper half of the subunit, a penetrative top-to-NE shear fabric (S_3)

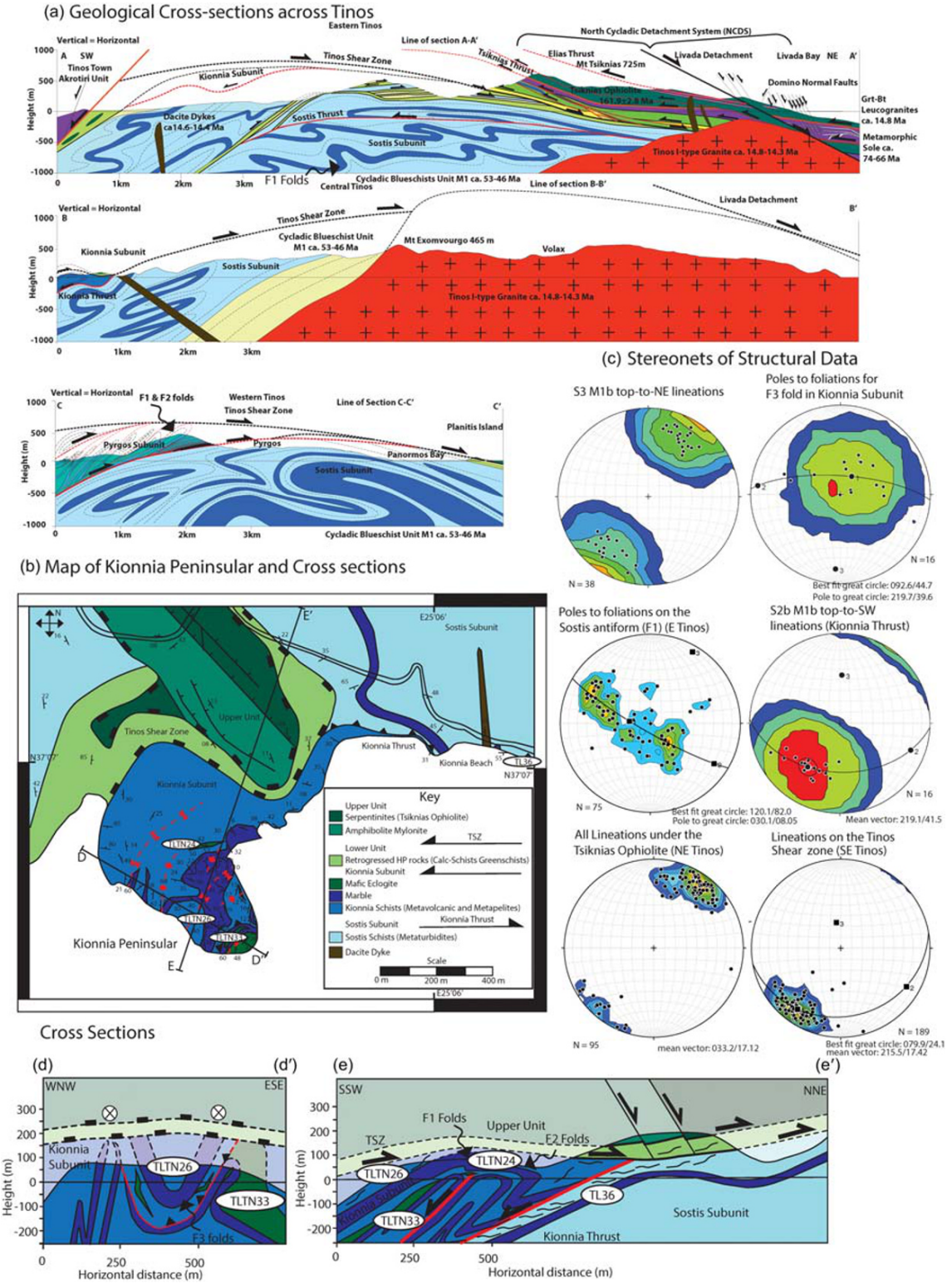

Figure 3. (a) Geological cross sections across Tinos along lines A-A′, B-B′, and C-C′ on Figure 2. (b) Geological map of Kionnia peninsular in Southern Tinos with samples locations used in this study with cross sections D-D and E-E′. (c) Stereonets of structural data from the Tsiknias Ophiolite metamorphic sole, and blueschist facies and retrograde greenschist facies structures on Tinos. See text for more discussion.

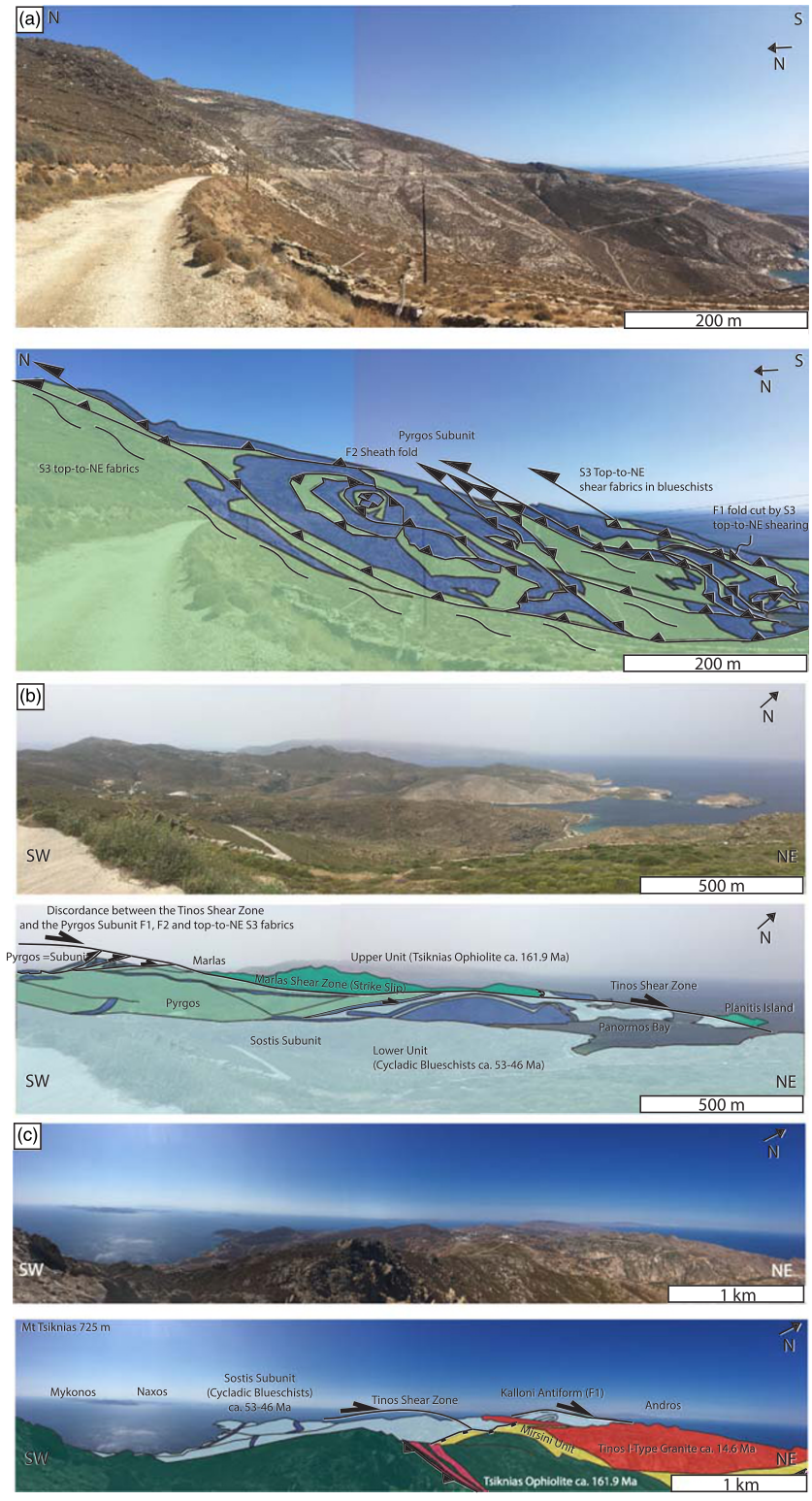

Figure 4. Panoramic photographs of structures within the Lower Unit on Tinos: (a) cross section through marbles folds and shear zones of the Pyrgos subunit to the west of Isternia (N37.628200, E25.029618), the folds are truncated by top-to-NE shearing structures (S3). (b) Overview of Panormos Bay (N37.635506, E25.058592) showing discordance of the high-pressure structures and the Tinos Shear Zone that is folded across the island. (c) Overview of the large-scale structures on Tinos from the top of Mt Tsiknias, (37.580569, 25.225505) showing the Upper and Lower Units that are cut by the Tinos pluton.

Figure 5. Annotated cross section of the Kionnia Subunit. (a) Photograph of the Kionnia Peninsular looking west with (b) an overview of the key geological features and location of outcrop photographs below. (c) F_1 and F_2 isoclinally folded sediments with a relatively undeformed fresh eclogite boudin TLTN33 in a dilatant strain zone. (d) S_{2b} top-to-SW retrogressed eclogite. (e) Top-to-SW S-C′ fabrics in meta-psammite. (f) F_2 sheath folded calc-schists with mafic retrogressed eclogite pods. Top-to-SW calcite sigma porphyroclast (S_{2b}) on the Kionnia Thrust. Retrogressed mafic boudin (now chl + pl + act) with meter scale top-to-SW asymmetry. (i) F_1 SW verging isoclinal fold within eclogite facies meta-psammnites.

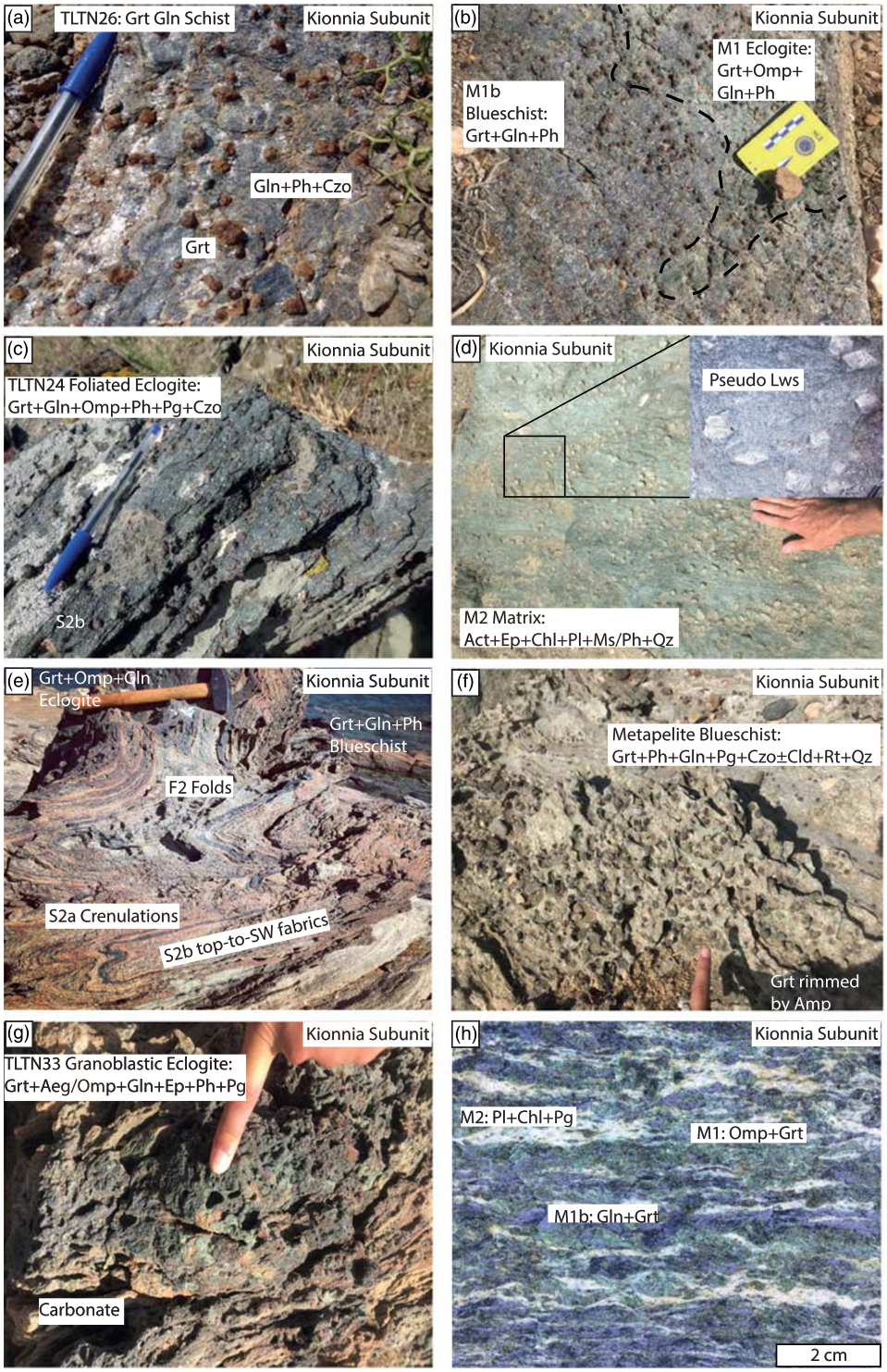

Figure 6. Outcrop photographs of fresh blueschist and eclogite facies assemblages from the Kionnia and Pyrgos Subunits. (a) Garnet glaucophane schist at the top of the Kionnia Subunit (TLTN26) (N37.548336, E25.124193). (b) Blueschist and eclogite facies paragenesis in the same outcrop (mafic garnet glaucophane schist) with localized omphacite (green) indicating boarder line eclogite facies conditions. (c) TLTN24 foliated eclogite (N37.550873, E25.124344). (d) Lawsonite pseudomophs (now Pg + Czo + Pl in retrogressed calc schist (N37.553464, E25.129058)) with zoomed in inset. (e) TLTN33 eclogite within folded calc-silicates. (f) Pelitic eclogites with 2 cm sized garnets + phengite ± chloritoid. (g) Garnet phengite schists interstitial with Kionnia eclogite, (h) another highly deformed mafic retrogressed eclogite pod similar to TLTN33.

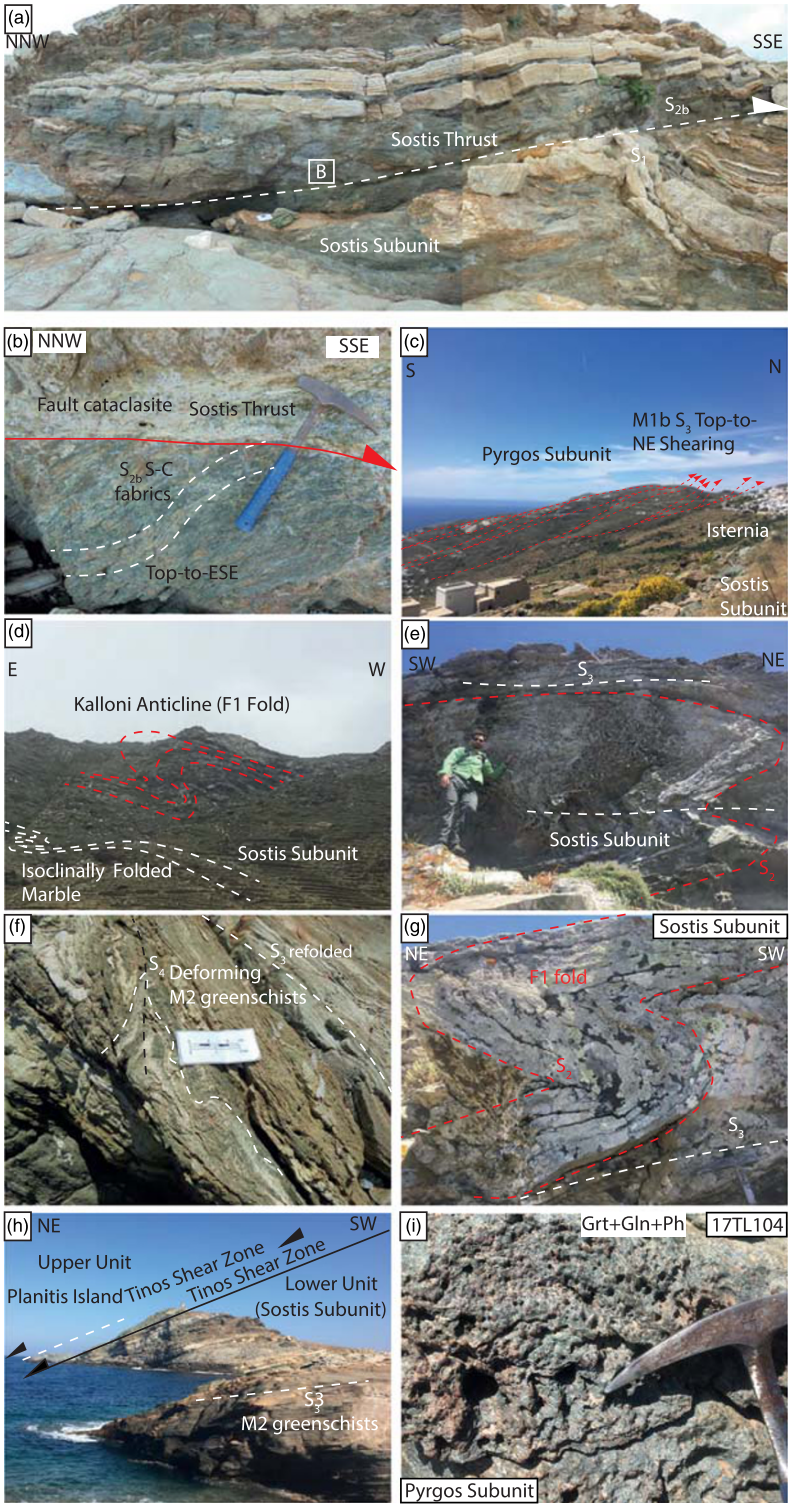

Figure 7. Meso-scale photographs of the Sostis Subunit on Tinos: (a and b) The Sostis Thrust (N37.534509, E25.223207), with clear brittle deformation overprinting ductile top-to-ESE shearing affecting glaucophane and phengite. (c) Top-to-NE S_3 shearing in the Pyrgos Subunit. (d) The Kalloni Anticline in central Tinos (N37.611719, E25.109457) that verges toward the SE. (e) Hinge of a NE verging F_2 sheath fold within the Sostis Unit (N37.604766, E25.089470). (f) Greenschist facies upright F_4 fold. (g) F_1 fold in psammites from the Sostis Unit (37.604695, 25.090930). (h) The Tinos Shear Zone at Panormos Bay (37.661674, 25.061793). (i) Blueschist within Pyrgos Subunit (sample 17TL104; N37.639889, E25.025361).

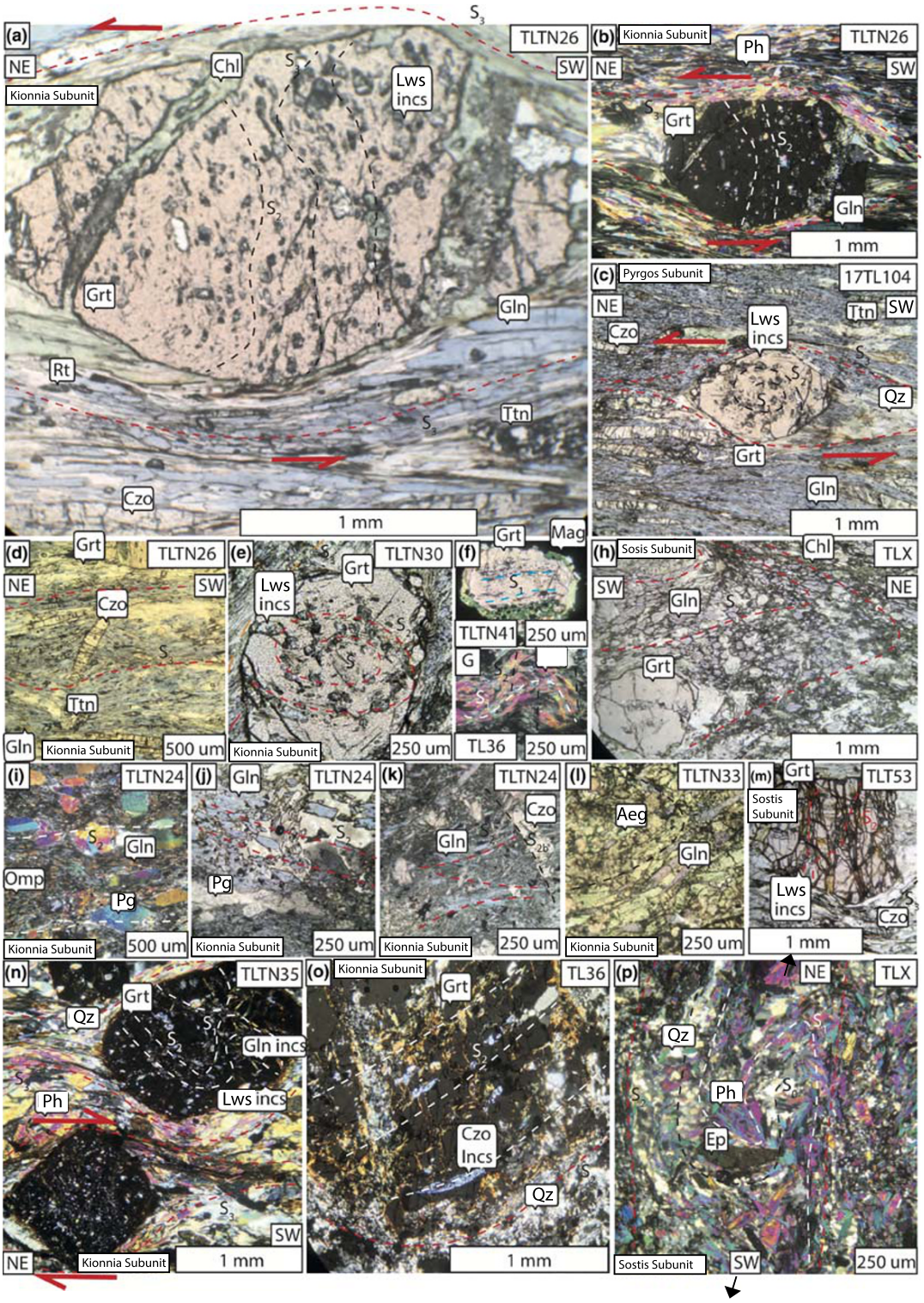

Figure 8. Photomicrographs of prograde features: (a and b) Discordance between S_2 internal garnet fabric and top-to-NE S_3 fabric. (c and e) Rotational fabric defined by ex-lawsonite inclusions discordant to the external fabric. (d) Rotated epidote porphyroclasts that are oblique to the S_3. (f–h) S_{2a} fabric within garnet porphyroclasts and affecting matrix Gln and Ph. (i) Coarse crosscutting paragonite laths that appear late. (j) Intergrown matrix Gln and Pg defining the S_{2a}. (k) Crosscutting Czo across fine acicular matrix glaucophane. (l) TLTN33 partially hydrated eclogite facies assemblage of grt with aeg-omp and cross-cutting gln matrix. (m–o) folded pseudomorphed lawsonite inclusions in garnet and affecting the matrix Gln and Ph. Note that TL36 rim contains a Czo inclusion and therefore grew under Czo stability (instead of lawsonite).

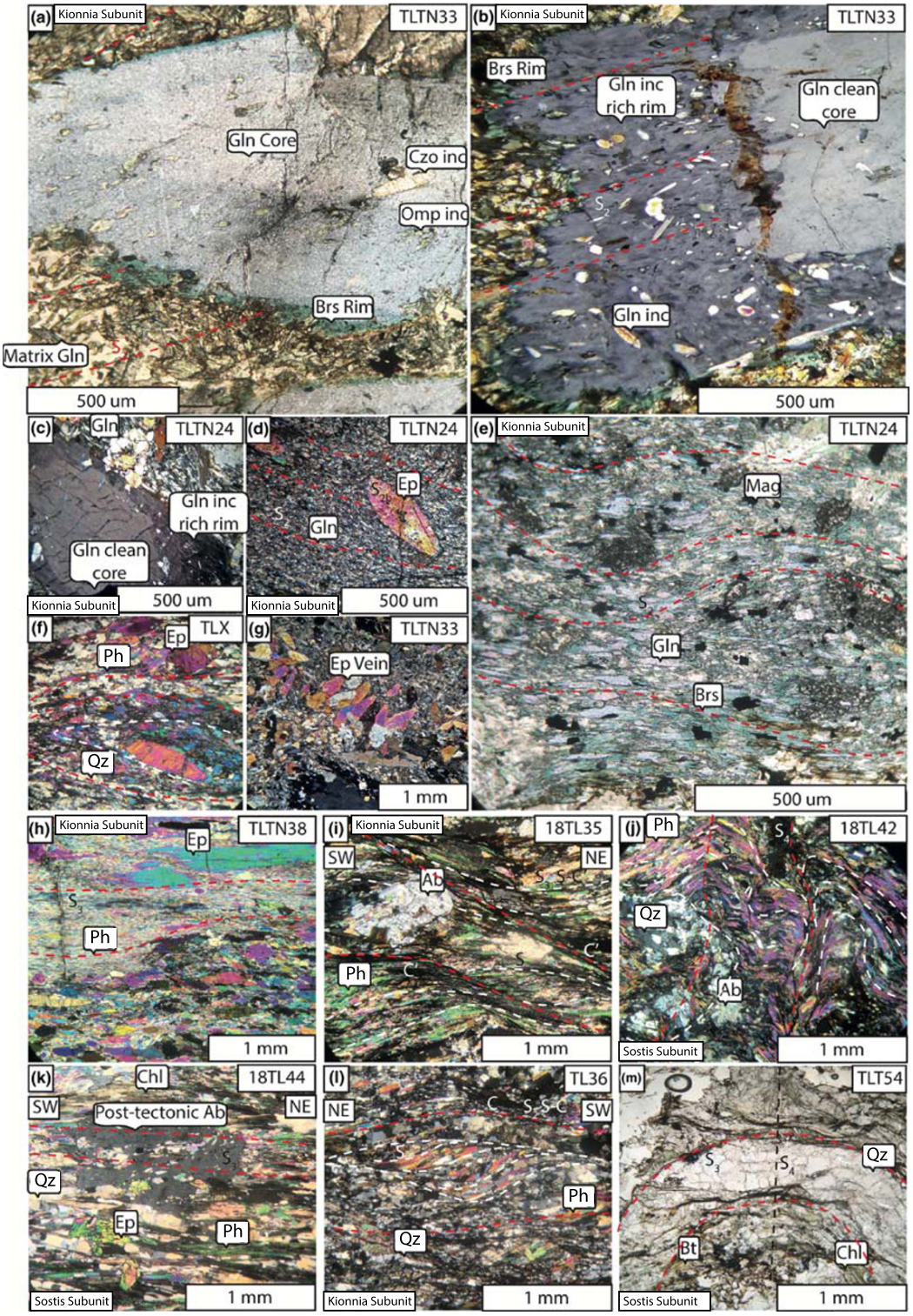

Figure 9. Retrograde photomicrographs: (a–c) TLTN33, coarse matrix crosscutting amphibole with a clean Gln core and an inclusion dominated and green outer rim of Brs-Mbh composition. (d) Coarse crosscutting epidote with fine matrix gln. (e) S_{2b} fabric affecting matrix Gln, which is transforming to Brs with interstitial magnetite. (f) S_{2a} crenulation fabric and (g) crosscutting epidote vein. (h) Crosscutting epidote on fine grained phengite. (i) Top to NE S-C′ S_3 fabric affecting greenschist assemblages. (j) Upright F_4 folds in green schists facies assemblages. (k) Posttectonic albite superimposed on S_3 blueschist facies fabric. (l) S_{2b} top-to-SW fabric on Kionnia Thrust Zone affecting blueschist facies assemblages. (m) Upright F_4 fold in a greenschist facies calcsilicate from the Sostis Subunit.

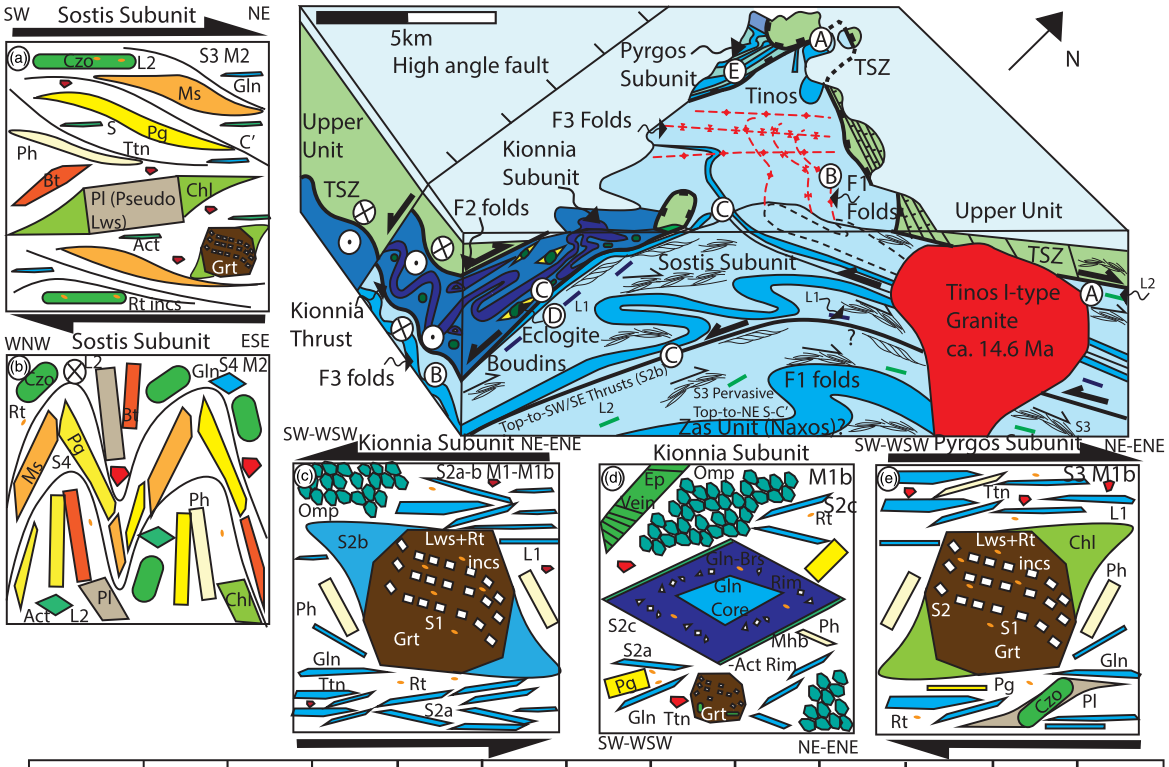

Subunit	Mineral	S1	S2a	S2b	S2c	S3	S4	L1	L2	F1	F2	F3
Kionnia Subunit	Grt											
	Gln											
	Brs											
	Lws											
	Omp											
	Ph											
	Pg											
	Czo											
	Chl											
	Pl											
	Rt											
	Ttn											
Pyrgos Subunit	Grt											
	Gln											
	Brs											
	Lws											
	Omp											
	Ph											
	Pg											
	Czo											
	Chl											
	Pl											
	Rt											
	Ttn											
Sostis Subunit	Grt											
	Gln											
	Brs											
	Lws											
	Act											
	Ph											
	Pg											
	Czo											
	Chl											
	Bt											
	Pl											
	Rt											
	Ttn											

Figure 10. (a–e) Schematic illustration of deformation macrostructures and microstructures on Tinos, showing fabrics, lineations, order of mineral growth with simplified sketches of microstructures described in the text. Mineral abbreviations follow Whitney and Evans (2010). TSZ = Tinos Shear Zone.

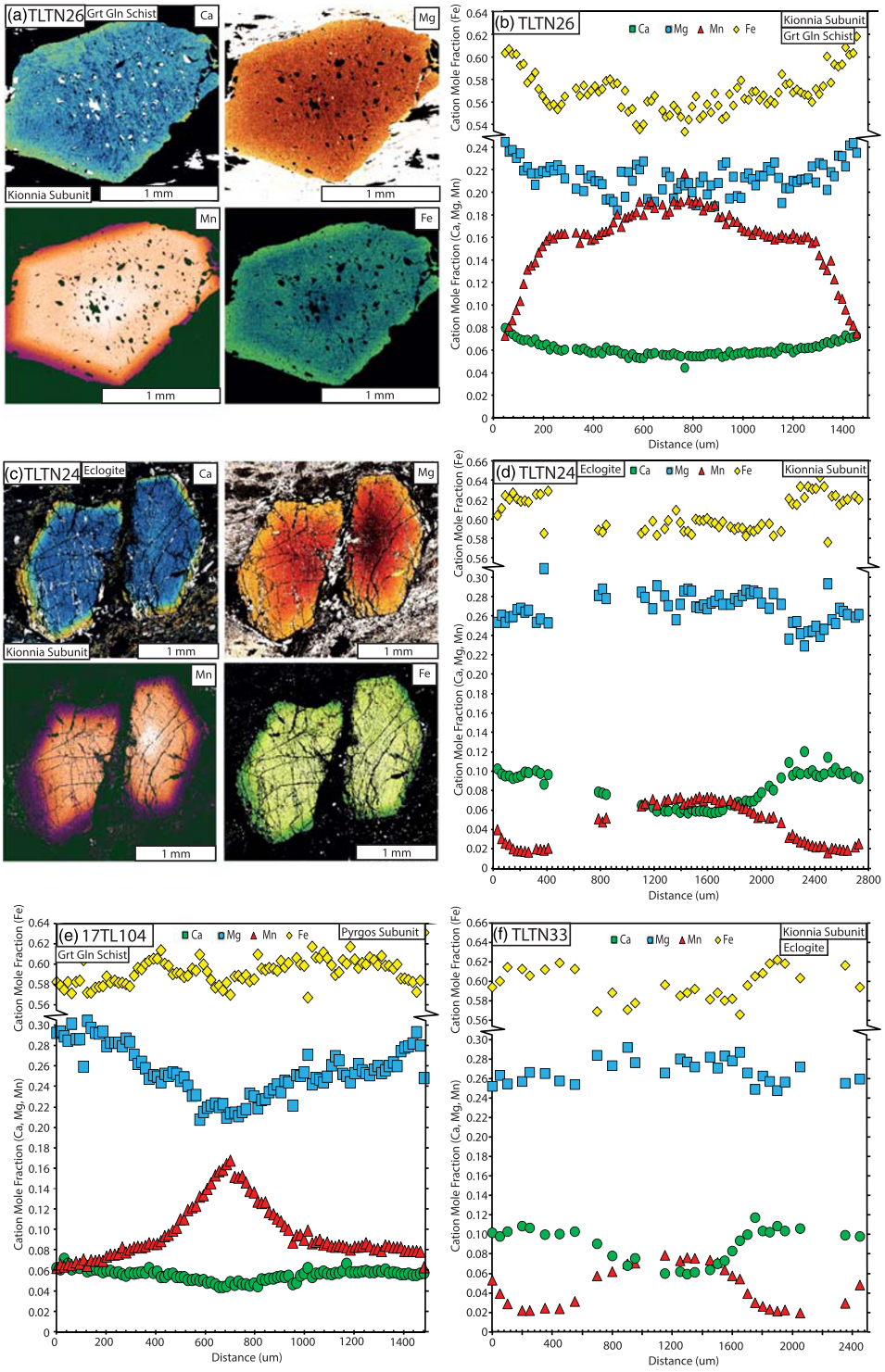

Figure 11. Prograde garnet maps and profiles for Kionnia and Pyrgos Subunit samples showing (a) TLTN26 EPMA maps with rotation textures in the calcium map, indicating garnet grew syntectonic with glaucophane in the matrix and strong spessartine zoning from core to rim, with (b) increasing grossular, pyrope, and almandine. (c) Eclogite TLTN24 garnet EPMA maps and line profiles (d) showing strong grossular and pyrope increases from core to rim with a small inflection in spessartine and almandine affecting the outer most rim. (e) Sharp prograde and symmetrical zoning in blueschist 17TL104 with increasing grossular toward the rim, interpreted as a single growth history. (f) TLTN33 garnet line profile, showing similar trends to TLTN24 but heavily affected by fractures (missing data) and a smoother profile than the blueschists.

affects the sequence and is defined by retrograde blueschist (M_{1b}) matrix phases including glaucophane, phengite, paragonite, and epidote that deforms around garnet porphyroclasts (Figures 8a–8d).

The sense of shear therefore inverts across the subunit with top-to-SW shear (S_{2b}) in the lower half, and top-to-NE shear (S_3) in the upper half. This suggests the subunit is bounded by shear zones that were active during exhumation from the eclogite facies depths. The TSZ truncates the blueschist-eclogite facies structures at the top of the subunit. The TSZ is associated with NE-SW lineations (L_2; defined by actinolite, chlorite, titanite, and plagioclase) and M_2 greenschist facies (S_3) top-to-NE S-C ultra-mylonites (see stereonets in Figure 3) and places Upper Unit greenschists (possibly retrogressed amphibolite metamorphic sole) directly against eclogite facies rocks (N37.552088, E25.124767). Although the very top of the Kionnia Subunit or overlying *HP* rocks are not exposed, it is acknowledged that post M_{1b} (S_3) top-to-NE shearing should become more intense up structural section toward the roof (top-to-NE) shear zone responsible for the exhumation from subduction depths. In contrast, the lower half of the subunit is affected by (S_{2b}) top-to-SW shear. These kinematics are associated with an inverted metamorphic field gradient upward from Kionnia Beach, suggesting the lower contact of the subunit represents a ductile thrust, referred to herein as the Kionnia Thrust (with top-to-SW kinematics affecting M_1 and M_{1b} assemblages) that separates it from the rest of the Lower Unit (Figures 3 and 5).

Between these two structures, the sequence has been recumbently folded (F_1) along ESE-WNW trending hinge lines and are boudinaged parallel to the NE-SW stretching lineation (L_1; see stereonet in Figures 3 and 5). Sheath folds (F_2) display cats-eye geometries (Figure 5) with stretching lineations (L_1; defined by M_{1b} glaucophane, rutile, titanite, chlorite, clinozoisite, and phengite) trending NE-SW/ENE-WSW, indicating they formed coeval with noncoaxial ductile top-to-SW shearing (S_{2b}; Alsop et al., 2007; Alsop & Holdsworth, 2006). NE trending upright and open folds (F_3) are superimposed on these recumbent (F_1) and sheath (F_2) folds (Figure 3). F_3 folds have a regular wavelength of ~100–150 m and have hinge lines parallel to the (L_1) NE-SW stretching lineation. They re-fold both (S_{2a+b}) top-to-SW and (S_3) top-to-NE shear fabrics, indicating they formed due to a component of orthogonal shortening during exhumation (M_{1b}).

Although this sequence has been interpreted as a mélange (Bröcker et al., 1993; Bulle et al., 2010), we find the sequence comparable to the Chroussa Subunit on Syros and is much more coherent than the *HP* serpentine bounded mélanges on Syros (Kampos Subunit: e.g., Keiter et al., 2011; Laurent et al., 2018). The consistent and rhythmic layering of metasediment and eclogite (Figure 6e) suggest the sequence records its primary sedimentary-volcaniclastic origin, with the eclogite representing boudinaged mafic intrusions or lava flows rather than fragments of oceanic crust.

3.1.1. Kionnia Eclogite

Eclogite occur as granoblastic boudins (sample TLTN33) beneath a 25 m thick recumbently folded (m3) marble band (e.g., N37.547909, E25.125488; Figure 5) and as continuously foliated mafic to intermediate horizons (sample TLTN24) intercalated with metapelites structurally above the (m3) marble band (Figure 3). Granoblastic eclogites (TLTN33) display coarse porphyritic (relict igneous) microstructures that are overprinted by eclogite facies (M_1) paragenesis. Major phases include garnet, clinopyroxene, glaucophane, epidote, paragonite, rutile, titanite, and quartz that are distributed between anhydrous clinopyroxene rich domains and more hydrated glaucophane-rich domains (Figures 8i, 8k, and 8l). Garnet forms poikiloblasts containing glaucophane, aegirine-omphacite, lawsonite pseudomorphs (now microcrystalline aggregates of paragonite, plagioclase and clinozoisite), epidote, rutile, and titanite inclusions. Within garnet cores, rutile and lawsonite pseudomorphs inclusions define S_1. Garnet rims lack lawsonite pseudomorphs but contain rutile, titanite, and epidote that define the S_{2a} foliation that is oblique to S_1, but concordant to the external fine-grained glaucophane and clinopyroxene matrix that garnet rims overgrow (Figure 8l). Clinopyroxene is aegirine-omphacite composition (Figure 8; supporting information Text S1) suggesting that the rocks were oxidized during M_1. On the outcrop scale, granoblastic eclogites are coarse grained with garnets up to 2 cm in diameter (Figures 6a and 6b). However, under thin section, much of the matrix clinopyroxene is finely recrystallized and has only a minor crystal preferred orientation that sometimes displays crenulations (S_{2a}) (Figures 8g, 8h, 8k, 8j, and 8p). Both types of eclogite contain several types of blue amphibole. In sample TLTN33, fine prismatic glaucophane (Figure 8l) occurs in the matrix and as inclusions within garnet, follows the S_{2a} and S_{2b} fabrics, and exhibits Na in B site occupancy [Na_B] between 1.75 and 1.96 atoms per unit formula (apfu), interpreted to represent peak M_1 conditions. Secondary, coarse, optically and chemically zoned

glaucophane and epidote porphyroblasts crosscut the (S_{2a+b}) matrix fabrics and contain inclusions of aegirine-omphacite, fine prismatic glaucophane, and rutile and display a clean core and textured, inclusion rich rim (Figures 9a–9c). The cores are glaucophane, with [Na_B] = 1.89–1.98 apfu, Si = 7.96–7.81 apfu, A site occupancy of Na + K [$(Na + K)_A$] = 0.0–0.06 apfu, and XMg [Mg/(Mg + Fe)] = 0.5–0.64 interpreted to represent immediately postpeak M_1. The inner rims are barroisite, with Na_B = 0.57–1.30 apfu, Si = 6.89–7.46 apfu, $(Na + K)_A$ = 0.17–0.49 apfu, and XMg = 0.54–0.72 and the sharp green actinolite-magnesio-hornblende to magnesio-katophorite outer rims have Na_B = 0.41–0.85 apfu, Si = 6.83–7.27 apfu, $(Na + K)_A$ = 0.42–0.85 apfu, and XMg = 0.46–0.62, which is interpreted to have formed during exhumation (M_{1b}). Barroisite and actinolite are also associated with fractured garnet grains. Epidote is similarly zoned with XFe^{3+} (pistacite) [$Fe^{3+}/(Fe^{3+} + Al)$] = 0.09–0.70 (Figure 9d) and occurs as radiating crystals along linear features that postdates the S_{2a+b} fabrics, likely representing a crosscutting fluid vein that was associated with hydrating the rock (Figure 9g) following lawsonite breakdown. Aegirine-omphacite grains vary in size from matrix-aligned laths up to 2 mm in length to <100 μm (Figure 8l) and exhibit minor zoning, with jadeite content [XJd = Na/(Na + Ca)] increasing from the core to the rim (Figures 9l; Table S1 and supporting information Text S1). Paragonite occurs as coarse crosscutting matrix flakes and interpreted to be retrograde, whereas phengite is aligned with the S_{2a+b} foliation and display Si zoning from 3.47–3.52 apfu from core to rim (Table S1). Garnets display a concentric zonation of spessartine [X_{Mn}] indicative of a single episode of prograde growth (Woodsworth, 1977). In Sample TLTN24, garnet core to rim zonation is associated with increasing pyrope [X_{Mg}] (6–10%), increasing almandine [X_{Fe2+}] (60–64%) and decreasing spessartine, whereas grossular [X_{Ca}] remains fairly constant across the core, slightly increases in the inner rim to ~28%, then decreases to ~24% in the outer rim. This corresponds with an inflection in spessartine in the outer rim (Figures 11c and 11d) and is interpreted to reflect minor garnet resorption. Similar patterns in emerge in garnets from sample TLTN33 (Figure 11f). Mafic boudins forming the granoblastic eclogites (TLTN33) are not internally deformed by (S_{2b}) top-to-SW or (S_3) top-to-NE shearing (Figure 5), whereas adjacent metasediments deform around them. This implies the metasedimentary hosts accommodated most of the ductile strain on the margins of the boudins.

3.1.2. Kionnia Blueschist

Garnet-glaucophane schists crop out as semi continuous horizons (TLTN26 Figure 6b) in the upper half of the subunit, structurally above a 10-m-thick band of metapelites and are affected by penetrative top-to-NE shear (S_3) that affects matrix M_1-M_{1b} phases including glaucophane, rutile, titanite, and clinozoisite. Peak M_1 phases include glaucophane, comprising >50% rock volume, matrix phengite, idioblastic garnet with pseudomorphed lawsonite inclusions, rutile, and quartz, whereas M_{1b} phases are confined to the matrix and include clinozoisite, titanite, chlorite, and quartz. Metapelites also show blueschist facies paragenesis, comprising matrix quartz, phengite, paragonite, blue amphibole, chloritoid, pseudomorphed lawsonite, rutile, and garnet up to 2–5 cm in diameter (Figure 6e). Highly retrogressed lawsonite schists crop out at the base of the subunit at Kionnia Beach, with 2 cm lawsonite pseudomorphs that are deformed by top-to-SW (S_{2b}) shear. Lawsonite schists are never in association with garnet suggesting a bulk rock/fluid control to lawsonite growth (Figure 6d). In sample TLTN26, garnet X-ray maps and line profiles (Figures 11a and 11b) reveal a concentric spessartine zonation from core to inner rim, followed by a step decrease in the outer rim, suggesting a two-stage garnet growth history. Grossular contents remain at ~20% across the cores, increase slightly toward the inner rim then increase abruptly to ~24% in the outer rim, albeit ~1% of the variation seems to reflect Ca inheritance from the relict amphibole matrix (S_1-S_{2a}) that garnets overgrow (Figure 11a). Almandine increases from core to rim (54–62%), whereas pyrope only increases from 5–8%. These features suggest prograde garnet growth occurred under lawsonite stability and supports the interpretation that S_1 and S_2 are prograde fabrics, whereas S_3 developed during the second phase of garnet growth as it is retained as a rotation of inclusion trails in the outermost rim. Matrix amphibolies are glaucophane, with Na_B = 1.75–2.0 apfu, Si = 7.70–8.00 apfu, $(Na + K)_A$ = <0.05 apfu, and XMg = 0.57–0.69. The occurrence of blueschist adjacent to centimeter-scale eclogite facies assemblages (Figure 6b) suggests that the growth of omphacite is controlled by bulk composition, hydration, or oxidation state (e.g., Weller et al., 2015).

3.2. The Pyrgos Subunit

In NW Tinos, the Pyrgos Subunit crops out along strike and at a similar structural level to the Kionnia Subunit, on the southern limb of the Tinos dome (Figures 2 and 3). It comprises a series of imbricated

and isoclinally folded (F_1) marbles (mainly m2 and m3) which are intercalated with metasediments and meta-volcanic sequences near the villages of Isternia and Pyrgos (Figures 5a, 7c, and 7i). These rocks preserve the same three structural fabrics as the Kionnia Subunit (with S_1 and S_{2a} only preserved as pseudomorphed lawsonite inclusions in garnet) but are more extensively overprinted by pervasive top-to-NE shear (S_3). Up to 12 marble horizons are laterally discontinuous along strike and bounded by (S_3) top-to-NE shear zones associated with S-C′ fabrics that affect peak (M_1) and retrograde (M_{1b}) blueschist facies assemblages. Isoclinal and recumbent folding in the marbles (F_1) is best seen across Vathi Bay (N37.628424, E25.028671) (Figure 5a). F_1 folds deform the S_2 foliation (defined by glaucophane, phengite, and rutile), verge toward the SW and are displaced, and crosscut by several shear zones with top-to-NE kinematics (S_3). Because top-to-NE shear zones (S_3) deform around and truncate F_1 folds (Figure 4a), it suggests the F_1 folding predates (S_3) top-to-NE shearing. F_1 folds therefore formed on the prograde part of the *P-T* path. In contrast, (S_3) top-to-NE shearing occurred during exhumation (M_{1b}), with the intensity of S_3 top-to-NE fabrics increase toward the top of the subunit. A gentle spaced crenulation (S_4) is orthogonal to the L_1 lineation and affects M_{1b}-M_2 matrix phases including blue-green amphibole, epidote, and plagioclase, suggesting it developed during M_2.

Garnet-glaucophane schists crop out toward the top of the sequence (17TL104, Figure 7i; N37.639889, E25.025361). M_1 phases include glaucophane (>50% volume), garnet, phengite, pseudomorphed lawsonite inclusions within garnet (composed of paragonite, clinozoisite, and plagioclase), and rutile, whereas the matrix contains M_{1b} phases including rutile, epidote, titanite, albite, chlorite, quartz, and minor ankerite. Garnet core to rim zonation is characterized by decreasing spessartine (15–1%), increasing pyrope (3–7%), and increasing almandine (60–64%), whereas grossular remains relatively constant across the core at ~28% but decreases to 22–24% in the outer rim (Figure 11e). The concentric and bell-shaped spessartine profile suggests that diffusion has not significantly affected the original growth zonation, such that the rim composition preserves the composition formed during peak metamorphism. Amphibole ranges from glaucophane-winchite, with $Na_B = 1.59–1.95$ apfu, $Si = 7.48–8.00$ apfu, $(Na + K)_A = 0.00–0.35$ apfu, and $XMg = 0.60–0.70$. Epidote occurs as elongate grains and in very fine-grained clusters, with pistacite = 0.24–0.29. Phengite occurs as small matrix-aligned (S_3) flakes, with Si = 3.40–3.51 apfu.

3.3. Sostis Subunit

The Sostis Subunit makes up the deepest structural levels of Tinos (Figure 2). It comprises meta-psammites and metapelites that are intercalated with meta-volcaniclastic lithologies and several <15 m thick dolomitic marble bands (m1-m2) (Bröcker, 1990; Melidonis, 1980), which are recumbently folded on a km scale (F_1). Very rare, meter-scale outcrops of serpentinite occur along shear zones, particularly near Tinos Town. Unlike the overlying subunits which preserve fresh M_1 assemblages, this thick package of rocks is affected by a very strong M_2 overprint. However, rare garnet and glaucophane bearing rocks preserve some of its M_1 history (TLX and TLT60). Small occurrences of jadeitites and retrogressed eclogite have been reported on the north coast, close to the listvenites described by Hinsken et al. (2017) (M. Bröcker, personal communication, October, 2019), although were not found in this study. Several highly retrogressed mafic horizons crop out as boudinaged blocks within the metasediments (Bulle et al., 2010) but are laterally discontinuous and extensively overprinted by M_2 assemblages. It is unclear what these mafic bodies represent. They could be interpreted as (1) mafic sills that intruded the Cycladic-Adriatic continental margin prior to subduction or (2) metagabbros that represent fragments of oceanic that were entrained into the host metasediment during subduction/exhumation (Bulle et al., 2010).

The same three fabrics can be identified within Sostis Subunit samples at thin section scale (Figures 8 and 10). S_1 is only preserved within garnet cores and is defined by pseudomorphed lawsonite, rutile, and sometimes glaucophane inclusions within epidote (Figures 9 and 10). Rutile and pseudomorphed lawsonite inclusion trails in garnet cores rotate toward garnet rims (S_{2a}) but are still discordant to the external (S_3) greenschist facies top-to-NE matrix foliation that deforms around garnet. S_{2a} crenulations are preserved within low-strain matrix domains represented by interlocking grains of phengite that form herringbone structures. All peak M_1 metamorphic assemblages (Grt + Gln + Ph + Lws + Chl + Rt + Qz) are prekinematic with respect to (S_3) top-to-NE shearing. Clinozoisite forms lath-like porphyroblasts with their long axes parallel to subparallel with the (M_{1b}) S_3 foliation. Plagioclase grains are affected by S_3 producing

Tectonics

10.1029/2019TC005890

Table 1

Summary of P-T Results for Samples Investigated in This Study, Distributed Across All Subunits Within the Cycladic Blueschist Unit on Tinos

Sample description				THERMOCALC average *P-T*								Grt-Cpx-Phg barometry Waters and Martin, (1993)		Grt Cpx thermometery				Hbl-Pl thermometry Holland and Blundy, (1994)		Ti in Bt thermometry Henry et al., (2005)	
														Powell (1985)		Krogh Ravna (2000)		Ed-Tr	Ed-Ri		
Unit	Sample	Rock type	location	End members included	X(H_2O)	Temp (°C)	S.D. (°C)	Pressure (kbar)	S.D. (kbar)	corr	fit	no. reactions	Pressure (kbar)	S.D. (kbar)	Temp (°C)	S.D. (°C)	Temp (°C)	S.D. (°C)	Temp (°C)	Temp (°C)	Temp (°C)	S.D. (°C)
Kionnia Subunit	TLTN26	Blueschist	Grt rim	py-gr-alm-gl-fgl-mu-cel-fcel-clin-daph-ames-law-q-H_2O	1.00	499	19	19.7	1.4	0.382	1.67	6	—	—	—	—	—	—	—	—	—	—
			Grt Core	py-gr-alm-gl-fgl-mu-cel-fcel-daph-law-q-H_2O	1.00	492	16	19.3	1.3	0.607	1.21	4	—	—	—	—	—	—	—	—	—	—
			Grt Core	py-gr-alm-cz-fgl-mu-cel-fcel-pa-daph-law-ru-sph-ta-q-H_2O	1.00	487	11	17.7	0.8	0.908	0.89	7	—	—	—	—	—	—	—	—	—	—
	TLTN33	Granoblastic Eclogite	Grt Core	py-gr-alm-di-hed-jd-gl-fgl-mu-cel-fcel-pa-law-q-H_2O	1.00	493	14	19.1	1.1	0.893	1.16	5	18.01	2.88	428	15	400	112	—	—	—	—
			Grt RimA	py-gr-alm-di-gd-cz-gl-fgl-law-q-H_2O	1.00	536	26	22.0	2.0	0.919	1.39	4	22.40	2.92	547	17	500	86	—	—	—	—
			Grt RimB	py-gr-alm-di-hed-jd-acm-cz-ep-gl-fgl-rieb-law-ru-sph-q-cc-H_2O-CO_2	0.99	557	36	21.7	3.3	0.941	1.85	9							—	—	—	—
			Retrograde Matrix	di-hed-jd-fact-ts-parg-an-ab-q-sph-ru-H_2O	1.00	540	20	13.0	0.4	—	0.92	5	—	—	—	—	—	—	517–588 (546 ± 12)	485–645 (589 ± 27)	—	—
	TLTN24	Foliated Eclogite	Grt Core	py-gr-alm-di-hed-jd-gl-fgl-mu-cel-fcel-pa-law-q-H_2O	1.00	501	16	18.5	0.8	0.840	1.01	7	18.08	2.77	497	17	467	67	—	—	—	—
			Grt Rim	py-gr-alm-di-hed-jd-mu-cel-fcel-pa-law-q-H_2O	1.00	509	20	19.0	1.0	0.866	0.93	5	22.58	2.91	560	16	574	65	—	—	—	—
			Retrograde Matrix	—	—	—	—	—	—	—	—	—	—	—	—	—	—	—	323–579 (446 ± 69)	423–500 (460 ± 69)	—	—
	TL36	Retrogressed Pelitic-Eclogite	Grt Rim	py-alm-tr-fact-ts-mu-cel-fcel-cz-law-q-H_2O	1.00	583	21	23.1	1.4	0.977	0.87	5	—	—	—	—	—	—	—	—	—	—

Tectonics

10.1029/2019TC005890

Table 1
Continued

Sample description					THERMOCALC average *P-T*									Grt-Cpx-Phg barometry Waters and Martin, (1993)		Grt Cpx thermometery				Hbl-Pl thermometry Holland and Blundy, (1994)		Ti in Bt thermometry Henry et al., (2005)	
																Powell (1985)		Krogh Ravna (2000)		Ed-Tr	Ed-Ri		
Unit	Sample	Rock type	location	End members included	X(H_2O)	Temp (°C)	S.D. (°C)	Pressure (kbar)	S.D. (kbar)	corr	fit	no. reactions	Pressure (kbar)	S.D. (kbar)	Temp (°C)	S.D. (°C)	Temp (°C)	S.D. (°C)	Temp (°C)	Temp (°C)	Temp (°C)	S.D. (°C)
			Retrograde Marix	an-ab-mu-cel-fcel-pa-ann-tr-fact-ts-parg-clin-daph-q-sph-ru-H_2O	1.00	576	28	15.4	1.3	0.773	1.46	8	—	—	—	—	—	—	—	—	—	—
Pyrgos Subunit	17TL104	Blueschist	Grt Core	py-alm-cz-ep-mu-cel-clin-gl-fgl-rieb-law-ru-q-sph-H_2O	1.00	468	12	15.3	0.8	0.953	0.34	5	—	—	—	—	—	—	—	—	—	—
			Grt Rim	py-gr-alm-cz-ep-mu-cel-clin-daph-gl-fgl-rieb-law-ru-sph-q-H_2O	1.00	496	15	17.2	1.1	0.931	1.49	7	—	—	—	—	—	—	—	—	—	—
	17TL48	Retrogressed Pelitic-Blueschist	Matrix	daph-ames-mu-cel-fcel-cz-law-ru-q-sph-H_2O	1.00	488	29	17.0	1.9	0.968	1.88	3	—	—	—	—	—	—	—	—	—	—
Sostis Subunit	TLX	Pelitic Blueschist	Grt Core	py-gr-alm-gl-fgl-mu-cel-fcel-cz-clin-daph-ames-q-ru-sph-law-H_2O	1.00	493	20	17.3	1.4	0.914	2.2	8	—	—	—	—	—	—	—	—	—	—
			Grt rim	py-gr-alm-gl-fgl-mu-cel-fcel-cz-clin-daph-q-law-H_2O	1.00	510	18	18.6	1.2	0.918	1.69	6	—	—	—	—	—	—	—	—	—	—
	TLT53	Retrogressed Calc-schist	Grt Rim + Matrix	py-gr-alm-cz-mu-cel-clin-daph-law-sph-ru-q-cc-H_2O-CO_2	0.90	536	14	7.5	0.6	0.959	0.99	5	—	—	—	—	—	—	—	—	—	—
	TLT60	Retrogressed Pelitic-Blueschist	Grt Rim+ Matrix	py-gr-alm-cz-mu-cel-clin-daph-law-sph-ru-q-H_2O	1.00	502	10	18.2	0.7	0.920	1.01	5	—	—	—	—	—	—	—	—	—	—
	TLT59	Retrogressed Psammite	Bt	—	—	—	—	—	—	—	—	—	—	—	—	—	—	—	—	—	408–617	13–26

sigma-type porphyroclasts with top-to-NE kinematics (Figures 8 and 9), although some plagioclase porphyroblasts clearly postdate shearing (Figure 9k). Plagioclase trap epidote and rutile inclusions, signifying they postdate M_{1b} and grew at much lower (M_2) pressures. Top-to-NE shearing (S_3) therefore developed over a range of pressures, initiating prior to plagioclase growth (M_{1b}) and continued into the greenschist facies (M_2). The final phase of deformation developed upright crenulation cleavages (S_4; Figures 9j and 9m) that are associated with centimeter-millimeter-scale (F_4) folds trending NE-SW. These features are superimposed on S_3 and cause kinking and folding of phengites and muscovite and suggest a component of E-W shortening during exhumation (Figures 10j and 10m). Quartz grains exhibit incipient recrystallization by grain boundary migration (Figures 9k and 9l), which suggests M_2 deformation temperatures >500°C (Stipp et al., 2002).

Top-to-SW/SE sensed shear zones (see stereonets in Figure 3) crosscut the sequence and are associated with extreme grain size reduction of M_1 and M_{1b} assemblages and form S-C microstructures (S_{2b}). These structures oppose the pervasive normal sense (S_3) top-to-NE kinematics and demonstrate reverse sensed offsets suggesting they are thrusts. The Sostis Thrust, at Sostis Bay (N37.534477, E25.223566), is associated with intense (S_{2b}) top-to-WSW mylonitization and displaces the marble band in in its hanging-wall (Figures 7a and 7b). A top-to-SW shear zone near Tinos Town crosscuts the subunit and juxtaposes the Akrotiri Unit (Upper Unit) against retrogressed meta-psammites and calc-schists. All these structures are truncated by the greenschist facies (M_2) (S_3) top-to-NE shear and the NE-SW L_2 lineation associated with the TSZ (see stereonet in Figure 2).

Kilometer-scale recumbent folds (F_1) are exposed in central Tinos on the northeast face of Mount Exomvourgo (N37.612590, E25.111204), to the SW of Kalloni, and Aetofolia villages and in east Tinos associated with the Sostis antiform (Figure 2). These folds (Figures 7d and 7e) have an ENE vergence and have N-S striking hinge lines (see stereonet in Figure 2). F_1 folds form directly above high-strain zones associated with intense isoclinal and (F_2) sheath folding in marble bands. F_1 folds are interpreted as hanging-wall antiforms above ductile top-to-SW thrusts, which were responsible for thickening and structurally repeating the metasedimentary sequence. A series of dacite dykes intrude through the sequence and are related to the Tinos granite (Brichau et al., 2006, 2007; Lamont, 2018). We do not find any evidence for a Basal Unit in Panormos Bay, in agreement with Bröcker and Franz (2005), although it is acknowledged that the dolomitic marbles are much thicker in this location and are affected by more intense M_2 retrogression associated with the overlying TSZ that crops out at Planitis Island.

In metapelite sample TLX, garnets show core to rim zonation with decreasing spessartine (5–1%) (Figure 11) increasing pyrope (4–6%), and increasing almandine (60–64%), whereas grossular remains 27–29% across the core. All amphibole is glaucophane-winchite, with Na_B = 1.84–2.0 apfu, Si = 7.87–8.00 apfu, $(Na + K)_A$ = 0.00–0.10 apfu, and XMg = 0.54–0.61. Epidote is present in the matrix as elongate grains and in very fine-grained clusters, with pistacite = 0.24–0.29, and small matrix-aligned phengite flakes, exhibit Si = 3.40–3.51 apfu.

3.4. Artemije and Efstathios Shear Zone, NW Tinos (AESZ)

The Artemije and Efstathios Shear Zone (AESZ) in NW Tinos (Figure 2; N37.655951, E24.992683) is ~400 m thick and cuts through the Pyrgos Subunit. It is characterized by intense (F_1) SW verging parasitic folding, which affects both metasedimentary layering (S_0) and a planar foliation (S_1), whereas crenulation cleavages (S_{2a+b}) develops axial planar to these folds. Well-developed (S_3) top-to-NE S-C′ fabric, crosscut the limbs of these folds and is associated with a blueschist and greenschist facies lineation (L_2) parallel to the shear direction (230/30). Although this structure dips toward the SW, its original geometry would have dipped gently to the NE after restoring the late doming. M_{1b}-M_2 phases are affected by top-to-NE shear (S_3), indicating this normal-sensed structure was active during exhumation from subduction-crustal depths. The degree of (S_3) top-to-NE shearing intensifies up structural section, and eventually discontinuous horizons of serpentinite and actinolite schists crop out on the northern coastline (see supporting information Text S1).

3.5. Tinos Shear Zone

The Tinos Shear Zone (TSZ) is a normal-sensed (M_2) greenschist facies structure ~500 m thick that bounds the top of the Lower Unit (CBU; Figure 2). It is associated with top-to-NE kinematics (Mehl et al., 2005) in M_2 assemblages and is discordant to and truncates the M_1 blueschist and eclogite facies structures,

suggesting it was not responsible for the exhumation from subduction depths. The structure outcrops on both the north and south coastlines, suggesting that it is folded around the island about an ENE-WSW axis (see stereonet of L_2 lineations on the TSZ in Figure 2). The gentle NNE dip of this structure on the island's northern coastline is responsible for the exposure of the Upper Unit including the Tsiknias Ophiolite as klippe on structurally high topography such as Mt Tsiknias (N37.581047, E25.225637). The TSZ is crosscut by the Tinos I-type granite and several smaller S-type intrusions, indicating it was active prior to granite emplacement (ca. 14.6 Ma; Brichau et al., 2007; Lamont, 2018) and may have been active at circa 21 Ma based on an Rb-Sr age close to the shear zone (Brichau et al., 2006, 2007; Bröcker & Franz, 1998).

Because the Kionnia Subunit is not exposed elsewhere on Tinos and sits at a structurally high level (Figures 2 and 3), the TSZ must cut it out along strike. The TSZ also cuts out the Pyrgos Subunit in NW Tinos near the village of Marlas and at Panormos Bay places the Upper Unit directly against the deepest levels of the island (Sostis Subunit) (e.g., Avigad & Garfunkel, 1989; Bröcker & Franz, 2000; Jolivet et al., 2010). The TSZ must truncate through all exposed M_1 metamorphic "stratigraphy." It is only on the south coast of Tinos where the thickest section of the CBU is preserved, which entrains the freshest *HP* rocks (Kionnia and Pyrgos Subunits), although rare occurrences of jadeitites outcrop in the Sostis Subunit on the north coast (Bröcker, 1990). The TSZ therefore postdates M_1 conditions and structures related to their exhumation, in agreement with conclusions of Bröcker and Franz (1998), who suggest that the tectonic juxtaposition occurred during M_2 (ca. 23–21 Ma). It is unclear whether the TSZ is related to crustal extension, as normal-sensed top-to-NE shear fabrics only record the relative ductile exhumation of material and cannot characterize a specific tectonic regime (Searle & Lamont, 2019). Although, it is acknowledged that extensive high-angle normal faulting occurs directly above and crosscuts the structure and along the north and south coastlines, which is undoubtedly related to regional extension.

3.6. Marlas Shear Zone

The Marlas shear zone (MSZ) crops out in NW Tinos (Figure 2; N37.654406, E25.032923) and steeply dips northward but displays subhorizontal ENE-WSW trending lineations (see stereonet in Figure 3) that could be interpreted as dextral strike slip kinematics. This structure truncates the Pyrgos Subunit and places the Tsiknias Ophiolite, greenschists, and serpentinites of the Upper Unit directly against pervasively retrogressed *HP-LT* rocks of the CBU. It is possible the structure represented the TSZ but has been folded from its original dip. Alternatively, it could represent a late dextral strike-slip fault that developed at during M_2 that displaces the TSZ and juxtaposes the Lower and Upper Units together.

4. *P-T* Conditions of Metamorphism

The *P-T* results for prograde, peak, and retrograde metamorphic conditions are presented in Table 1 and described below. For further details of the petrographic methods, electron-probe microanalysis (EPMA), mineral chemistry, thermobarometric methods, and equilibrium phase diagram modeling, please refer to supporting information Text S1.

4.1. Thermobarometry

4.1.1. Peak M_1 Conditions

Peak metamorphic conditions for the Kionnia Subunit eclogites were constrained using the garnet-clinopyroxene-phengite barometer (Waters & Martin, 1996) and garnet-clinopyroxene thermometer (Krogh Ravna, 2000; Powell, 1985). Sample TLTN24 yielded 18.1 ± 2.8 kbar and 497 ± 17°C for the garnet core and 22.6 ± 2.9 kbar and 560 ± 16°C for the garnet rim. Sample TLTN33 yielded garnet core *P-T* results of 18 ± 2.9 kbar and 428 ± 15°C and a very similar garnet rim result of 22.4 ± 2.9 kbar and 547 ± 17°C.

Calculated *P-T* results using the THERMOCALC Av-PT function using phase compositions of inclusions trapped within garnet demonstrate two distinct peak M_1 populations. The Sostis Subunit samples (TLT60, TLT53, and TLX) give *P-T* results of 18.5 ± 0.6 kbar, 498 ± 10°C (TLT60). TLX similarly predicts peak conditions of 18.6 ± 1.2 kbar and 510 ± 18°C within error of TLT60 result (see Table 1). In contrast, the Kionnia Subunit reached slightly higher pressure M_1 blueschist facies conditions of 20–22 kbar, 500–520°C. TLTN26 garnet cores grew at 17.7 ± 0.8 kbar and 487 ± 11°C, and rims at 19.7 ± 1.4 kbar and 499 ± 19°C. In contrast, eclogite facies samples TLTN24 and TLTN33 yield elevated *P-T* conditions with TLTN33 garnet cores giving 19.1 ± 1.1 kbar and 493 ± 14°C, and garnet rims suggesting 22.0 ± 2.0 kbar and 526 ± 26°C, whereas TLTN24

yields 18.5 ± 0.8 kbar and 501 ± 16°C for garnet core growth and 19.0 ± 1.0 kbar and 509 ± 20°C for garnet rims.

These results overlap with the Grt-Cpx-Ph barometer and Grt-Cpx thermometer on eclogite facies samples. However, Av-PT systematically predicts lower temperatures and pressures owing to inclusion of epidote in the calculated equilibria and therefore represents a lower bound to the peak *P-T* conditions. Despite this, the data still show that all rocks experienced *HP* although the Kionnia Subunit reached slightly higher pressures (~22–23 kbar) during M_1.

4.2. Retrograde M_{1b} and M_2 Conditions

Retrograde M_{1b} conditions were estimated using the Av-PT function in THERMOCALC. Although no symplectites occur in Tinos eclogites and blueschists, many of the large amphibole laths in eclogite sample TLTN33 exhibit thin magnesio-hornblende rims in contact with retrograde matrix albite, pyroxene and titanite and rutile. Thin coronas associated with garnet breakdown also contain fine plagioclase, green amphibole, and epidote; are in contact with pyroxene that crosscut the S_{2b} matrix fabrics; and were also used by this method. M_2 retrograde pressures were also determined using average pressure calculations in Av-PT using the coexisting activities of amphibole, plagioclase, titanite, epidote, and H_2O. Temperatures of 485–570°C were derived independently using the amphibole-plagioclase thermometer of Holland and Blundy (1994) at a reference pressure of 13 kbar, based on Av-PT results. M_{1b} amphibole rim growth yields pressures between 12.6 and 13.7 kbar (±0.8 kbar) between 500 and 600°C. Results were combined with previously calculated temperatures to produce a *P-T* array for amphibole rim growth between 520–570°C and 12.6–13.7 kbar.

Av-PT was carried out for Sostis Subunit sample TLT53 using M_2 phases Grt + Ep + Chl + Ttn + Ms + Pl + H_2O + CO_2, and an XH_2O of 0.9 (minor matrix carbonate present) and yielded a *P-T* result of 7.3 ± 0.7 kbar and 536 ± 16°C. These conditions are also consistent with the Ti in Bt thermometer (Henry et al., 2005) on adjacent sample TLT59, which yields temperatures of 480–560°C. These results imply that the Sostis Subunit decompressed while remaining at high temperature through the upper greenschist facies.

Despite these results, the nature of the prograde and retrograde *P-T* path is poorly constrained using these methods alone, as conventional therombarometry is largely ineffective at constraining peak *P-T* conditions in *HP* rocks (e.g., Stípská & Powell, 2005). Uncertainty in thermobarometry in *HP* rocks arise due the valence state of Fe in omphacite, which biases estimates up temperature, and the lack of constrained activity solution models for Fe^{3+} thus giving associated large uncertainties (typically, >±50°C and ±1 kbar at 1 SD; Powell & Holland, 2008). It is also possible that phase compositions used in thermobarometry are not representative of peak conditions. Hence, phase diagram modeling (pseudosection construction) in THERMOCALC was employed herein as the major tool to harness prograde, peak, and retrograde *P-T* information.

4.3. Equilibrium Phase Diagram Modeling

4.3.1. TLTN26: Garnet-Glaucophane Schist (Kionnia Subunit)

A *P-T* pseudosection for TLTN26 (Figure 12) reveals that the inferred peak assemblage Grt + Gln + Lws + Ph + Rt + Qz (red text) is stable between ~20–24 kbar and 490–500°C. Across the peak field, the amphibole Na_B content ranges between 1.90 and 1.96 apfu, in good agreement with measured compositions. Garnet core (4–5% pyrope, 20–22% grossular) and rim compositions (6–7% pyrope, 22–24% grossular; Figure 12b) constrain the prograde evolution (pink shading, Figure 12) and suggest peak *P-T* conditions of ~24–27 kbar and ~520–540°C (pink polygon) but plotting inside the omphacite stability phase field, in disagreement with lack of observed omphacite. Due to the predicted presence of omphacite in the peak assemblage, a one-step garnet fractionation was carried out, with fractionation of garnet applied along the proposed *P-T* path (Figures 12a and 12b) at 20 kbar and 450°C. The same trends are observed on the resultant fractionated equilibrium phase diagram (Figures 12d–12f), with H_2O-saturated topologies; however, the omphacite producing reaction is shifted to higher temperatures by this procedure. Pyrope and grossular isopleths also shift to lower temperatures and intersect at 22–26 kbar at 500–520°C in the Grt + Gln + Lws + Ph + Rt + Qz field (red text), in good agreement with observations. TLTN26 in outcrop showed variations between omphacite present and omphacite absent domains. However, Figure 12f indicates that minor variations in M(O) through the outcrop could explain this behavior and further shows that the oxidation state of sample

TLTN26 is near the omphacite stability field (Figure 6b), such that minor changes in M(O) could account for omphacite occurrence. The observed assemblage (red text) places tight constraints for M(O) between 0.2 and 0.3 at 22–26 kbar.

4.3.2. TLTN24: Eclogite (Kionnia Subunit)

A *P-T* pseudosection for TLTN24 (Figure 13) shows the peak assemblage Grt + Lws + Gln + Omp + Ph + Rt + Qz is stable at >21 kbar, and 510–560°C. The calculated assemblage does however predict ~1% chloritoid, which is not observed. However, owing to the very low abundance, chloritoid can be volumetrically ignored and could possibly be related to too much aluminum in the modeled bulk composition. The measured range in matrix amphibole ($Na_B = 0.84–0.99$ apfu, Figure 12) constrains this field further, indicating that the peak assemblage is stable at ~540–560°C (green shading), with minor chloritoid predicted. Consideration of garnet core (5–6% pyrope, 26–28% grossular) and rim chemistry (11–12% pyrope, 22–24% grossular) further constrains the prograde evolution of the sample (red shading, Figure 13b). Garnet cores grew at 19 kbar, 510°C, whereas peak *P-T* conditions of ~22 kbar and 540–560°C (green polygon) are calculated from garnet inner rims. Inflection of spessartine and decrease in grossular in garnet outer rim (Figure 11c) is interpreted to reflect garnet resorption during decompression at >560°C, consistent with decreasing garnet modes (Figure 13c). Following the methodology above, fractionation of 50% of the garnet does not affect the peak estimate (Figure 13b). The various constraints imply a prograde *P-T* path (dotted black line, Figure 13) compatible with the composition of amphibole observed as inclusions in garnet (Figure 12). The only phase that does not show a reasonable model fit is phengite, with the calculated Si range of apfu in the peak assemblage field everywhere less than the measured value of 3.50–3.52 apfu, which could be due to a porphyllitic substitution causing a vacancy in the mica.

A titration determined XFe^{3+} (Fe^{3+}/Fe^{total}) value of 0.35 was applied for TLTN24. The effect of oxidation state and the validity of titration value is analyzed using a *P*-M(O) phase diagram (Figure 13d). At the predicted peak pressure of ~22–24 kbar, the observed assemblage is stable between 0.20 and 0.40. At lower M(O), chloritoid is lost from the assemblage (Figure 13d), and at higher M(O), hematite joins the assemblage followed by destabilization of glaucophane and eventually garnet. The same trends and limits apply in temperature space (see supporting information). As M(O) is increased, epidote and hematite join the assemblage. The presence of epidote implies the sample must have been reasonably oxidized (>0.15). The glaucophane-barroisite solvus is invariant of oxidation state, as the top of the solvus (purple line) is met consistently at ~12 kbar.

4.3.3. TLTN33: Eclogite (Kionnia Subunit)

A *P-T* pseudosection for TLTN33 (Figure 14) reveals that the interpreted peak assemblage Grt + Gln + Omp + Lws/Ep + Ph + Rt + Qz (red text) is stable from ~18 to 28 kbar, and 480–600°C, with this upper temperature boundary representing the appearance of kyanite. At ~20 kbar, lawsonite (blue line) is predicted to replace epidote, and at higher temperatures, glaucophane is lost from the assemblage and is replaced by kyanite. Glaucophane becomes less sodic with decreasing pressure until the glaucophane-barroisite solvus extension is met, across which Na_B rapidly decreases from 1.60–1.10 apfu. Two areas are highlighted by shading on Figure 14, which correspond to the range in Na_B of the glaucophane cores and barroisite-magnesiohornblende rims with the former only present at *HP* within the peak field or within the epidote stability region. With these constraints, the composition zoning in large amphibole matrix laths must be retrograde (M_{1b}).

Further constraints on the prograde evolution are provided by consideration of the garnet pyrope and grossular content. Garnet cores are characterized by 6–7% pyrope and 28–32% grossular, whereas garnet rims contain 12–13% pyrope and 25–27% grossular (Figure 14). The colored shaded regions on Figure 14 correspond to where these constraints are met with cores growing at 22–23 kbar 540–550°C, whereas rims correspond to ~24 kbar 570–575°C. All phases show a good model fit except for white mica. In this case, the model does not recreate paragonite found within the matrix and instead paragonite is not predicted until much lower pressures (>13 kbar).

The effect of M(O) is investigated in Figure 14d. At the peak pressure of ~23 kbar, the observed assemblage is stable between M(O) = 0–0.42. This compares with an $XFe^{3+} = 0.31$ derived from the observed mineral assemblage as a guide to oxidation state, implying a good fit with modeled predictions. With increasing M(O), chloritoid and hematite becomes stable at lower pressures (18–21 kbar), whereas at higher pressure

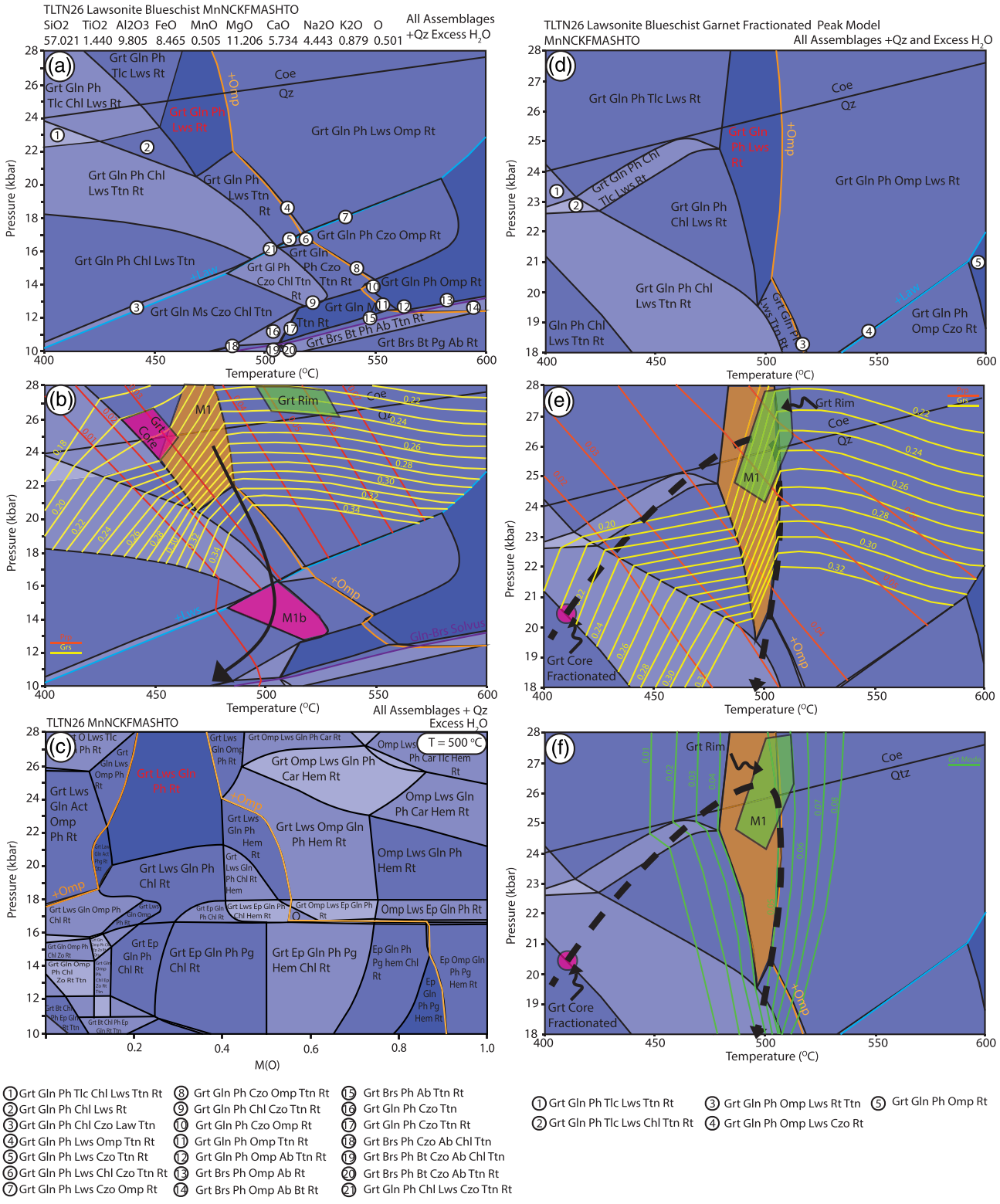

Figure 12. Equilibrium phase diagrams for TLTN26 (a) topology showing the major reactions (lawsonite in; omphacite in; kyanite in and rutile and titanite), (b) overlaid isopleths for grossular (grs) and pyrope (prp) and garnet modal proportions. (c) M(O) pseudosection to investigate the oxidation state on the assemblage field, red text indicates the observed field. (d) Fractionated out garnet core at a hypothetical point on its predicted prograde path (20 kbar, 420°C), phase diagram with the peak observed assemblage in red text and the retrograde matrix assemblage in green text. (f) Overlaid pyrope and grossular isopleths for the fractioned garnet model, which intersect in the observed assemblage field (f) garnet modes, which are mainly temperature sensitive.

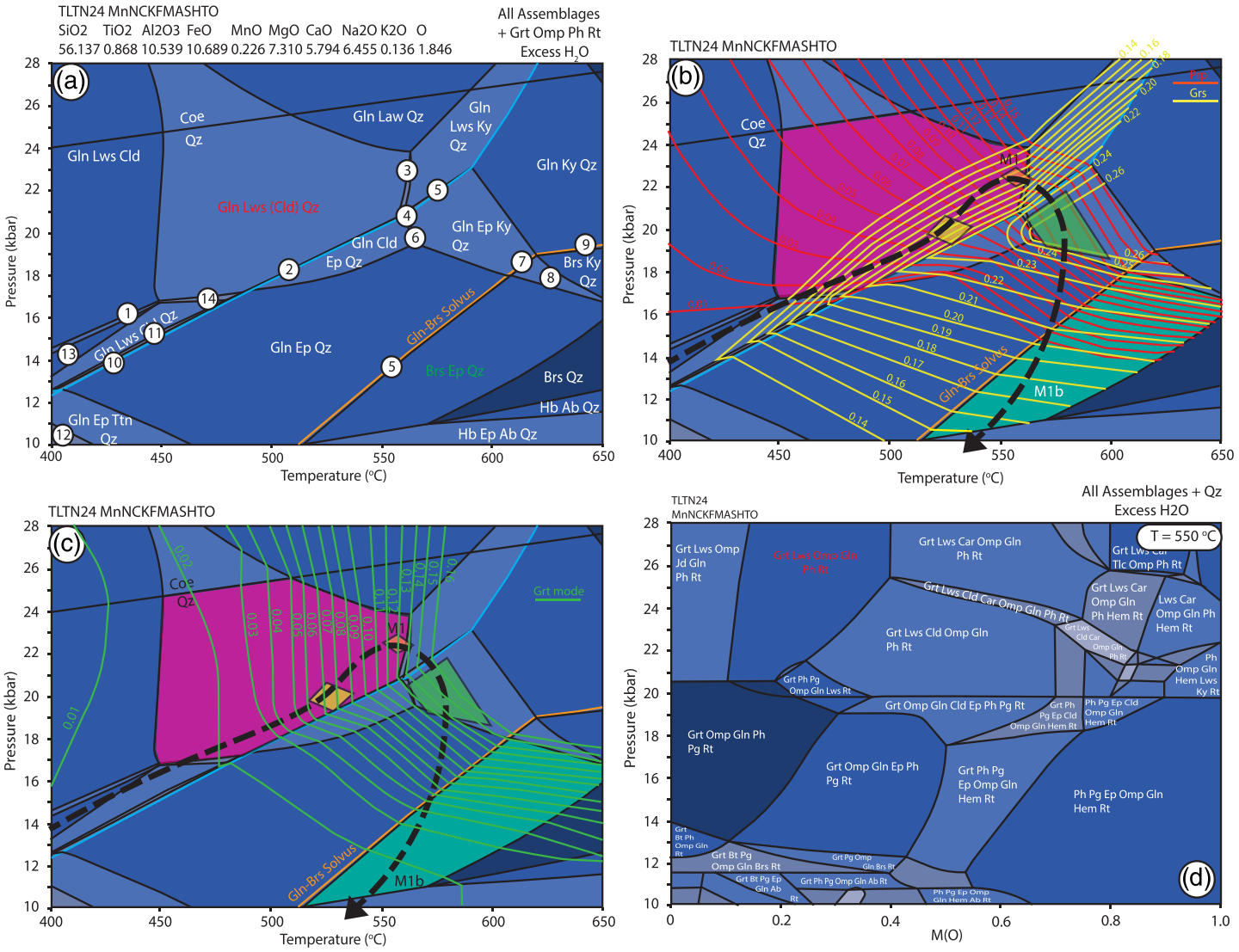

1. Grt Gln Omp Lws Ctd Chl Ph Rt
2. Grt Gln Omp Lws Ep Qz Ph Rt
3. Grt Gln Omp Lws Ctd Ky Qz Ph Rt
4. Grt Gln Omp Lws Ep Ctd Ky Qz Ph Rt
5. Grt Gln Omp Lws Ep Ky Qz Ph Rt
6. Grt Gln Omp Ep Ctd Ky Qz Ph Rt
7. Grt Gln Hb Omp Ep Ky Qz Ph Rt
8. Grt Brs Omp Ep Ky Qz Ph Rt
9. Grt Brs Omp Ky Qz Ph Rt
10. Grt Gln Omp Lws Ep Chl Qz Ph Rt
11. Grt Gln Omp Ep Chl Qz Ph Rt
12. Grt Gln Omp Ep Chl Qz Ph Rt Ttn
13. Grt Gln Omp Lws Chl Ph Rt
14. Grt Gln Omp Lws Ctd Qz Chl Ph Rt

Figure 13. TLTN24 pseudosections using the XRF derived bulk composition showing (a) phase relations and the position of the lawsonite in reaction and Brs-Gln solvus with the peak assemblage in red text and the retrograde M_{1b} matrix assemblage in green text, (b) isopleths of grossular and pyrope that match observed compositions at ~22 kbar and 560°C, (c) garnet modes, which steadily increase up temperature, and (d) a *P*-M(O) pseudosection to evaluate the oxidation state at high pressures; the red text highlights the observed field.

talc becomes stable at M(O) > 0.4, shortly followed by the loss of glaucophane from the assemblage, also suggesting M(O) remained <0.4.

4.3.4. 17TL104: Garnet-Glaucophane-Phengite Schist (Pyrgos Subunit)

A *P-T* pseudosection for 17TL104 (Figure 15) reveals that the inferred peak assemblage Grt + Gln + Lws + Ph + Rt + Qz (red text) is stable between ~20–28 kbar and 470–510°C. Across the

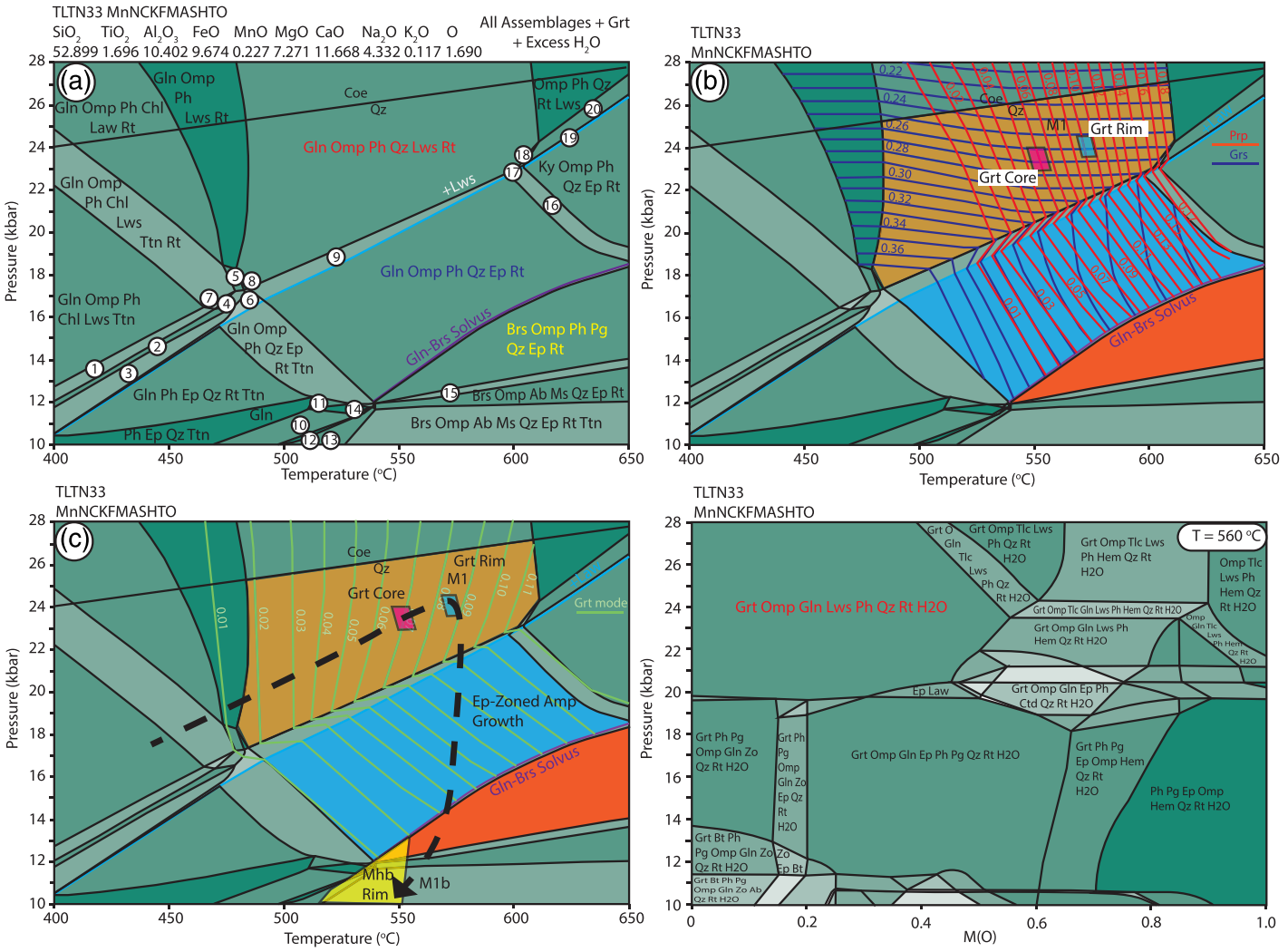

① Gln Ph Omp Chl Lws Ep Ttn
② Gln Ph Omp Lws Ep Ttn
③ Gln Ph Omp Lws Ep Qz Ttn
④ Gln Ph Omp Lws Ep Rt Ttn
⑤ Gln Ph Omp Lws Rt Ttn
⑥ Gln Omp Ph Qz Lws Ep Rt Ttn
⑦ Gln Omp Ph Chl Lws Ep Rt Ttn
⑧ Gln Omp Ph Qz Lws Rt Ttn
⑨ Gln Omp Ph Qz Ep Rt
⑩ Gln Ph Ep Ab Qz Ttn
⑪ Gln Ph Ep Qz Ttn Rt
⑫ Brs Ph Ep Ab Qz Ttn
⑬ Brs Ph Ep Ab Qz Rt Ttn
⑭ Brs Ph Ep Ab Qz Rt Ttn
⑮ Brs Omp Ab Ms Pg Qz Ep Rt
⑯ Brs Ky Omp Ph Qz Ep Rt
⑰ Brs Ky Omp Ph Qz Lws Ep Rt
⑱ Brs Ky Omp Ph Qz Lws Rt
⑲ Ky Omp Ph Qz Lws Ep Rt
⑳ Ky Omp Ph Qz Lws Rt

Figure 14. Equilibrium phase diagram TLTN33, (a) showing the major phase relations with the peak M_1 assemblage in red text and the matrix retrograde M_{1b} assemblage in blue text, (b) pyrope and grossular isopleths showing garnet core and rim intersections, (c) garnet modes, increasing up temperature and pressure, and (d) *P*-M(O) phase diagram to investigate the role of oxidation state on the phase relations.

peak field, the amphibole Na_B content ranges between 1.85 and 1.96 apfu, consistent with measured compositions (Figure 12). Garnet core (4% pyrope, 20–22% grossular) and rim chemistry (6–7% pyrope, 30–32% grossular; Figure 15b) further constrain the prograde evolution of the sample (pink shading, Figures 15b and 15c). Intersection of garnet core isopleths indicate garnet nucleation occurred at ~27 kbar and 490°C in the peak assemblage field. In contrast the grossular rich rims intersect at ~22 kbar and 510°C (pink polygon) but just plotting inside the omphacite stability phase field, in disagreement with lack of observed omphacite in the sample, although minimal omphacite is predicted (<0.02 mode). These results imply 17TL104 experienced decompression as garnet grew from ~27–

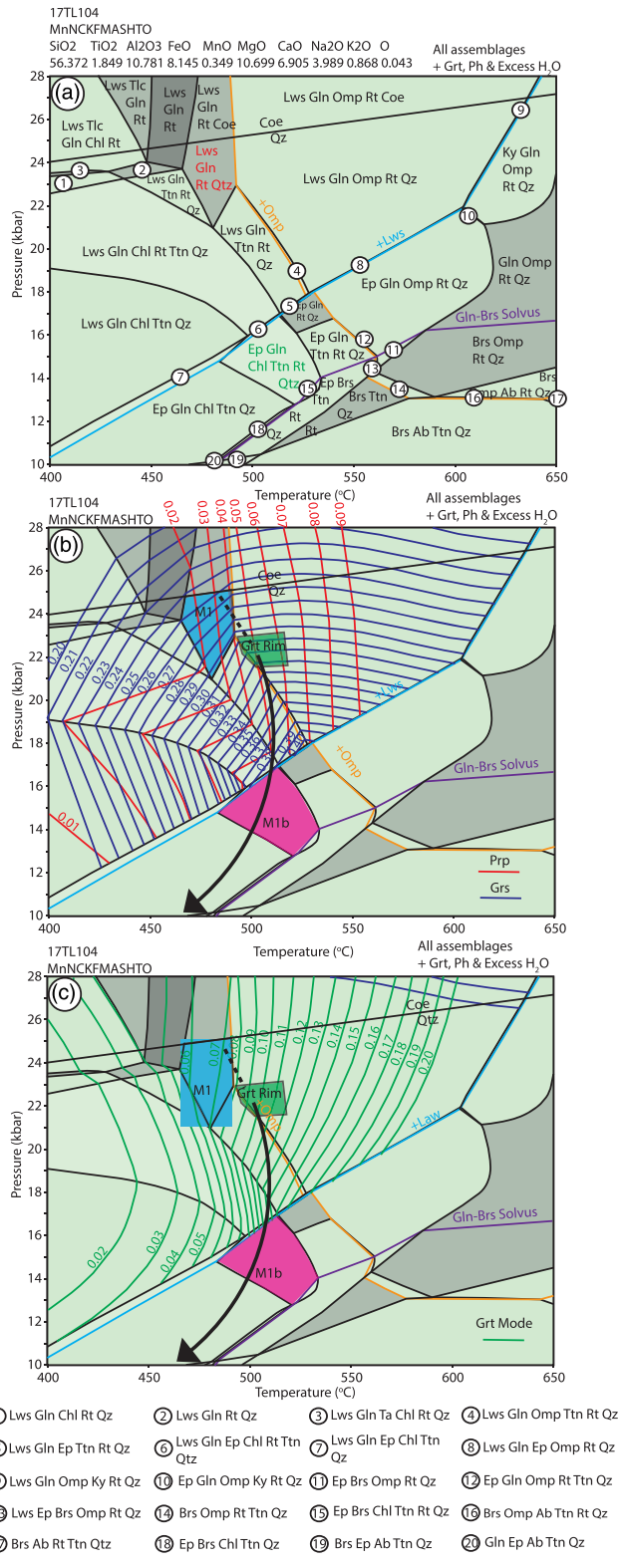

Figure 15. Calculated equilibrium phase diagrams for 17TL104 showing (a) the phase relations, omphacite in reaction (orange line), and the peak M_1 assemblage in red text with the M_{1b} retrograde matrix assemblage in green text, (b) garnet pyrope and grossular compositional isopleths, and (c) garnet modal proportions.

22 kbar while temperatures increased by only ~20°C and is consistent with an increase in garnet mode from 0.06–0.10 between core and rim intersections.

If the garnet core *P-T* result of ~27 kbar is correct, it indicates significant overstepping of the garnet producing reaction and *UHP* conditions were achieved. However, no relict coesite inclusions were found in garnet, and the presence of paragonite and lack of kyanite in metapelitic rocks within the CBU raises ambiguity as to whether this estimated ~27 kbar was experienced. A minimum pressure of ~22 kbar can be rectified based on the predicted assemblage, lack of titanite inclusions in garnet and glaucophane chemistry between 1.90 and 1.96 apfu. This decompression path during garnet growth also suggests S_{2a} and S_{2b} rotational fabrics where associated with the earliest stages of exhumation, thus implying top-to-SW shearing was active during decompression. Further constraints can be placed on the retrograde history associated with growth of matrix epidote, chlorite and titanite. These join the assemblage and coexist together between 470 and 525°C at <17 kbar and coexist until ~12 kbar when the sample crosses the glaucophane-barroisite solvus and plagioclase becomes stable.

4.3.5. TLX: Garnet-Glaucophane Schist (Sostis Subunit)

A *P-T* phase diagram (Figures 16a and 16b) reveals the peak assemblage Grt + Gln + Lws + Ph + Chl + Rt + Qz (red text) is stable between ~18–26 kbar and ~460–540°C. Across the peak field, the amphibole Na_B content ranges between 1.90 and 1.96 apfu, in good agreement with measured compositions. Intersection of garnet core (4% pyrope, 27–29% grossular) and rim (6% pyrope, 27–29% grossular; Figure 16b) isopleths provides further constraints on the sample's prograde evolution (pink shading, Figure 16b) and suggests that garnet cores grew at *P-T* conditions of ~21 kbar and ~480°C (pink polygon), whereas rims grew at 22 kbar 510–520°C in the same field. This implies TLX underwent a dominantly heating *P-T* trajectory during garnet growth, consistent with increases in garnet mode. Although garnet rim isopleths also intersect at ~12 kbar, the predicted assemblage of garnet, barroisite, chlorite biotite, epidote, rutile, and titanite is not consistent with observations of pseudomorphed lawsonites in the garnet cores or Na_B compositions of amphibole. Constraints on the retrograde history can be determined by the lack of biotite in the matrix, implying the rock decompressed through the garnet, glaucophane, epidote, chlorite, and titanite phase field (green text) between ~400–510°C and 10–15 kbar and remained cool during exhumation.

4.3.6. TLT60: Garnet-Mica Schist (Sostis Subunit)

A pseudosection of TLT60 (Figures 16c and 16d) reveals intersection of un-zoned garnet isopleths of pyrope (3–4%) and grossular (28–30%) occurred at ~18 kbar 510–520°C in the Grt + Gln + Ph + Lws + Omp + Rt + Qz phase field. The inferred presence of lawsonite at peak conditions is consistent with relict pseudomorphed inclusions within garnet cores. The model predicts consistent phengite compositions of 3.51 apfu to observations, although no omphacite or glaucophane are present in the current assemblage. This peak *P-T* result is in good agreement with an Av-PT result of 18.5 ± 0.8 kbar and 498 ± 10°C. Upon reaching its peak pressures, the rock decompressed to the M_2

matrix assemblage of Grt + Bt + Pl + Ep + Chl + Ms + Ttn + Qz (green text), stable between 400 and 520°C at >5.5–6 kbar. The upper bound of this M_2 *P-T* estimate is comparable to 7.3 ± 0.9 kbar and 536 ± 19°C calculated for sample TLT53, at a similar structural level.

5. Discussion

5.1. Tectonic Evolution and *P-T-D* Paths on Tinos

Diverse *P-T* paths recorded within the Lower Unit on Tinos (Figure 17) indicate that the CBU is not a single package of rocks, but rather a series of tectonometamorphic slices. Each subunit experienced a different tectonothermal evolution and were juxtaposed against each other during exhumation by a series of top-to-NE ductile extensional shear zones at the top of each subunit, and top-to-SW directed thrusts along their base. The exhumation mechanism of the CBU on Tinos is thus consistent with a model of SW directed synorogenic extrusion from a NE dipping subduction zone, whereby buoyant continental margin derived rocks return from subduction depths via return ductile flow in a channel or extruding wedge due to the positive buoyancy contrast compared to the overriding mantle (Agard et al., 2009; Chemenda et al., 1995; England & Holland, 1979; Hacker & Gerya, 2013; Hacker et al., 2013). An inverted metamorphic gradient (decreasing peak pressure with structural depth) is recorded across Tinos. Although we acknowledge a limitation with the calculated *P-T* is the uncertainties on activity-composition models and the role of local disequilibrium at peak and retrograde *P-T* conditions (Palin et al., 2016). However, this result has also been shown to occur on many other Cycladic islands including Syros and Sifnos (e.g., Laurent et al., 2016, 2018; Roche et al., 2016) and lower pressure blueschists in the Zas Unit at deeper levels of the CBU on Naxos (Lamont et al., 2019).

Although the apparently better preservation of *HP* rocks toward the top of the CBU succession has been previously interpreted to more severe retrograde overprinting/availability of fluids in the lower parts of the CBU during the M_2 event (Avigad, 1998; Avigad & Garfunkel, 1989; Bröcker, 1990; Bröcker et al., 1993, 2004; Katzir et al., 2002), our thermobarometry and field data questions this model. We argue for a major top-to-SW thrust (Kionnia Thrust) and several other structures throughout the CBU on Tinos and importantly, peak M_1 pressures decrease with structural depth. This is consistent with the lack eclogite exposed at deeper levels of the CBU, the pervasive internal shearing, and formation of discrete *HP* mélanges throughout the higher structural levels of the CBU. Both these observations and our *P-T* data are inconsistent with the coherent unit hypothesis. Furthermore, the >6 km structural thickness of the CBU on Tinos is inconsistent with the narrow subduction/exhumation channel (otherwise referred to as the plate interface; Agard et al., 2018) predicted by numerical models for exhumation of *HP* rocks (England & Holland, 1979; Gerya et al., 2002), and geophysical observations of active subduction zones (Abers, 2005; Hilairet & Reynard, 2008). Additionally, many other Tethyan *HP* terranes are not exhumed as coherent units but as discrete thrust sheets or mélanges (e.g., Agard et al., 2018; Brovarone & Herwartz, 2013; Plunder et al., 2016; Searle et al., 2004; Smye et al., 2011). Finally, peak M_1 *P-T* conditions vary across the Cyclades (~26–22 kbar on Tinos vs. ~14.5–12 kbar within the Zas Unit on Naxos; Lamont et al., 2019) supporting a model of progressive (diachronous) stacking of *HP* nappes at slightly different times and depths within the subduction channel or wedge.

In this subduction/extrusion model, underplating would be the dominant mode of accretion, as the active top-to-SW thrust stepped structurally downward with time. This would be combined with normal-sensed shearing also stepping structurally downward on the roof shear zone, allowing for exhumation of earlier subducted rocks up a subduction channel coeval with underthrusting of newly subducted rocks. This is consistent with the occurrence of the South Cycladic Thrust on Ios, which bounds the base of the CBU (Huet et al., 2009), recent interpretations from Syros (Laurent et al., 2018; Philippon et al., 2011; Ring, et al., 2020), the classical underplating model of Platt (1986), and refinements discussed in Agard et al. (2018). The evolution of each subunit is summarized from structurally high-to-low and where possible combined with available geochronology.

5.1.1. Kionnia Subunit

Rocks at the highest structural level of the Kionnia Subunit, reached blueschist facies conditions of ~22–26 kbar and 490–520°C during M_1, significantly higher pressure than previous estimates from Tinos. In contrast, eclogite boudins >200 m structurally below record slightly lower pressures of ~20–23 kbar but higher temperatures of 530–570°C. Although we acknowledge the transition of blueschist to eclogite

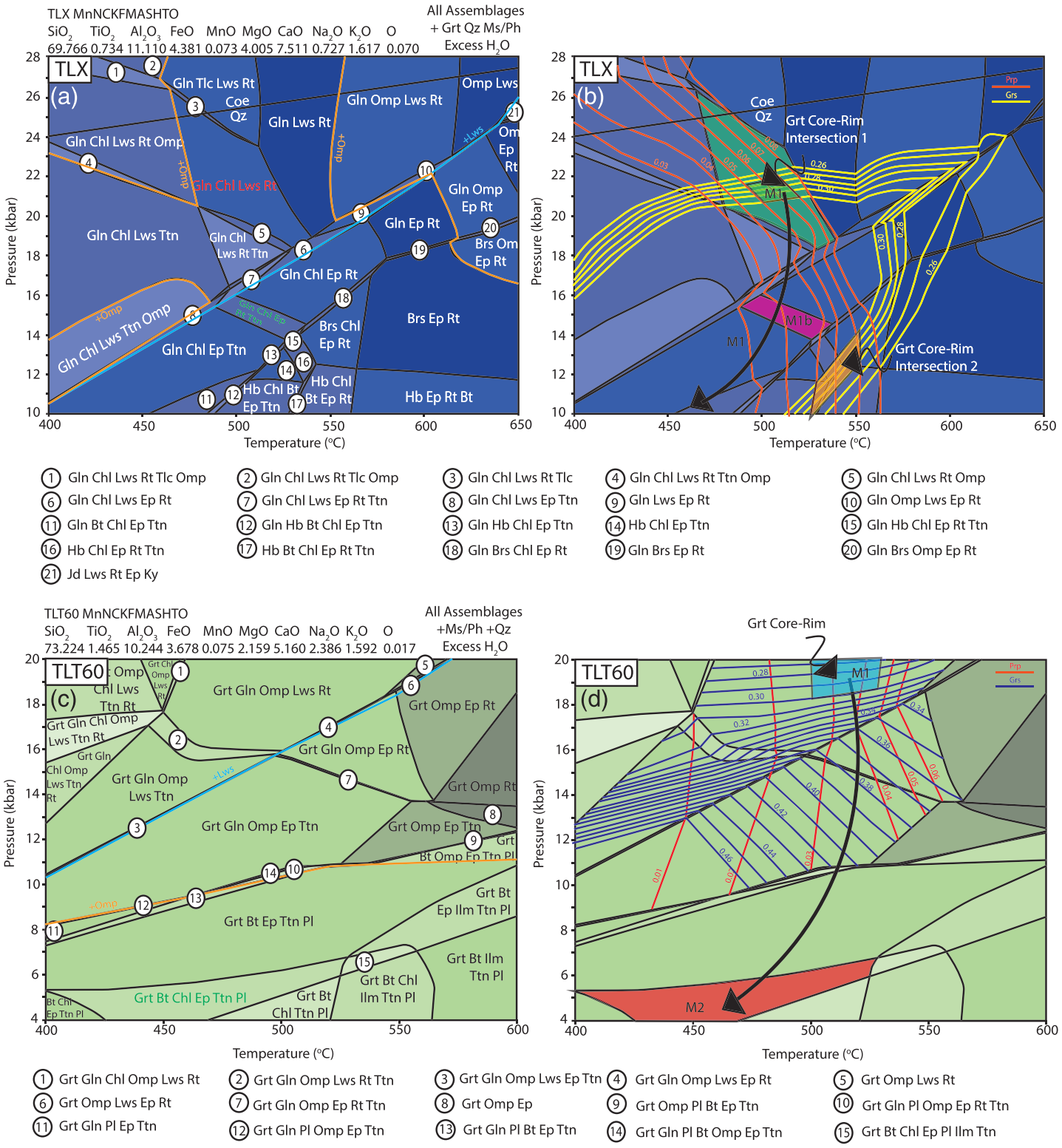

Figure 16. Equilibrium phase diagrams of samples TLX and TLT60 from the Sostis unit, showing the phase relations (a, c) with isopleths of garnet pyrope and grossular (b, d), which show unique points of intersection, red text is the observed phase field for TLX, whereas the green text is the matrix retrograde assemblage.

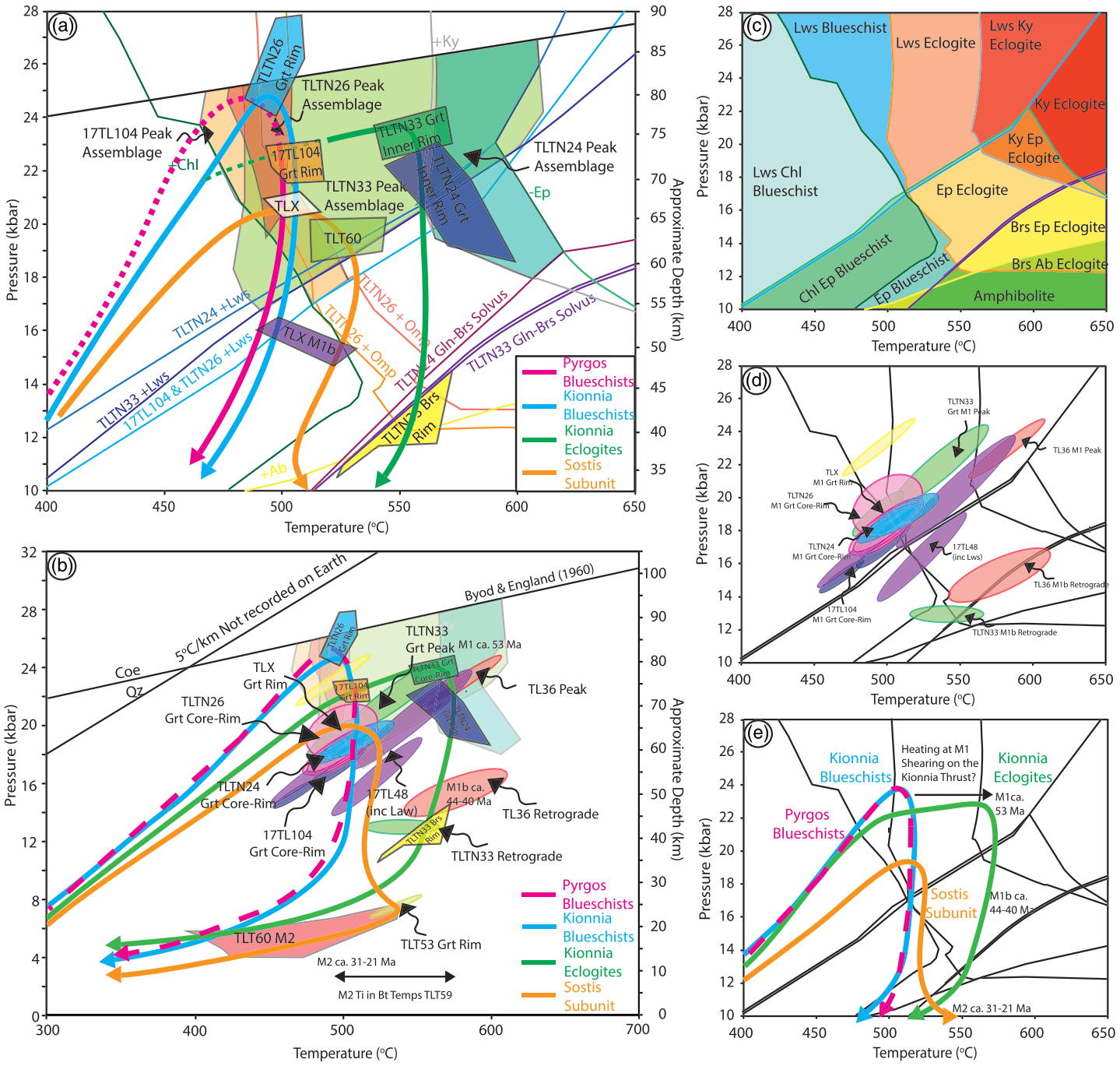

Figure 17. Summary of *P-T* results. (a) Pseudosection constrains of peak metamorphism with overlaid reactions for omphacite, lawsonite albite, and the Gln-Brs solvus with *P-T* paths for each subunit. (b) Conventional thermobarmetry *P-T* constrains with the overlaid coesite-quartz transition from Boyd and England (1960). (c) Approximate metamorphic facies based on a mafic bulk composition (from samples TLTN26 and 17TL104), explaining such high pressures in blueschists before the omphacite in reaction. (d) Thermobarometry of all samples showing variable pressures between the different units. (e) Interpreted *P-T* paths for the Kionnia, Pyrgos, and Sostis Subunits showing possible *P-T* conditions of garnet growth predicted from pseudosection.

facies, defined by the appearance of omphacite, is sensitive to bulk composition and fluid availability, thus allowing both metamorphic facies to be present within the same rock volume at the outcrop scale (e.g., Weller et al., 2015; Figure 5b). The discrepancy in apparent *P-T* conditions across such a narrow deformed zone could be explained by either (1) A temporally evolving geothermal structure with depth within the subduction-accretion system, and subsequent tectonic juxtaposition of eclogite and blueschist during

exhumation. In this model, the upper levels of the Kionnia Subunit were buried deeper under a cooler temperature regime (2–4 kbar equating to ~6–12 km) and were juxtaposed against the underlying (warmer) eclogites by a top-to-SW thrust. This is consistent with top-to-SW fabrics throughout the eclogite facies rocks in lower half of the Kionnia section corresponding to the Kionnia Thrust. This is, however, difficult to justify, as the blueschists are located <200 m away without a clear structural break. (2) Both packages of rocks were buried to similar pressures of ~22–26 kbar and ~500–520°C. At this point during their evolution, the blueschists and eclogites detached from the down-going slab and began buoyancy-driven exhumation toward the Earth's surface. The rocks in the upper half of the Kionnia Subunit remained sufficiently cool to maintain their blueschist assemblages, suggesting that they were located in the middle of the extruding channel sufficiently far away from localized shear zones that would otherwise heat the channel boundaries due to dissipative heating. In contrast, eclogite in the lower half of the Kionnia Subunit (close to the channel boundaries) increased in temperature upon exhumation possibly due to shear heating on the Kionnia Thrust. Although it is acknowledged that fluids may buffer out any extremely localized thermal gradients. This slight increase in temperature during exhumation may also explain the smoother garnet zoning profiles from core to rim in eclogite (TLTN24 and TLTN33) as compositions used to determine maximum pressures may have been affected by diffusion and therefore may only give an apparent prograde *P-T* trajectory. Eclogite garnets also show a spessartine inflection and decreasing grossular in their outer rim, interpreted as garnet resorption with decreasing pressure and increasing temperature. This could be consistent with shear heating during exhumation on the Kionnia Thrust. Irrespective of these speculative scenarios, the heating episode recorded in the eclogite caused lawsonite to decompose, and subsequently rehydrate the rock to form coarse, zoned, and crosscutting epidote and glaucophane after deformation in the eclogite boudin ceased.

U-Pb geochronology from the Kionnia Subunit includes a jadeitite dated at ~63–61 Ma (Bröcker & Enders, 1999), although this likely reflects a mixed age (Bulle et al., 2010), whereas eclogite yields a lower intercept age of 78.2 ± 1.4 Ma (Bröcker & Keasling, 2006), overlapping with the circa 80–76 Ma ages from Syros *HP* metagabbro and plagiogranite in the Kampos mélange that are interpreted to represent magmatic crystallization in a small section of oceanic crust (Tomaschek et al., 2003). If these Late Cretaceous dates are interpreted as metamorphic ages, it would imply a separate *HP* event predating or associated with subduction initiation and ophiolite obduction at circa 74 Ma, which is difficult to fit in with this geodynamic framework. The compatibility of these ages and geochemistry between Syros and Tinos eclogite could be interpreted as the eclogite represent fragments of circa 78 Ma oceanic crust subducted slightly earlier (Bröcker & Keasling, 2006; Bulle et al., 2010). This may explain the warmer eclogite M_1 temperatures. However, this is not supported by our field data, which suggest the Kioinnia subunit is coherently layered and does not show evidence for other fragments of oceanic crust (e.g., meta-cherts, gabbro) and greater than tens of kilometers displacements between the eclogite and its metasedimentary host required by this model. An alternative explanation is the Kionnia eclogite represents a boudinaged sill or dyke that intruded the Cycladic/Adriatic continental margin associated with the same circa 78 Ma magmatic event, which formed a fragment of subducted oceanic crust exposed on Syros, immediately prior to subduction initiation at circa 74 Ma. Two ages on oscillatory zoned zircon from Kionnia eclogite are the best constraints of peak M_1 eclogite facies metamorphism as 53.5 ± 1.6 and 56.7 ± 3.9 Ma (Bulle et al., 2010).

Structural constraints show the Kionnia Subunit was exhumed by a combination of top-to-NE normal-sensed shearing concentrated on the roof shear zone, and top-to-SW thrust sensed shearing at the base (the Kionnia Thrust) (Figure 18). Both normal and thrust sensed shear fabrics show a continuum of deformation from peak to retrograde (M_1–M_{1b}) conditions. The exhumation and deformation history therefore follow an extrusion type mechanism with the Kionnia Subunit overthrusted onto the underlying Sostis Subunit that was not buried to as great depths (Figure 18). The exhumation was associated with the development of F_2 folds and isothermal decompression to conditions of ~13 kbar 520–540°C (e.g., TLTN33), as represented by retrograde matrix phases including coexisting titanite and plagioclase and growth of coarse crosscutting barroisite amphibole rims. Upright open folds (F_3), with their axes trending parallel to the NE-SW shear direction developed during exhumation and were probably related to constriction within the extruding channel, owing to along-strike variations in channel thickness. These features have also been documented across the CBU (Gerogiannis et al., 2019; Xypolias & Alsop, 2014). If there were no variation in along-strike exhumation rates, narrower zones within the channel would produce a component of

convergent flow orthogonal to the main transport direction (e.g., Lévy & Jaupart, 2011; Mancktelow & Pavlis, 1994) toward unrestricted zones.

5.1.2. Pyrgos Subunit

The Pyrgos Subunit records the stacking and folding of the proximal shelf carbonates under peak M_1 blueschist facies conditions of ~22 kbar, 510°C. This result, however, represents a minimum pressure estimate as garnet cores yield up to 27 kbar, 480–490°C. These *P-T* conditions are comparable to that recorded by Kionnia Subunit blueschists (TLTN26) that sits at a similar structural level, although no eclogites have been found in the Pyrgos Subunit. Deformation was comparable to the Kionnia Subunit along strike, with S_1 and S_2 fabrics and (F_1) isoclinal folds forming during burial of the continental margin. This was later overprinted by pervasive top-to-NE shearing (S_3) that developed continuously during exhumation (M_{1b}-M_2) as the unit was extruding toward the SW, which overprints all previous prograde structures.

5.1.3. Sostis Subunit

In contrast to the eclogite and blueschist facies rocks preserved at higher structural levels, the interior of Tinos (Sostis Subunit), achieved less extreme peak pressures and temperatures of ~18–19 kbar, 490–500°C during M_1. It should be noted however, small occurrences of jadeitites and retrogressed eclogite occur on the north coast close to the listvenites reported by Hinsken et al. (2017) (M. Bröcker, personal communication, October 2019), although were not found in this study. Ar-Ar geochronology of white mica from this subunit suggest the minimum age of M_1 conditions were experienced at circa 44–40 Ma (Bröcker et al., 1993) and were affected by extensive M_2 retrogression through the upper greenschist facies at circa 31–21 Ma (Bröcker et al., 1993, 2004; Bulle et al., 2010). Rocks from this subunit underwent a similar prograde style to the overlying blueschists and eclogites and display lawsonite pseudomorphs as inclusions within garnet and within the matrix, and >3.5 Si apfu of phengites. Kilometer-scale (F_1) recumbent eastward verging folds are related to the burial process and the stalling of relatively buoyant metasediments. This presumably occurred upon reaching the point of neutral buoyancy due to entrainment of sufficient continental material. NE trending (F_2) sheath folds within all units are associated with the (S_3) top-to-NE fabrics and presumably also developed during its exhumation from mantle depths. The (top-to-SW) Kionnia Thrust separates this subunit from the overlying (and higher pressure) Kionnia Subunit. The ~4–5 kbar pressure difference between the subunits (~12 km) suggests that the Sostis Subunit was underplated beneath the extruding Kionnia Subunit and achieved its peak pressures (equating to ~60 km depth) at the same time as the overlying Kionnia Subunit was returning back toward the surface. This is because we should expect higher pressures in the Sostis Subunit if underplating occurred at the same time without any differential exhumation. The Zas Unit on Naxos records even lower pressures (~14.5–12 kbar) and represents the more proximal Cycladic/Adriatic continental margin (Lamont et al., 2019). It may be expected that the Zas Unit structurally underlies the Sostis Subunit (Figure 18) and was not buried as deeply.

Retrograde M_2 *P-T* conditions of ~7.3 kbar, 500–540°C, indicate that rocks were exhumed at a minimum rate of ~4 km/Myr and experienced a component of heating once they reached midcrustal conditions. The cause of this heating remains debated. While Avigad and Garfunkel (1991) suggest the heating is related to crustal extension, we argue Barrovian metamorphism is a result of crustal thickening as observed on Naxos, following continental collision between Eurasia and Adria/Cyclades (Lamont et al., 2019; Searle & Lamont, 2019).

In summary, the geometry of the CBU on Tinos does not represent the architecture of the subduction/accretion system at peak M_1 conditions, but rather a snapshot of the lower half of the subduction channel once the subunits were juxtaposed against each other during exhumation (Figures 18 and 19). The *P-T-D* relationships within the CBU suggest that prograde and retrograde deformation progressed down structural level with time as the rocks were sequentially buried and extruded toward the SW from the subduction zone. This implies the extruding channel became wider at shallower depths as more deeply buried extruding subunits became coupled with subunits that did not reach such depths (Figures 18 and 19). This is also consistent with blueschists in Attica that structurally overlie the CBU and did not reach as *HP* but were exhumed from subduction depths by the same extrusion event (Baziotis et al., 2020).

Upon reaching midcrustal (M_2) conditions, the TSZ (associated with top-to-NE kinematics) truncates the *HP* (M_1 and M_{1b}) structures at circa 21–14.6 Ma (Brichau et al., 2007; Bröcker et al., 1993). Deformation on the TSZ was responsible for exhumation of rocks from midcrustal depths much later in the orogenic history. It is unclear whether the top-to-NE extensional fabrics on the TSZ represents overall crustal extension or relative

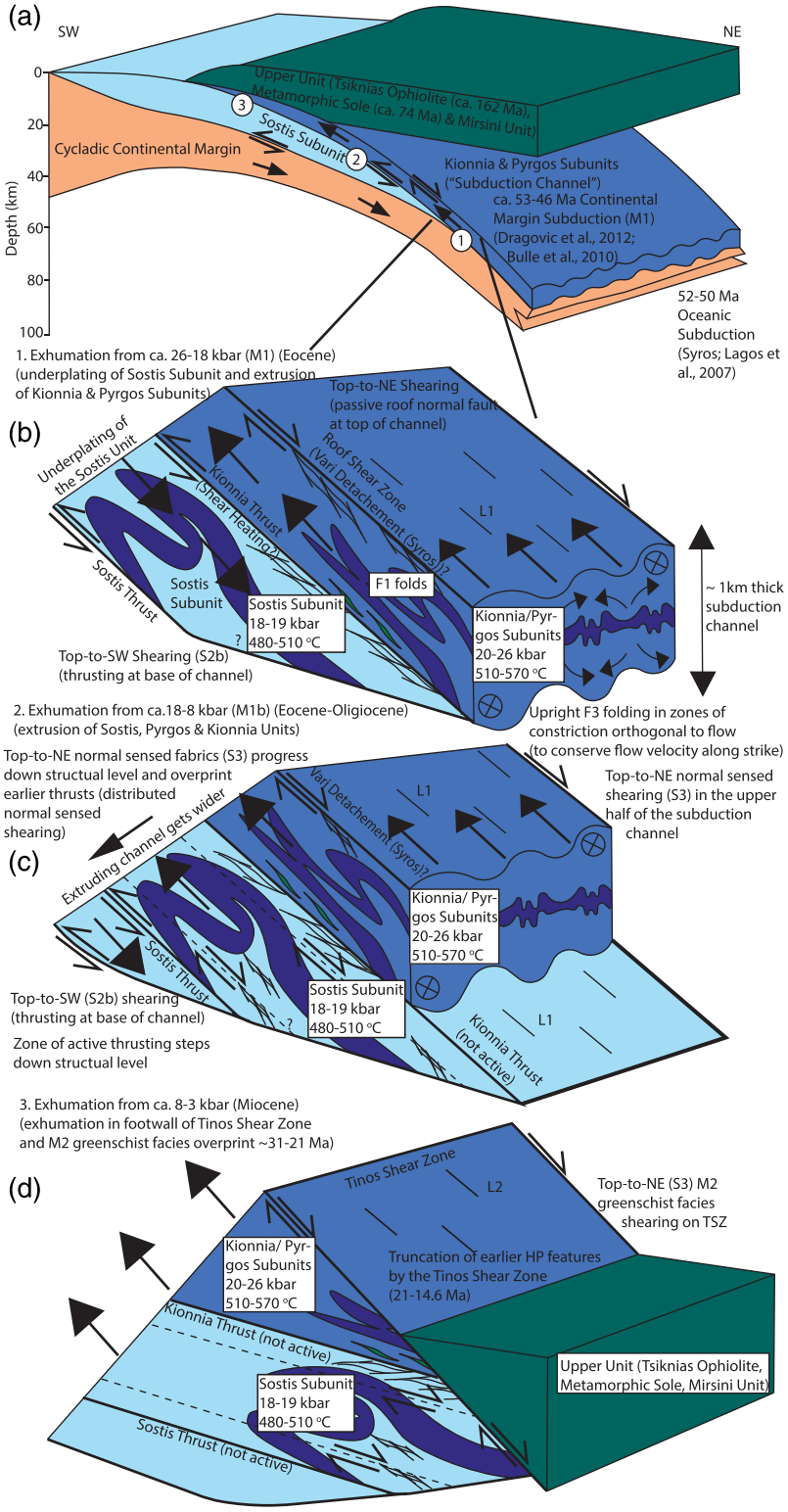

Figure 18. Extrusion model for exhumation of Tinos *HP-LT* rocks: (a) Schematic sketch of a subduction zone with the location of the subduction channel. (b) Extrusion of high-pressure rocks by top-to-SW thrusting at the base and normal-sensed motion at the top, placing higher-pressure rocks on top of lower pressure rocks. (c) Migration of the thrust zone down structural section, causing an overprint of extensional fabrics at the top of the channel. Note lateral variation in channel width can cause localized construction and open folding orthogonal to the transport direction. (d) All high-pressure fabrics are truncated by the Tinos Shear Zone at midcrustal greenschist facies conditions.

extension along a passive roof fault in an overall compressional regime (Means, 1989; Searle & Lamont, 2019). The TSZ was responsible cutting out ~25 Myr of subduction history by juxtaposing the Upper Unit containing the Tsiknias Ophiolite, metamorphic sole, Mirsini Unit (pelagic metasediments) and Akrotiri Units in the hanging wall against the CBU in its footwall.

5.2. Thermal Evolution of the Cycladic NE Dipping Subduction Zone

P-T conditions of ~22–26 kbar and 490–520°C suggest subduction of the Cycladic continental margin to ~70–80 km depth, along a cool geothermal gradient of ~6–7°C/km. Other Tethyan *HP-LT* terranes including Corsica, Elba, Western Turkey, Iran, and Oman record comparably cold geotherms (Brovarone et al., 2011; Davis, 2011; Davis & Whitney, 2006; Hunziker et al., 2017; Papeschi et al., 2020; Plunder et al., 2015, 2016; Ravna et al., 2010; Searle et al., 1994, 2004; Wang et al., 2019; Warren & Waters, 2006), suggesting similar processes occurred along strike at slightly different times.

Thermal modeling of subduction zones shows that considerable conductive cooling occurs in the mantle wedge within the first few million years following initiation, eventually converging on a steady-state system (e.g., Kincaid & Sacks, 1997; Molnar & England, 1990, 1995; Warren et al., 2008). Immediately following subduction initiation, temperatures on the slab top reach ~800–900°C at 70 km depth, enough to trigger melting of the sediments under water-saturated conditions (Kincaid & Sacks, 1997). After this early thermal maximum, slab surface temperatures decrease to a steady state within a few Myr by continued subduction of the cold slab (Kincaid & Sacks, 1997; Molnar & England, 1990, 1995). The thermal evolution of the slab surface is influenced by (1) the subduction rate, (2) the age of the subducting plate, and (3) factors controlling the flux of hot material into the wedge to oppose the cooling effects of the slab (England & Wilkins, 2004; Molnar & England, 1990, 1995), although the age (or thickness) of the overriding plate and the slab dip angle are most influential (e.g., Molnar & England, 1990, 1995). For a fixed dip angle, rapid subduction beneath a thicker overriding plate results in increased cooling of the mantle wedge and generates the coolest slab surface temperatures (England, 2018; Molnar & England, 1990, 1995). In contrast, the maximum slab surface temperatures are recorded in slow subduction zones, where both the subducting and overriding plates are young and thin (England, 2018; Molnar & England, 1990, 1995). Dissipative heating likely plays a role (England, 2018; England & Molnar, 1993; Kohn et al., 2018; Turcotte & Schubert, 1973), although some disregard it as a driving metamorphism and melting (e.g., Abers et al., 2017; Syracuse et al., 2010). Shear stresses of 10–100 MPa are required to explain additional heat flow observations of 40 mW m^{-2} (England, 2018), corresponding to a coefficient of friction on subduction zone interfaces as ~0.05–0.07 (England, 2018). Shear heating thus acts to increase temperatures near subduction zone interfaces with faster convergence rates and has been shown through thermal modeling to be necessary to explain *P-T* conditions recorded in *HP* rocks globally (Kohn et al., 2018; Peacock, 1992).

The cool geotherm during M_1 of ~6–7°C/km, contrasts with >30°C/km recorded in the Tsiknias Ophiolite metamorphic sole associated with subduction initiation (Lamont, Roberts, et al., 2020). This difference can be easily explained if both events were related to the same subduction zone but separated by circa 25 Myr (i.e., ca. 74 Ma vs. 53–46 Ma). During this time, the Upper Unit, including the Tsiknias Ophiolite, metamorphic sole, and Mirsini Unit, must have been accreted in an upper-plate position with the active subduction thrust stepping back and down structural level beneath these features (Figures 18 and 20).

The subducted oceanic plate (i.e., metamorphic sole amphibolites) formed during the early Jurassic (ca. 190 Ma; Lamont, Roberts, et al., 2020), similar to the age of the Cycladic continental margin (Altherr et al., 1982; Andriessen et al., 1979). During subduction initiation at circa 74 Ma, the subducted ocean crust (amphibolites) on the plate interface (The Tsiknias Thrust), reached higher temperatures due to a combination of shear heating and a possible excursion of the mantle wedge (Lamont, Roberts, et al., 2020). In contrast, at the time of M_1 (ca. 53–46 Ma), the subducted oceanic crust would have been circa 140 Myr old and cold, thus cooling the thermal structure of the subduction zone. A minor complication is the circa 78 Ma ages recorded in Syros and Tinos eclogite. If these are interpreted as magmatic protolith ages, it suggests a small fragment of subducted oceanic crust and ocean-continent transition may have been warmer at the time of M_1. However, the heating effect of these rocks is unlikely to be significant if most of the subducted oceanic crust was ~140 Myr older and the upper plate was ~110 Myr old. Using these ages, and the shortest possible time between sole formation (subduction initiation) and *HP-LT* metamorphism of circa 25 Myr, the apparent geothermal gradient in the subducting slab cooled at a rate of ~1.2–1.5°C/km/Myr.

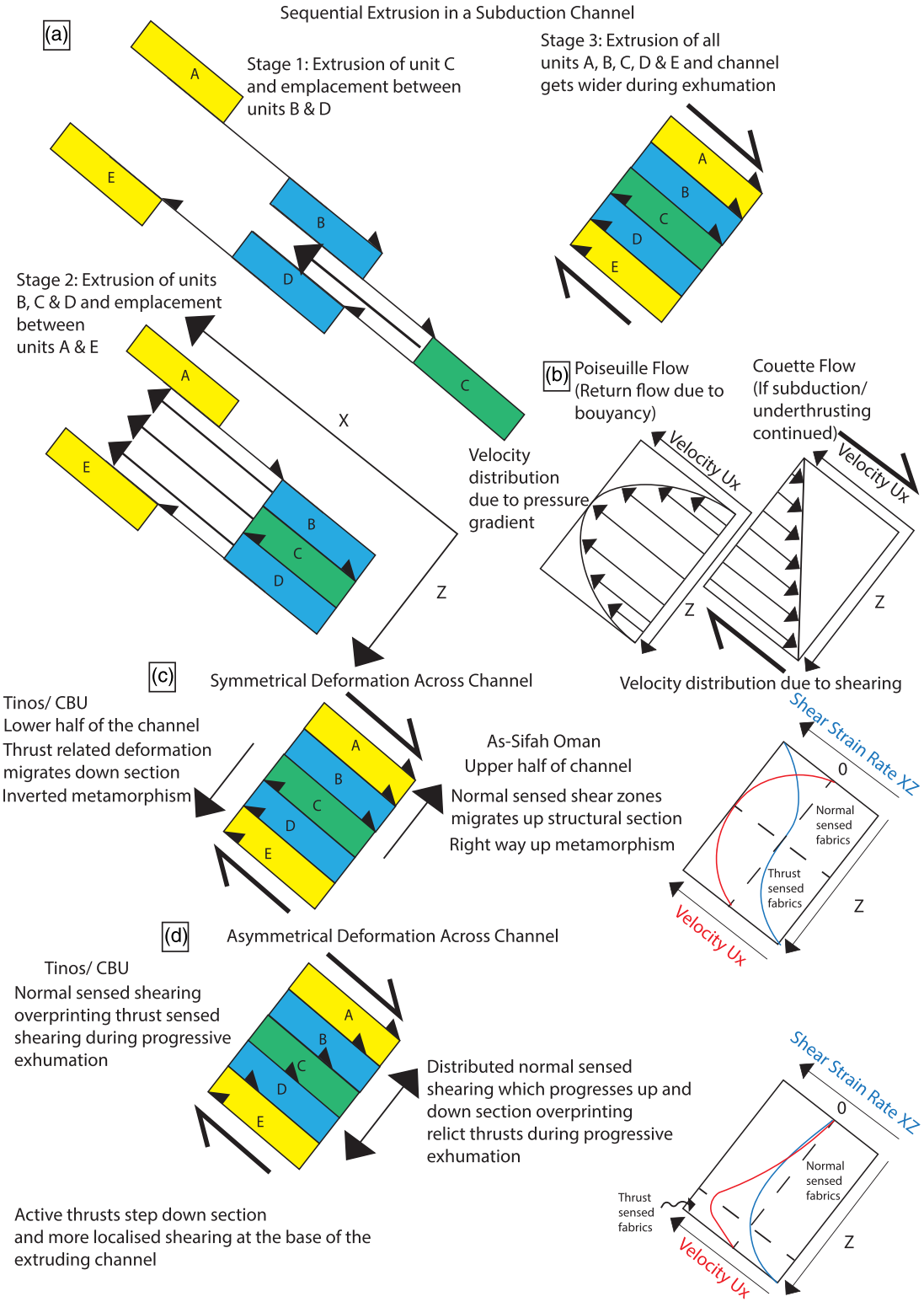

Figure 19. Extrusion channel flow model after England and Holland (1979) and Chemenda et al. (1995) for Tinos and As-Sifah in Oman showing the sequence of exhumation for various parts of the subduction channel. (a) Sequential extrusion where Package C is extruded adjacent to Packages B and D. At this point the packages become coupled and are extruded adjacent to Packages A and E, note thrusts at the base of the extruding package and normal-sensed faults at the top. (b) Schematic velocity distribution diagrams for Poiseuille and Couette flow. (c) Predicted strain and fabrics recorded from symmetrical extrusion within the channel and (d) asymmetrical extrusion within the channel with more localized thrusting deformation at the base of the channel and more pervasive normal-sensed shearing throughout the channel.

Because Molnar and England (1990) demonstrated that most cooling occurs in the first few Myr following subduction initiation, this cooling rate represents an absolute minimum.

A final consideration to explain low temperatures within the CBU is whether the *HP-LT* rocks remained within the interior of the subducting slab or channel and therefore had a conductive boundary layer separating them from the hotter slab surface. This mechanism may preserve cooler temperatures within the slab interior (e.g., England, 2018), whereas higher temperatures would occur on the slab-mantle wedge interface or on major shear zones due to both shear heating and conduction from the overlying mantle wedge (England, 2018). Following these arguments, the first-order control on the cool geotherm was likely the cold and old subducting lithosphere as well as the old and cold upper plate (ca. 190 Ma subducted oceanic lithosphere and the ca. 162 Ma Tsiknias Ophiolite in the upper plate), although fast subduction may have played an important role with cooling, it would also increase the magnitude of shear heating, which may become locally important.

5.3. Comparisons to High-Pressure Rocks Under Obducted Ophiolites

The best known examples of *HP* rocks structurally below ophiolite complexes include Western Turkey (Okay, 1982, 2002; Okay et al., 1998; Okay & Kelley, 1994; Plunder et al., 2013, 2015, 2016), New Caledonia (Cluzel et al., 2012; Gautier et al., 2016), and the As-Sifah eclogites and blueschists in Oman (Searle et al., 2004; Searle & Cox, 2002; Warren & Waters, 2006). In Western Turkey, a blueschist facies overprint of the metamorphic sole formed coeval with the overriding ophiolite at circa 93 Ma, indicating that the cooling may have occurred while the sole itself was exhuming (e.g., Plunder et al., 2016). However, Lu-Hf geochronology suggests an ~15 Myr age difference between high temperature sole metamorphism associated with subduction initiation and blueschist facies conditions with ages of circa 104 Ma and 93–86 Ma, respectively (Pourteau et al., 2019).

In Oman, eclogites and blueschists crop out at the deepest exposed levels of the Arabian continental margin, ~6–7 km structurally beneath the Semail Ophiolite and metamorphic sole (Searle & Cox, 1999, 2002; Searle et al., 1994, 2004; Warren et al., 2003). Eclogite in As-Sifah occur as boudins that represented basaltic sills that intruded the Arabian shelf carbonates (Searle et al., 2004) similar to eclogite within the Kionnia Subunit. These *HP* rocks reached similar *P-T* conditions to the CBU (20–22 kbar, 530–570°C) at circa 78 Ma (Warren et al., 2003; Warren & Waters, 2006) as the Arabian continental margin attempted to subduct. As-Sifah eclogites are also associated with extensive top-to-ENE extensional shear fabrics that formed during extrusion of buoyant continental margin back up the subduction channel under a passive roof fault during the final stages of ophiolite obduction, similar to the process we propose for Tinos (Searle et al., 2004). However, in As-Sifah the highest-pressure rocks are located at the deepest levels (right-way up metamorphism) and each tectonometamorphic unit are separated by normal-sensed shear zones associated with large *P-T* jumps (Searle et al., 2004). As-Sifah therefore represents the upper half of the extruding subduction channel, whereas the CBU on Tinos likely represents the lower half of the extruding channel/wedge and hence shows inverted metamorphism associated with firstly thrusting and underplating, overprinted by normal-sensed shearing during exhumation (Figure 19). The subduction-extrusion event also occurred some circa 15 Myr following subduction initiation and obduction of the Semail Ophiolite (Searle et al., 2004; Warren et al., 2003). The timing, occurrence and *P-T-D* constraints of *HP* metamorphism following ophiolite obduction in Oman are almost identical to that recorded in the Cyclades. The only difference is the *HP* sequence is cut by the later TSZ, which juxtaposes the Tsiknias Ophiolite and Metamorphic Sole directly against the CBU, which was subducted some ~25 Myr later.

6. Tectonic Model and Conclusions

Integration of *P-T-D* data with existing geochronology, the tectonothermal evolution of the CBU on Tinos, involves the following stages (Figure 20):

1. Initiation of a NE dipping subduction zone at circa 74 Ma, and southwest obduction of the circa 162 Ma Tsiknias Ophiolite, coeval with the formation of the metamorphic sole (ca. 74 Ma; Lamont, Roberts, et al., 2020). Pelagic metasediments and basalts of the metamorphic sole were subducted to shallow depths (~8.5 kbar) and experienced high-grade metamorphism and partial melting directly under the Tsiknias Thrust due to conductive heating combined with shear heating on the Tsiknias Thrust

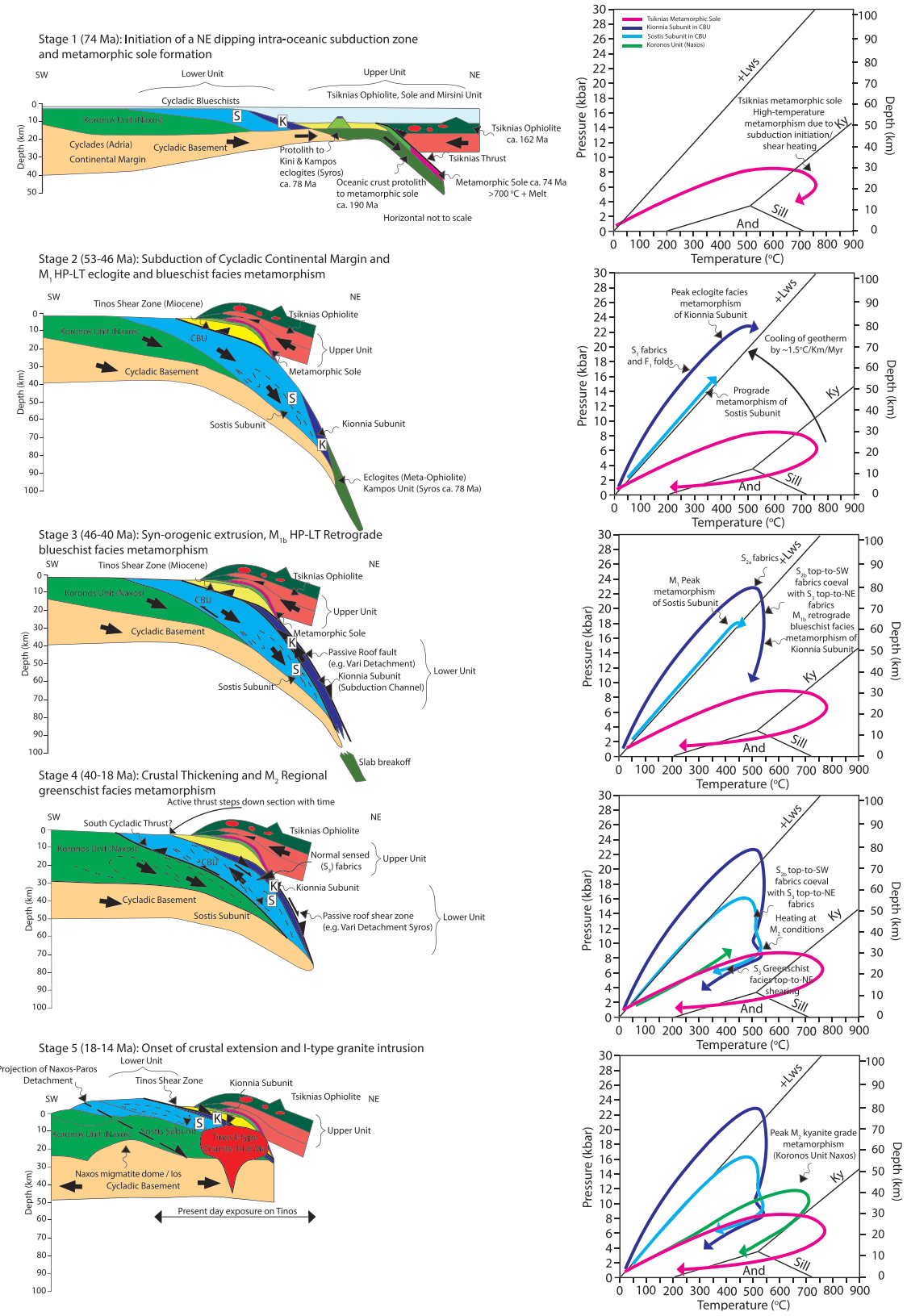

Figure 20. Tectonic model for the evolution of the CBU on Tinos and Tsiknias Ophiolite with annotations and companion summary *P-T* diagrams to illustrate the metamorphic conditions each unit experienced at each tectonic stage, K = Kionnia Subunit, S = Sostis Subunit, see text for discussion of the tectonics during each stage.

(Lamont, Roberts, et al., 2020). These rocks were accreted to the base of the ophiolite and became part of the upper plate during the obduction process and are today exposed in the Upper Unit that did not reach *HP* (M_1). During obduction, the subduction interface must have stepped back, allowing steady-state subduction of oceanic lithosphere under the Upper Unit (in the upper plate) for ~25 Myr. Late Cretaceous *UHP* metamorphic rocks also occur along strike in the Rhodope Massif (Collings et al., 2016) suggesting the subduction zone was a regional feature.

2. Steady-state NE dipping subduction of circa 190 Ma oceanic lithosphere continued between 74 and 53–46 Ma (i.e., for ca. 25 Myr). During this period, the subduction zone cooled, possibly owing to fast plate motions and advection of cold 190 Ma oceanic crust down to mantle depths. We believe Tinos eclogite represent boudinaged mafic intrusions and meta-volcanics within the leading edge of the Cycladic continental margin. Although eclogite in the Kampos and Kini mélanges on Syros, probably represent fragments of subducted oceanic crust and include metagabbro, serpentinites, plagiogranites, and metacherts (Keiter et al., 2004, 2011). On Tinos, U-Pb data suggest the M_1 event occurred at circa 57–53 Ma (Bulle et al., 2010) and possibly as old as circa 63–61 Ma (Bröcker & Enders, 1999) although the latter is likely a mixed age. This contrasts with slightly younger Lu-Hf garnet ages across the CBU of circa 52–46 Ma suggesting that the M_1 event was diachronous.
3. The arrival of the leading edge of the Cycladic continental margin at the trench resulted in burial of the CBU under a cold geothermal gradient (6–7°C/km) through the lawsonite stability field to peak (M_1) blueschist-eclogite facies conditions at circa 53–46 Ma (Lu-Hf garnet; Dragovic et al., 2012; Lagos et al., 2007). This burial process produced (S_{2b}) top-to-SW thrusts and isoclinal (F_1) folding as rocks were continuously underplated, causing the subduction wedge to thicken. Blueschist and eclogite exposed on the Kionnia peninsular achieved *P-T* conditions of ~22–26 kbar, 490–520°C and 20–23 kbar, 500–570°C, which equates to depths of ~70–80 km. Such depths can only be achieved due to the slab-pull force from already subducted and eclogitized dense oceanic crust at greater depths (e.g., Kampos Subunit on Syros; e.g., Keiter et al., 2004, 2011; Laurent et al., 2018).
4. Upon reaching peak pressures, and possibly due to a change in the boundary conditions from subduction termination as a result of continent-continent collision between Cyclades/Adria and Eurasia. The Kionnia and Pyrgos Subunits detached from the subducting slab and were buoyantly extruded back up an overriding channel (plate interface; Agard et al., 2018) producing top-to-NE (S_3) extensional fabrics along the roof shear zones, and top-to-SW fabrics (S_{2b}) along the base, and (F_2) sheath folds due to non-coaxial SW directed ductile flow. During exhumation, (M_{1b}) deformation was localized at the margins of the subunits. Eclogite remained unaffected by the exhumation related deformation (S_3), due to strain localization at the margins of the boudins, owing to the competency difference with the host metasediments. Lawsonite breakdown during decompression, released fluid, hydrating the matrix of these rocks at ~18–20 kbar and 550°C, producing crosscutting coarse and zoned epidotes and glaucophane-barroisite. Upright open folds (F_3) with their fold axes parallel to L_1 developed during the early stages of exhumation (M_{1b}), within the extruding channel due to lateral constriction conserving flow, likely owing to the channel having a variable along-strike thickness. Localized constriction occurred in the narrowest parts of the channel due to converging ductile flow in response to the obstruction at the margins.
5. Following peak M_1 pressures, the Kionnia Subunit was overthrusted onto the Sostis Subunit, by a top-to-SW thrust (Kionnia Thrust). The timing of this thrusting event (M_{1b}) is best constrained by Ar-Ar geochronology from phengite deformed with the foliation which yield ages of circa 44–40 Ma (Bröcker et al., 1993). The opposing kinematics on the top and bottom of the Kionnia Subunit and the lower pressures of the Sostis Subunit imply an extrusion mechanism, whereby the Sostis Subunit achieved its peak pressures at a slightly later time than the overlying Kionnia Subunit (which was on its return journey toward the surface). The Sostis Subunit experienced a similar prograde evolution, through the lawsonite stability field to less extreme *P-T* conditions of ~18.5 kbar and 490–500°C, followed by isothermal decompression associated with widening of the extrusion channel at shallower depths. Top-to-NE shearing (S_3) from M_1 blueschist-M_2 greenschist facies conditions was coeval with localized (S_{2b}) top-to-SW thrusting, suggesting the zone of underplating and subsequent extrusion stepped down structural level with time. The Sostis Thrust is the best exposure of a thrust that developed during this extrusion stage. The sequential juxtaposition of material during extrusion postdating peak metamorphism was when the architecture of the CBU on Tinos was aggregated. Exhumation from the subduction zone was complete by circa 31 Ma (Bulle et al., 2010), implying a minimum exhumation rate of ~4 km/Myr.

6. Upon reaching crustal depths (<12 kbar) the rocks were affected by extensive greenschist facies metamorphism (M_2), at *P-T* conditions of ~7.3 kbar and 530°C at circa 31–21 Ma (Bröcker et al., 1993, 2004; Bröcker & Franz, 1998; Hinsken et al., 2016). Top-to-NE (S_3) shearing became localized on the TSZ, which was responsible for juxtaposing the Lower Unit against the ophiolitic Upper Unit that was already at a much higher structural level. Across the TSZ, ~25 Myr of subduction history is missing. The TSZ truncates all M_1-M_{1b} fabrics and folds and therefore postdates synorogenic extrusion of *HP* rocks from subduction depths.
7. During M_2, upright crenulation cleavages (S_4) and open upright folds (F_4) formed across all subunits on Tinos with NE-SW axes parallel to the extensional (L_2) lineation. A component of E-W shortening must have occurred during the Miocene, prior to final exhumation.
8. All structures on Tinos are affected by doming and cut by the I-type granite pluton and smaller S-type intrusions, suggesting M_2 top-to-NE shearing ceased by circa 14.6 Ma (Brichau et al., 2007; Lamont, 2018). The final exhumation to the surface was due to footwall uplift associated with high angle brittle normal faults along the northern and southern coastlines.

Further geochronological investigation to constrain the rates of deformation and exhumation of the shear zones and subunits identified in this study are required to successfully correlate them across other Aegean islands. Such work would greatly improve understanding of deep accretionary processes that occurred during, or immediately prior to continent-continent collision between Cyclades/Adria and Eurasia resulting in the Aegean Orogeny.

Data Availability Statement

Data used in this study are deposited in the Oxford University Research Archive under the search name "The Cycladic Blueschist Unit on Tinos, Greece: Cold NE Subduction and SW Directed Extrusion of the Cycladic Continental Margin under the Tsiknias Ophiolite," (Lamont, Palin, 2020) available via https://10.5287/bodleian:rbaYPaMy7.

Acknowledgments

This work forms part of T. N. Lamont's doctoral project, which is funded by the Natural Environment Research Council (Grant NE/L0021612/1) and the University of Oxford for covering publication fees. We would like to thank University College Oxford for travel grants to undertake fieldwork, and Philip England, Chris Ballhaus, Lars Hansen for critical and thought-provoking discussion and analytical assistance. Anna Bidgood, Owen Weller, Marc St-Onge, and Richard White are thanked for assistance and discussion in the field. We thank the Editor Laurent Jolivet for handling the manuscript and Associate Editor Federico Rossetti for a thorough, very helpful, and critical review. We are greatly indebted to Michael Bröcker, Alexis Plunder, and an anonymous reviewer for critical and helpful reviews, comments, and suggested improvements that significantly refocused and improved the quality of the manuscript.

References

Abers, G. A. (2005). Seismic low-velocity layer at the top of subducting slabs: Observations, predictions, and systematics. *Physics of Earth and Planetary Interiors*, *149*, 7–29.

Abers, G. A., Van Keken, P. E., & Hacker, B. R. (2017). The cold and relatively dry nature of mantle forearcs in subduction zones. *Nature Geoscience*, *40*, 1–5.

Agard, P., Plunder, A., Angiboust, S., Bonnet, G., & Ruh, J. (2018). The subduction plate interface: Rock record and mechanical coupling (from long to short timescales). *Lithos*, *320–321*, 537–566.

Agard, P., Yamato, P., Jolivet, L., & Burov, E. (2009). Exhumation of oceanic blueschists and eclogites in subduction zones: Timing and mechanisms. *Earth-Science Reviews*, *92*(1–2), 53–79.

Alsop, G. I., & Holdsworth, R. E. (2006). Sheath folds as discriminators of bulk strain type. *Journal of Structural Geology*, *28*, 1588–1606.

Alsop, G. I., Holdsworth, R. E., & McCaffrey, K. J. W. (2007). Scale invariant sheath folds in salt, sediments and shear zones. *Journal of Structural Geology*, *29*(10), 1585–1604.

Altherr, R., Kreuzer, H., Wendt, I., Lenz, H., Wagner, G. A., Keller, J., et al. (1982). A late Oligocene/early Miocene high temperature belt in the Attic-Cycladic Crystalline Complex (SE Pelagonian, Greece). *Geolog*, *E23*, 97–164.

Andriessen, P. A. M., Boelrijk, N. A. I. M., Hebeda, H. E., Priem, H. N. A., Verdurmen, H. E. A. T., & Verschure, R. H. (1979). Dating the events of metamorphism and granitic magmatism in the Alpine Orogen of Naxos (Cyclades, Greece). *Contributions to Mineral Petrology*, *69*, 215–225.

Ashley, K. T., Caddick, M. J., Steele-MacInnis, M. J., Bodnar, R. J., & Dragovic, B. (2014). Geothermobarometric history of subduction recorded by quartz inclusions in garnet. *Geochemistry, Geophysics, Geosystems*, *15*, 350–360. https://doi.org/10.1002/2013GC005106

Avigad, D. (1998). High-pressure metamorphism and cooling on SE Naxos (Cyclades, Greece). *European Journal of Mineralogy*, *10*(6), 1309–1319.

Avigad, D., & Garfunkel, Z. (1989). Low-angle faults above and below a blueschist belt—Tinos Island, Cyclades, Greece. *Terra Nova*, *1*, 182–187.

Avigad, D., & Garfunkel, Z. (1991). Uplift and exhumation of high-pressure metamorphic terrains: The example of the Cycladic blueschist belt (Aegean Sea). *Tectonophysics*, *188*, 357–372.

Baziotis, I., Mposkos, E., Windley, B. F., & Lamont, T. N. (2020). Exhumation of Attica high-pressure rocks in a subduction channel: New metamorphic PT constraints from Attica, NW Cyclades, Greece. *Lithos*.

Behr, W., Kotowski, A., & Ashley, K. (2018). Dehydration-induced rheological heterogeneity and the deep tremor source in warm subduction zones. *Geology*, *46*.

Bolhar, R., Ring, U., & Ireland, T. R. (2017). Zircon in amphibolites from Naxos, Aegean Sea, Greece: Origin, significance and tectonic setting. *Journal of Metamorphic Geology*, *35*, 413–434.

Boyd, F. R., & England, J. L. (1960). The quartz-coesite transition. *Journal of Geophysical Research*, *65*(2), 749–756.

Brichau, S., Ring, U., Carter, A., Monie, P., Bolhar, R., Stockli, D., & Brunel, M. (2007). Extensional faulting on Tinos Island, Aegean Sea, Greece: How many detachments? *Tectonics*, *26*, TC4009. https://doi.org/10.1029/2006tc001969

Brichau, S., Ring, U., Ketcham, R. A., & Carter, A. (2006). Constraining the long-term evolution of the slip rate for a major extensional fault system in the central Aegean, Greece, using thermochronology. *Earth and Planetary Science Letters*, *241*, 293–306.
Bröcker, M. (1990). Die Blauschiefer–Grünschiefer-Assoziation der Insel Tinos (Kykladen, Griechenland) und ihre kontaktme- tamorphe Überprägung. *Geotektonische Forschungen*, *74*, 1–107.
Bröcker, M., Bieling, D., Hacker, B., & Gans, P. (2004). High-Si phengite records the time of greenschist facies overprinting: Implications for models suggesting mega-detachments in the Aegean Sea. *Journal of Metamorphic Geology*, *22*(5), 427–442.
Bröcker, M., & Enders, M. (1999). U–Pb zircon geochronology of unusual eclogite-facies rocks from Syros and Tinos (Cyclades, Greece). *Geological Magazine*, *136*, 111–118.
Bröcker, M., & Franz, L. (1994). The contact aureole on Tinos (Cyclades, Greece). Part I: Field relationships, petrography and *P-T* conditions. *Chemie der Erde*, *54*, 262–280.
Bröcker, M., & Franz, L. (1998). Rb–Sr isotope studies on Tinos Island (Cyclades, Greece): Additional time constraints for metamorphism, extent of infiltration-controlled overprinting and deformational activity. *Geological Magazine*, *135*, 369–382.
Bröcker, M., & Franz, L. (2000). The contact aureole on Tinos (Cyclades, Greece): tourmaline-biotite geothermometry and Rb-Sr geochronology. *Mineralogy and Petrology*, *70*(3–4), 257–283.
Bröcker, M., & Franz, L. (2005). The base of the Cycladic blueschist unit on Tinos Island (Greece) re-visited: Field relationships, phengite chemistry and Rb–Sr geochronology. *Journal of Mineralogy and Geochemistry*, *181*, 81–93.
Bröcker, M., & Keasling, A. (2006). Ionprobe U-Pb zircon ages from the high-pressure/low-temperature mélange of Syros, Greece: Age diversity and the importance of pre-Eocene subduction. *Journal of Metamorphic Geology*, *24*, 615–631. https://doi.org/10.1111/j.1525-1314.2006.00658.x
Bröcker, M., Kreuzer, A., Matthews, A., & Okrusch, M. (1993). $^{40}Ar/^{39}Ar$ and oxygen isotope studies of poly-metamorphism from Tinos Island, Cycladic blueschist belt, Greece. *Journal of Metamorphic Geology*, *11*, 223–240.
Bröcker, M., Löwen, K., & Rodionov, N. (2014). Unraveling protolith ages of meta-gabbros from Samos and the Attic–Cycladic Crystalline Belt, Greece: Results of a U–Pb zircon and Sr–Nd whole rock study. *Lithos*, *198–234*,199, 248.
Brovarone, A. V., Beyssac, O., Malavieille, J., Molli, G., Beltrando, M., & Compagnoni, R. (2013). Stacking and metamorphism of continuous segments of subducted lithosphere in a high-pressure wedge: The example of Alpine Corsica (France). *Earth-Science Reviews*, *116*, 35–56.
Brovarone, A. V., & Herwartz, D. (2013). Timing of HP metamorphism in the Schistes Lustrés of Alpine Corsica: New Lu–Hf garnet and lawsonite ages. *Lithos*, *172*, 175–191.
Brovarone, A. V., Groppo, C., Hetényi, G., Compagnoni, R., & And Malavieille, J. (2011). Coexistence of lawsonite-bearing eclogite and blueschist: Phase equilibria modelling of Alpine Corsica metabasalts and petrological evolution of subducting slabs. *Journal of Metamorphic Geology*, *29*, 583–600.
Bulle, F., Bröcker, M., Gärtner, C., & Keasling, A. (2010). Geochemistry and geochronology of HP mélanges from Tinos and Andros, Cycladic blueschist belt, Greece. *Lithos*, *117*(1–4), 61–81.
Chemenda, A. I., Mattauer, M., Malavieille, J., & Bokun, A. N. (1995). A mechanism for syncollision rock exhumation and associated normal faulting: Results from physical modelling. *Earth and Planetary Science Letters*, *132*, 225–232.
Cluzel, D., Jourdan, F., Meffre, S., Maurizot, P., & Lesimple, S. (2012). The metamorphic sole of New Caledonia ophiolite: 40Ar/39Ar, U-Pb, and geochemical evidence for subduction inception at a spreading ridge. *Tectonics*, *31*, TC3016. https://doi.org/10.1029/2011TC003085
Collings, D., Savov, I., Maneiro, K., Baxter, E., Harvey, J., & Dimitrov, I. (2016). Late Cretaceous UHP metamorphism recorded in kyanite–garnet schists from the Central Rhodope Mountains, Bulgaria. *Lithos*, *246–247*, 165–181.
Cowan, R. J., Searle, M. P., & Waters, D. J. (2014). Structure of the metamorphic sole to the Oman ophiolite, Sumeini window and Wadi Tayyin: Implications for ophiolite obduction processes. *Geological Society, London, Special Publications*, *392*(1), 155–175.
Davis, P. B. (2011). Petrotectonics of lawsonite eclogite exhumation: Insights from the Sivrihisar massif Turkey. *Tectonics*, *30*, TC1006. https://doi.org/10.1029/2010TC002713
Davis, P. B., & Whitney, D. L. (2006). Petrogenesis of lawsonite and epidote eclogite and blueschist, Sivrihisar Massif, Turkey. *Journal of Metamorphic Geology*, *24*, 823–849.
DeMets, C., Iaffaldano, G., & Merkouriev, S. (2015). High-resolution Neogene and Quaternary estimates of Nubia-Eurasia-North America Plate motion. *Geophysical Journal International*, *203*, 416–427.
Dragovic, B., Baxter, E. F., & Caddick, M. J. (2015). Pulsed dehydration and garnet growth during subduction revealed by zoned garnet geochronology and thermodynamic modeling, Sifnos, Greece. *Earth and Planetary Science Letters*, *413*, 111–122.
Dragovic, B., Samanta, L. M., Baxter, E. F., & Selverstone, J. (2012). Using garnet to constrain the duration and rate of water-releasing metamorphic reactions during subduction: An example from Sifnos, Greece. *Chemical Geology*, *314*, 9–22.
Durr, S., Altherr, R., Okrusch, M., & Seidel, E. (1978). The median Aegean Belt; stratigraphy, structure, metamorphism. In H. Closs, D. Roeder, & K. Schmidt (Eds.), *Alps, Apennines, Hellenides*. Stuttgart: Springer.
England, P. (2018). On shear stresses, temperatures, and the maximum magnitudes of earthquakes at convergent plate boundaries. *Journal of Geophysical Research: Solid Earth*, *123*, 7165–7202. https://doi.org/10.1029/2018JB015907
England, P., & Molnar, P. (1993). The interpretation of inverted metamorphic isograds using simple physical calculations. *Tectonics*, *12*, 145–157.
England, P., & Wilkins, C. (2004). A simple analytical approximation to the temperature structure in subduction zones. *Geophysical Journal International*, *159*, 1138–1154.
England, P. C., & Holland, T. J. B. (1979). Archimedes and the Tauern eclogites: The role of buoyancy in the preservation of exotic eclogite blocks. *Earth and Planetary Science Letters*, *44*, 287–294.
Fryer, P., Wheat, C. G., & Mottl, M. J. (1999). Mariana blueschist mud volcanism: Implications for conditions within the subduction zone. *Geology*, *27*(2), 103–106.
Gautier, P., Quesnel, B., Boulvais, P., & Cathelineau, M. (2016). The emplacement of the Peridotite Nappe of New Caledonia and its bearing on the tectonics of obduction. *Tectonics*, *35*, 3070–3094. https://doi.org/10.1002/2016TC004318
Gerogiannis, N., Xypolias, P., Chatzaras, V., Aravadinou, E., & Papapavlou, K. (2019). Deformation within the Cycladic subduction–exhumation channel: New insights from the enigmatic Makrotantalo nappe (Andros, Aegean). *International Journal of Earth Sciences (Geol Rundsch) (2019)*, *108*, 817–843.
Gerya, T. V., Stöckhert, B., & Perchuk, A. L. (2002). Exhumation of high-pressure metamorphic rocks in a subduction channel: A numerical simulation. *Tectonics*, *21*(6), 1056. https://doi.org/10.1029/2002TC001406
Goffé, B., & Chopin, C. (1986). High-pressure metamorphism in the Western Alps: Zoneography of metapelites, chronology and consequences. *Schweiz. mineral. petrogr Mitt.*, *66*, 41–52.

Groppo, C., Forster, M., Lister, G., & Compagnoni, R. (2009). Glaucophane schists and associated rocks from Sifnos (Cyclades, Greece): New constraints on the P-T evolution from oxidized systems. *Lithos*, *109*, 254–273.
Guilmette, C., Smit, M. A., van Hinsbergen, D. J., Gürer, D., Corfu, F., Charette, B., et al. (2018). Forced subduction initiation recorded in the sole and crust of the Semail Ophiolite of Oman. *Nature Geoscience*, *11*(9), 688.
Hacker, B. R. (1990). Simulation of the metamorphic and deformational history of the metamorphic sole of the Oman ophiolite. *Journal of Geophysical Research*, *95*, 4895–4907.
Hacker, B. R., & Gerya, T. V. (2013). Paradigms, new and old, for ultrahigh-pressure tectonism. *Tectonophysics*, *603*, 79–88.
Hacker, B. R., Gerya, T. V., & Gilotti, J. A. (2013). Formation and exhumation of ultrahigh-pressure terranes. *Elements*, *9*, 289–293.
Henry, D. J., Guidotti, C. V., & Thomson, J. A. (2005). The Ti-saturation surface for low-to-medium pressure metapelitic biotite: Implications for Geothermometry and Ti-substitution mechanisms. *American Mineralogist*, *90*, 316–328.
Hilairet, N., & Reynard, B. (2008). Stability and dynamics of serpentinite layer in subduction zone. *Tectonophysics*. https://doi.org/10.1016/j.tecto.2008.10.005
Hinsken, T., Bröcker, M., Berndt, J., & Gärtner, C. (2016). Maximum sedimentation ages and provenance of metasedimentary rocks from Tinos Island, Cycladic blueschist belt, Greece. *International Journal of Earth Sciences*, *105*(7), 1923–1940.
Hinsken, T., Bröcker, M., Strauss, H., & Bulle, F. (2017). Geochemical, isotopic and geochronological characterization of listvenite from the Upper Unit on Tinos, Cyclades, Greece. *Lithos*, *282*, 281–297.
Holland, T. J. B., & Blundy, J. (1994). Non-ideal interactions in calcic amphiboles and their bearing on amphibole-plagioclase thermometry. *Contributions to Mineralogy and Petrology*, *116*, 433–447.
Huet, B., Labrousse, L., & Jolivet, L. (2009). Thrust or detachment? Exhumation processes in the Aegean: Insight from a field study on Ios (Cyclades, Greece). *Tectonics*, *28*, TC3007. https://doi.org/10.1029/2008TC002397
Huet, B., Labrousse, L., Monie, P., Malvoisin, B., & Jolivet, L. (2015). Coupled phengite ^{40}Ar–^{39}Ar geochronology and thermo-barometry: P-T-t evolution of Andros Island (Cyclades, Greece). *Geological Magazine*, *152*, 711–727.
Hunziker, D., Burg, J.-P., Moulas, E., Reusser, E., & Omrani, J. (2017). Formation and preservation of fresh lawsonite: Geothermobarometry of the North Makran Blueschists, southeast Iran. *Journal of Metamorphic Geology*, *35*, 871–895.
Jolivet, L., & Brun, J. P. (2010). Cenozoic geodynamic evolution of the Aegean region. *International Journal of Earth Sciences*, *99*, 109–138.
Jolivet, L., Faccenna, C., Huet, B., Labrousse, L., Le Pourhiet, L., Lacombe, O., Lecomte, E., et al. (2013). Aegean tectonics: Strain localisation, slab tearing and trench retreat. *Tectonophysics*, *597–598*, 1–33.
Jolivet, L., Lecomte, E., Huet, B., Denèle, Y., Lacombe, O., Labrousse, L., et al. (2010). The north cycladic detachment system. *Earth and Planetary Science Letters*, *289*, 87–104.
Jolivet, L., Menant, A., Sternai, P., Rabillard, A., Arbaret, L., Augier, R., et al. (2015). The geological signature of a slab tear below the Aegean. *Tectonophysics*, *659*, 166–182. https://doi.org/10.1016/j.tecto.2015.08.004
Katzir, Y., Matthews, A., Garfunkel, Z., Schliestedt, M., & Avigad, D. (1996). The tectono-metamorphic evolution of a dismembered ophiolite (Tinos, Cyclades, Greece). *Geological Magazine*, *133*, 237–254.
Katzir, Y., Valley, J. W., Matthews, A., & Spicuzza, M. J. (2002). Tracking fluid flow during deep crustal anatexis: Metasomatism of peridotites (Naxos, Greece). *Contributions to Mineralogy and Petrology*, *142*(6), 700–713.
Keay, S., Lister, G., & Buick, I. (2001). The timing of partial melting, Barrovian metamorphism and granite intrusion in the Naxos metamorphic core complex, Cyclades, Aegean Sea, Greece. *Tectonophysics*, *342*, 275–312.
Keiter, M., Ballhaus, C., & Tomaschek, F. (2011). A new geological map of the Island of Syros (Aegean Sea, Greece): Implications for lithostratigraphy and structural history of the Cycladic Blueschist Unit. *Geological Society of America Special Papers*, *481*, 1–43.
Keiter, M., Piepjohn, K., Ballhaus, C., Lagos, M., & Bode, M. (2004). Structural development of high-pressure metamorphic rocks on Syros island (Cyclades, Greece). *Journal of Structural Geology*, *26*, 1433–1445.
Kincaid, C., & Sacks, I. S. (1997). Thermal and dynamical evolution of the upper mantle in subduction zones. *Journal of Geophysical Research*, *102*(B6), 12,295–12,315.
Kohn, M. J., Castro, A. E., Kerswell, B. C., Ranero, C. R., & Spear, F. S. (2018). Shear heating reconciles thermal models with the metamorphic rock record of subduction. *Proceedings of the National Academy of Sciences*, *115*(46), 11,706–11,711.
Krogh Ravna, E. J. (2000). The garnet–clinopyroxene Fe^{2+}–Mg geothermometer: An updated calibration. *Journal of Metamorphic Geology*, *18*(2), 211–219.
Lagos, M., Scherer, E. E., Tomaschek, F., Münker, C., Keiter, M., Berndt, J., & Ballhaus, C. (2007). High precision Lu–Hf geochronology of Eocene eclogite-facies rocks from Syros, Cyclades, Greece. *Chemical Geology*, *243*(1-2), 16–35. https://doi.org/10.1016/j.chemgeo.2007.04.008
Lamont, T. N. (2018). Unravelling the structural, metamorphic, and strain history of the "Aegean orogeny," southern Greece, with a combined structural, petrological and geochronological approach, D. Phil Thesis, University of Oxford
Lamont, T. N., Palin, R. M., Searle, M. P., Gopon, P., Roberts, N. M. W., Wade, J., & Waters, D. J. (2020). *Supporting data for the Cycladic Blueschist Unit on Tinos, Greece: Cold NE subduction and SW-directed extrusion of the cycladic continental margin under the Tsiknias Ophiolite*. University of Oxford.
Lamont, T. N., Roberts, N. M., Searle, M. P., Gopon, P., Waters, D. J., & Millar, I. (2020). The age, origin and emplacement of the Tsiknias ophiolite, Tinos, Greece. *Tectonics*, *39*, e2019TC005677. https://doi.org/10.1029/2019TC005677
Lamont, T. N., Searle, M. P., Waters, D. J., Roberts, N. M., Palin, R. M., Smye, A., et al. (2019). Compressional origin of the Naxos metamorphic core complex, Greece: Structure, petrography, and thermobarometry. *Geological Society of America Bulletin*, *132*(1–2), 149–197.
Laurent, V., Jolivet, L., Roche, V., Augier, R., Scaillet, S. & Cardello, G. L. et al. (2016). Strain localization in a fossilized subduction channel: Insights from the Cycladic Blueschist Unit (Syros, Greece). *Tectonophysics*, *672–673*, 150–169.
Laurent, V., Lanari, P., Naïr, I., Augier, R., Lahfid, A., & Jolivet, L. (2018). Exhumation of eclogite and blueschist (Cyclades, Greece): Pressure–temperature evolution determined by thermobarometry and garnet equilibrium modelling. *Journal of Metamorphic Geology*, *36*, 769–798.
Lévy, F., & Jaupart, C. (2011). Folding in regions of extension. *Geophysical Journal International*, *185*, 1120–1134.
Lister, G. S., Banga, G., & Feenstra, A. (1984). Metamorphic core complexes of cordilleran type in the Cyclades, Aegean Sea, Greece. *Geology*, *12*, 221–225.
Lister, G. S., & Forster, M. A. (2016). White mica ^{40}Ar/^{39}Ar age spectra and the timing of multiple episodes of high-P metamorphic mineral growth in the Cycladic eclogite–blueschist belt, Syros, Aegean Sea, Greece. *Journal of Metamorphic Geology*, *34*, 401–421.
Maekawa, H., Shozui, M., Ishll, T., Fryer, P., & Pearce, J. (1993). Blueschist metamorphism in an active subduction zone. *Nature*, *364*, 520–523.

Mancktelow, N., & Pavlis, T. (1994). Fold-fault relationships in low-angle detachment systems. *Tectonics*, *13*(2), 668–685.
Martin, L., Duchêne, S., Deloule, E., & Vanderhaeghe, O. (2006). The isotopic composition of zircon and garnet: A record of the metamorphic history of Naxos, Greece. *Lithos*, *87*, 174–192.
Maruyama, S., & Liou, J. (1996). Blueschists and eclogites of the world and their exhumation. *International Geology ldots*, *38*, 485–594.
Matthews, A., Lieberman, J., Avigad, D., & Garfunkel, Z. (1999). Fluid-rock interaction and thermal evolution during thrusting of an Alpine metamorphic complex (Tinos Island, Greece). *Contributions to Mineralogy and Petrology*, *135*, 212–224.
Means, W. D. (1989). Stretching faults. *Geology*, *17*, 893–896.
Mehl, C., Jolivet, L., & Lacombe, O. (2005). From ductile to brittle: Evolution and localization of deformation below a crustal detachment (Tinos, Cyclades, Greece). *Tectonics*, *24*, TC4017. https://doi.org/10.1029/2004tc001767
Melidonis, N. G. (1980). The geological structure and mineral deposits of Tinos island (Cyclades, Greece). *Geology Greece*, *13*, 1–80.
Miyashiro, A. (1961). Evolution of metamorphic belts. *Journal of Petrology*, *2*(31), 277–311.
Molnar, P., & England, P. (1990). Temperatures, heat flux, and frictional stress near major thrust faults. *Journal of Geophysical Research*, *95*, 4833–4856.
Molnar, P., & England, P. (1995). Temperatures in zones of steady-state underthrusting of young oceanic lithosphere. *Earth and Planetary Science Letters*, *131*, 57–70.
Okay, A. I. (1982). Incipient Blueschist metamorphism and metasomatism in the Tavşanlı region, Northwest Turkey. *Contributions to Mineralogy and Petrology*, *79*, 361–367.
Okay, A. I. (1989). Alpine-Himalayan blueschists. *Annual Review of Earth and Planetary Sciences*, *17*(1), 55–87.
Okay, A. İ. (2002). Jadeite-chloritoid-glaucophane-lawsonite blueschists in north-west Turkey: Unusually high P/T ratios in continental crust. *Journal of Metamorphic Geology*, *20*, 757–768.
Okay, A. I., Harris, N. B. W., & Kelley, S. (1998). Exhumation of blueschists along a Tethyan suture in northwest Turkey. *Tectonophysics*, *285*, 275–299.
Okay, A. İ., & Kelley, S. (1994). Tectonic setting, petrology and geochronology of jadeite + glaucophane and chloritoid + glaucophane schists from north-west Turkey. *Journal of Metamorphic Geology*, *12*, 455–466.
Okrusch, M., & Bröcker, M. (1990). Eclogite facies rocks in the Cycladic blueschist belt, Greece: A review. *European Journal of Mineralogy*, *2*, 451–478.
Oxburgh, E. R., & Turcotte, D. L. (1971). Origin of paired metamorphic belts and crustal dilation in island arc regions. *Journal of Geophysical. Research*, *76*(5), 1315–1327.
Palin, R. M., Weller, O. M., Waters, D. J., & Dyck, B. (2016). Quantifying geological uncertainty in metamorphic phase equilibria modelling; a Monte Carlo assessment and implications for tectonic interpretations. *Geoscience Frontiers*, *7*, 591–607.
Palin, R. M., & White, R. W. (2016). Emergence of blueschists on Earth linked to secular changes in oceanic crust composition. *Nature Geoscience*, *9*(4), 60–64.
Papanikolaou, D. (2013). Tectonostratigraphic models of the Alpine terranes and subduction history of the Hellenides. *Tectonophysics*, *595–596*, 1–24.
Papeschi, S., Musumeci, G., Massonne, H. J., Mazzarini, F., Ryan, E. J., & Viola, G. (2020). High-P (P= 1.5–1.8 GPa) blueschist from Elba: Implications for underthrusting and exhumation of continental units in the Northern Apennines. *Journal of Metamorphic Geology*.
Parra, T., Vidal, O., & Jolivet, L. (2002). Relation between the intensity of deformation and retrogression in blueschist metapelites of Tinos Island (Greece) evidenced by chlorite–mica local equilibria. *Lithos*, *63*, 41–66.
Patzak, M., Okrusch, M., & Kreuzer, H. (1994). The Akrotiri unit on the island of Tinos, Cyclades, Greece: Witness to a lost terrane of Late Cretaceous age. *Neues Jahrbuch für Geologie und Paläontologie Abhandlungen*, *194*, 211–252.
Peacock, S. M. (1992). Blueschist-facies metamorphism, shear heating, and P-T-t paths in subduction shear zones. *Journal of Geophysical Research*, *97*(B12), 17,693–17,707.
Peillod, A., Ring, U., Glodny, J., & Skelton, A. (2017). An Eocene/Oligocene blueschist-/greenschist-facies P–T loop from the Cycladic blueschist unit on Naxos Island, Greece: Deformation-related reequilibration vs thermal relaxation. *Journal of Metamorphic Geology*, *35*, 805–830.
Philippon, M., Brun, J. P., & Gueydan, F. (2011). Tectonics of the Syros blueschists (Cyclades, Greece): From subduction to Aegean extension. *Tectonics*, *30*, TC4001. https://doi.org/10.1029/2010tc002810
Platt, J. P. (1986). Dynamics of orogenic wedges and the uplift of high-pressure metamorphic rocks. *Geological Society of America Bulletin*, *97*(9), 1037–1053.
Plunder, A., Agard, P., Chopin, C., & Okay, A. I. (2013). Geodynamics of the Tavşanlı zone, western Turkey: Insights into subduction/obduction processes. *Tectonophysics*, *608*, 884–903.
Plunder, A., Agard, P., Chopin, C., Pourteau, A., & Okay, A. I. (2015). Accretion, underplating and exhumation along a subduction interface: From subduction initiation to continental subduction (Tavşanlı zone, W. Turkey). *Lithos*, *226*, 233–254.
Plunder, A., Agard, P., Chopin, C., Soret, M., Okay, A. I., & Whitechurch, H. (2016). Metamorphic sole formation, emplacement and blueschist facies overprint: Early subduction dynamics witnessed by western Turkey ophiolites. *Terra Nova*, *28*(5), 329–339.
Pourteau, A., Scherer, E. E., Schorn, S., Bast, R., Schmidt, A., & Ebert, L. (2019). Thermal evolution of an ancient subduction interface revealed by Lu–Hf garnet geochronology, Halilbağı Complex (Anatolia). *Geoscience Frontiers*, *10*(1), 127–148.
Powell, R. (1985). Regression diagnostics and robust regression in geothermometer/geobarometer calibration; the garnet-clinopyroxene geothermometer revisited. *Journal of Metamorphic Geology*, *3*, 231–243.
Powell, R., & Holland, T. J. (2008). On thermobarometry. *Journal of Metamorphic Geology*, *26*, 155–179.
Putlitz, B., Cosca, M. A., & Schumacher, J. C. (2005). Prograde mica $^{40}Ar/^{39}Ar$ growth ages recorded in high pressure rocks (Syros, Cyclades, Greece). *Chemical Geology*, *214*, 79–98.
Ravna, E. J. K., Andersen, T. B., Jolivet, L., & De Capitani, C. (2010). Cold subduction and the formation of lawsonite eclogite—Constraints from prograde evolution of eclogitized pillow lava from Corsica. *Journal of Metamorphic Geology*, *28*, 381–395.
Ring, U., Glodny, J., Will, T., & Thomson, S. (2010). The Hellenic subduction system: High-pressure metamorphism, exhumation, normal faulting, and large-scale extension. *Annual Reviews of Earth and Planetary Science*, *38*, 45–76.
Ring, U., & Layer, P. W. (2003). High-pressure metamorphism in the Aegean, eastern Mediterranean: Underplating and exhumation from the Late Cretaceous until the Miocene to Recent above the retreating Hellenic subduction zone. *Tectonics*, *22*(3), 1022. https://doi.org/10.1029/2001TC001350
Ring, U., Pantazides, H., Glodny, J., & Skelton, A. (2020). Forced return flow deep in the subduction hannel, Syros, Greece. *Tectonics*, *39*, e2019TC005768. https://doi.org/10.1029/2019TC005768

Roche, V., Laurent, V., Cardello, G. L., Jolivet, L., & Scaillet, S. (2016). Anatomy of the Cycladic Blueschist Unit on Sifnos Island (Cyclades, Greece). *Journal of Geodynamics*, *97*, 62–87.
Schliestedt, M., Altherr, R., & Matthews, A. (1987). Evolution of the cycladic crystalline complex: Petrology, isotope geochemistry and geochronolgy.
Schmädicke, E., & Will, T. M. (2003). Pressure–temperature evolution of blueschist facies rocks from Sifnos, Greece, and implications for the exhumation of high-pressure rocks in the Central Aegean. *Journal of Metamorphic Geology*, *21*, 799–811.
Schumacher, J. C., Brady, J. B., Cheney, J. T., & Tonnsen, R. R. (2008). Glaucophane-bearing marbles on Syros, Greece. *Journal of Petrology*, *49*, 1667–1686.
Searle, M. P., & Cox, J. (1999). Tectonic setting, origin, and obduction of the Oman ophiolite. *Geological Society of America Bulletin*, *111*, 104–122.
Searle, M. P., & Cox, J. (2002). Subduction zone metamorphism during formation and emplacement of the Semail ophiolite in the Oman Mountains. *Geological Magazine*, 241–255.
Searle, M. P., & Lamont, T. N. (2019). Compressional metamorphic core complexes, low-angle normal faults and extensional fabrics in compressional tectonic settings. *Geological Magazine*, 1–18.
Searle, M. P., Warren, C. J., Waters, D. J., & Parrish, R. R. (2004). Structural evolution, metamorphism and restoration of the Arabian continental margin, Saih Hatat region, Oman Mountains. *Journal of Structural Geology*, *26*, 451–473.
Searle, M. P., Waters, D. J., Martin, H. N., & Rex, D. C. (1994). Structure and metamorphism of blueschist–eclogite facies rocks from the northeastern Oman Mountains. *Journal of the Geological Society*, *151*(3), 555–576.
Smye, A. J., Bickle, M. J., Holland, T. J., Parrish, R. R., & Condon, D. J. (2011). Rapid formation and exhumation of the youngest Alpine eclogites: A thermal conundrum to Barrovian metamorphism. *Earth and Planetary Science Letters*, *306*(3–4), 193–204.
Soukis, K., & Stockli, D. F. (2013). Structural and thermochronometric evidence for multi-stage exhumation of southern Syros, Cycladic islands, Greece. *Tectonophysics*, *595*, 148–164.
Stípská, P., & Powell, R. (2005). Can ternary feldspars be used to constrain the metamorphic conditions of high-grade meta-igneous rocks? Evidence from orthopyroxene gneisses, bohemian massif. *Geolines*, *19*, 110.
St-Onge, M. R., Rayner, N., Palin, R. M., Searle, M. P., & Waters, D. J. (2013). Integrated pressure–temperature–time constraints for the Tso Morari dome (Northwest India): Implications for the burial and exhumation path of UHP units in the western Himalaya. *Journal of Metamorphic Geology*, *3*, 469–504.
Syracuse, E. M., Keken, P. E. V., & Abers, G. A. (2010). The global range of subduction zone thermal models. *Physics of the Earth and Planetary Interiors*, *183*, 73–90.
Tomaschek, F., Kennedy, A. K., Villa, I. M., Lagos, M., & Ballhaus, C. (2003). Zircons from Syros, Cyclades, Greece—Recrystallization and mobilization of zircon during high-pressure metamorphism. *Journal of Petrology*, *44*, 1977–2002.
Trotet, F., Jolivet, L., & Vidal, O. (2001). Tectono-metamorphic evolution of Syros and Sifnos islands (Cyclades, Greece). *Tectonophysics*, *338*, 179–206.
Trotet, F., Vidal, O., & Jolivet, L. (2001). Exhumation of Syros and Sifnos metamorphic rocks (Cyclades, Greece). New constraints on the PT paths. *European Journal of Mineralogy*, *13*, 901–902.
Turcotte, D. L., & Schubert, G. (1973). Frictional heating of descending lithosphere. *Journal of Geophysical Research*, *78*, 5876–5886.
Virgo, S., von Hagke, C., & Urai, J. L. (2018). Multiphase boudinage: A case study of amphibolites in marble in the Naxos migmatite core. *Solid Earth*, *9*, 91–113.
Vissers, R. L. M., & Meijer, P. T. (2012). Iberian plate kinematics and Alpine collision in the Pyrenees. *Earth Science Reviews*, *114*, 61–83.
von Hagke, C., Bamberg, B., Virgo, S., & Urai, J. L. (2018). Outcrop-scale tomography: insights into the 3D structure of multiphase boudins. *Journal of Structural Geology*, *115*, 311–317.
Wang, Y., Prelević, D., & Foley, S. F. (2019). Geochemical characteristics of lawsonite blueschists in tectonic mélange from the Tavşanlı Zone, Turkey: Potential constraints on the origin of Mediterranean potassium-rich magmatism. *American Mineralogist*, *104*(5), 724–743.
Warren, C. J., Beaumont, C., & Jamieson, R. A. (2008). Modelling tectonic styles and ultra-high pressure (UHP) rock exhumation during the transition from oceanic subduction to continental collision. *Earth and Planetary Science Letters*, *267*, 129–145.
Warren, C. J., Parrish, R. R., Searle, M. P., & Waters, D. J. (2003). Dating the subduction of the Arabian continental margin beneath the Semail ophiolite, Oman. *Geology*, *31*(10), 889–892.
Warren, C. J., Parrish, R. R., Waters, D. J., & Searle, M. P. (2005). Dating the geologic history of Oman's Semail ophiolite: Insights from U-Pb geochronology. *Contributions to Mineralogy and Petrology*, *150*, 403.
Warren, C. J., & Waters, D. J. (2006). Oxidized eclogites and garnet-blueschists from Oman: P–T path modelling in the NCFMASHO system. *Journal of Metamorphic Geology*, *24*(9), 783–802.
Waters, D. J., & Martin, H. N. (1996). The garnet-Cpx-phengite barometer. Recommended Calibration and Calculation Method, 1.
Weller, O. M., Wallis, S. R., Aoya, M., & Nagaya, T. (2015). Phase equilibria modelling of blueschist and eclogite from the Sanbagawa metamorphic belt of southwest Japan reveals along-strike consistency in tectonothermal architecture. *Journal of Metamorphic. Geology*, *33*, 579–596.
Whitney, D. L., & Evans, B. W. (2010). Abbreviations for names of rock-forming minerals. *American Mineralogist*, *95*(1), 185–187.
Woodsworth, G. J. (1977). Homogenization of zoned garnets from pelitic schists. *Canadian Mineralogist*, *15*, 230–242.
Xypolias, P., & Alsop, G. I. (2014). Regional flow perturbation folding within an exhumation channel: A case study from the Cycladic Blueschists. *Journal of Structural Geology*, *62*, 141–155.
Zeffren, S., Avigad, D., Heimann, A., & Gvirtzman, Z. (2005). Age resetting of hanging wall rocks above a low-angle detachment fault: Tinos Island (Aegean Sea). *Tectonophysics*, *400*, 1–25.

References From the Supporting Information

Abbey, S. (1983). Studies in "Standard Samples" of silicate rocks minerals 1969–1982. *Geological Survey of Canada Paper*, *83–15*, 1–114.
Bhattacharya, L., Mohanty, L., Maji, A., Sen, S. K., & Raith, M. (1992). Non-ideal mixing in the phlogopite-annite binary: Constraints from experimental data on Mg-Fe partitioning and a reformulation of the biotite-garnet geothermometer. *Contributions to Mineral Petrology*, *111*, 87–98.
Carson, C. J., Powell, R., & Clarke, G. L. (1999). Calculated mineral equilibria for eclogites in $CaO–Na_2O–FeO–MgO–Al_2O_3–SiO_2–H_2O$: Application to the Pouebo Terrane, PamPeninsula, New Caledonia. *Journal of Metamorphic Geology*, *17*, 9–2.

Clarke, G. L., Powell, R., & Fitzherbert, J. A. (2006). The lawsonite paradox: A comparison of field evidence and mineral equilibria modelling. *Journal of Metamorphic Geology*, *24*, 715–725.

Droop, J. T. R. (1987). A general equation for estimating Fe^{3+} concentrations in ferromagnesian silicates and oxides from microprobe analyses, using stoichiometric criteria. *Mineralogical Magazine*, *51*, 431–435.

Essen, E. J., & Fyfe, W. S. (1967). Omphacite in Californian rocks. *Contributions to Mineral Petrology*, *15*, 1–23.

Ganguly, J. (1979). Garnet and clinopyroxene solid solutions, and geothermometry based on Fe-Mg distribution coefficient. *Geochimica et Cosmochimica Acta*, *43*, 1021–1029.

Govindaraju, K. (1994). Compilation of working values and sample description for 383 geostandards: Geostandards newsletter, 18, Special Issue, 1–158

Green, E. C. R., White, R. W., Diener, J. F. A., Powell, R., Holland, T. J. B., & Palin, R. M. (2016). Activity–composition relations for the calculation of partial melting equilibria in metabasic rocks. *Journal of Metamorphic Geology*, *34*, 845–869.

Holland, T. (2009). AX: A program to calculate activities of mineral endmembers from chemical analyses (usually determined by electron microprobe). Available at: http://www.esc.cam.ac.uk/research/research-groups/holland/ax

Holland, T. J. B., & Powell, R. (1998). An internally-consistent thermodynamic dataset for phases of petrological interest. *Journal of Metamorphic Geology*, *16*, 309–344.

Holland, T. J. B., & Powell, R. (2011). An improved and extended internally consistent thermodynamic dataset for phases of petrological interest, involving a new equation of state for solids. *Journal of Metamorphic Geology*, *29*, 333–383.

Krogh Ravna, E. J., & Terry, M. P. (2004). Geothermobarometry of UHP and HP eclogites and schists—An evaluation of equilibria among garnet–clinopyroxene–kyanite–phengite–coesite/quartz. *Journal of Metamorphic Geology*, *22*, 579–592.

Leake, B., Woolley, A., Arps, C., Birch, W., Gilbert, M., Grice, J., & Youzhi, G. (1997). Nomenclature of amphiboles; report of the subcommittee on amphiboles of the international mineralogical association commission on new minerals and mineral names. *Mineralogical Magazine*, *61*(405), 295–310.

Powell, R., & Holland, T. J. B. (1988). An internally consistent thermodynamic dataset with uncertainties and correlations: 3. Application to geobarometry, worked examples and a computer program. *Journal of Metamorphic Geology*, *6*, 173–204.

Rebay, G., Powell, R., & Diener, J. (2010). Calculated phase equilibria for a MORB composition in a P T window, 450–650 °C and 18–28 kbar: The stability of eclogite. *Journal of Metamorphic Geology*, *28*, 635–645.

White, R. W., Powell, R., Holland, T. J. B., Johnson, T., & Green, E. C. R. (2014). New mineral activity-composition relations for thermodynamic calculations in metapelitic systems. *Journal of Metamorphic Geology*, *32*, 261e286.

White, R. W., Powell, R., & Johnson, T. (2014). The effect of Mn on mineral stability in metapelites revisited: New a-x relations for manganese-bearing minerals. *Journal of Metamorphic Geology*, *32*, 809–828.